KU LEUVEN

FACULTY OF SCIENCE

# Resonantly damped oscillations of systems of two coronal loops

**Stief GIJSEN**

Supervisor: Prof. Dr. T. Van Doorsselaere

Thesis presented in fulfillment of the requirements for the degree of Master of Science in Mathematics

Academic year 2012-2013

© Copyright by KU Leuven

Without written permission of the promotors and the authors it is forbidden to reproduce or adapt in any form or by any means any part of this publication. Requests for obtaining the right to reproduce or utilize parts of this publication should be addressed to KU Leuven, Faculteit Wetenschappen, Geel Huis, Kasteelpark Arenberg 11 bus 2100, 3001 Leuven (Heverlee), Telephone +32 16 32 14 01.

A written permission of the promotor is also required to use the methods, products, schematics and programs described in this work for industrial or commercial use, and for submitting this publication in scientific contests.

# Preface

This thesis contains the investigations I performed when trying to get to grips with the intricacies of coronal loop oscillations. The study of oscillations of magnetic cylinders is a subject of interest for about 40 years, in which the simple models of homogeneous cylinders have been extended in many directions, stimulated by observations of the solar corona. This thesis hopes to lead the way to unify several extensions of these models, leading to a better understanding of the oscillations of these coronal loops. I have enjoyed working on this master thesis project; the process gave me the joy one gets by finding things out, thinking about a solving strategy or just calculating one's way towards an equation. In the end, I hope to have contributed if only an infinitesimal step ($\epsilon$, presumably) towards a further understanding of coronal loop oscillations. I hope you will enjoy reading it.

Several people should be thanked for making this thesis possible. First of all I would like to thank my promotor, Prof. T. Van Doorsselaere, for many insightful comments which helped to improve the quality of the thesis, for bringing his physical intuition to the rescue in order to bring sense into a chaos of calculations I sometimes produced, and finally for his ongoing support during the past year. Let us hope this will be the start of a long and fruitful collaboration. Also the readers, Prof. Em. M. Goossens and Prof. A. Kuijlaars should be thanked, not just for actually reading this thesis, but also for their critical questions and observations which improved this work as well as my presentation skills. Marcel deserves a mention in particular for having introduced me in the world of plasma dynamics. Finally, I want to thank my parents and sister for believing in me.

# Contents

# Chapter 1

# Introduction: observational evidence of coronal loop oscillations

The solar corona is the outer layer of the solar atmosphere. It consists of hot, ionized gas, called plasma, which interacts strongly with the magnetic field of the Sun. Typical values of the plasma parameters are $\rho = 10^{-11}$ kg/$m^3$, $B = 0.003T(30G)$ and $T = 10^6$ K. Because of its low plasma beta $\beta = 2p\mu/B^2$ (with $p$ the pressure, $B^2$ the square of the magnetic field strength and $\mu = 4\pi\dot{1}0^{-7}$ H m$^{-1}$ the permeability of vacuum) we can, in first approximation, neglect the gravitational force and pressure gradient force when we look at the large spatial structure of the corona. The dominant force is the Lorentz force. Early observations have already shown that the magnetic field causes the plasma to organize itself into loop-like structures which are expected to follow the magnetic field lines.

Broadly speaking, three models can be used to shed light on the different aspects of plasma behavior: a microscopic theory, dealing with the motions of charged particles interacting with a magnetic field and with each other through collisions, a kinetic theory of an electron and ion fluid with different characteristics and a global 'fluid' theory, called magnetohydrodynamics (MHD), which is obtained by averaging over the electron and ion distributions describing the plasma in terms of global characteristics such as pressure, temperature, etc. Each model can be constructed from the previous one by making a number of simplifications. The microphysics we lose will be compensated by the strength of the mathematical apparatus we can use within MHD. It has proven to be a successful model in explaining many global phenomena occurring in the Sun and also in this thesis I will stick to the MHD formalism. However, it is worth emphasizing that MHD has its limits, especially in describing small-scale phenomena, where the different dynamics of ions and electrons become important.

The evolution of the large-scale physical variables are governed in MHD by a set of partial differential equations:

$$\begin{aligned}
\frac{\partial \rho}{\partial t} &= -\nabla \cdot (\rho \mathbf{v}) \\
\rho \frac{d\mathbf{v}}{dt} &= -\nabla p + \rho \mathbf{g} + \frac{1}{\mu}(\nabla \times \mathbf{B}) \times \mathbf{B} \\
\frac{dp}{dt} &= -\gamma p \nabla \cdot \mathbf{v} + \underbrace{(\gamma - 1)\eta \frac{1}{\mu^2} |\nabla \times \mathbf{B}|^2} \\
\frac{\partial \mathbf{B}}{\partial t} &= \nabla \times (\mathbf{v} \times \mathbf{B}) + \underbrace{\eta \nabla^2 \mathbf{B}} \\
\nabla \cdot \mathbf{B} &= 0.
\end{aligned}$$

This set of equations is known as the set of ideal and resistive MHD equations. The underbraced terms denote the terms which are typical of resistive magnetohydrodynamics. Obtaining a full solution to the MHD equations is an extremely difficult task for almost any nontrivial geometry and set of boundary conditions; this is true analytically as well as numerically. Therefore, one often investigates the effect on small perturbations on an equilibrium state. This linearisation of the MHD equations yield expressions which can be (more easily) solved for certain equilibria and admit solutions in the form of waves and instabilities.

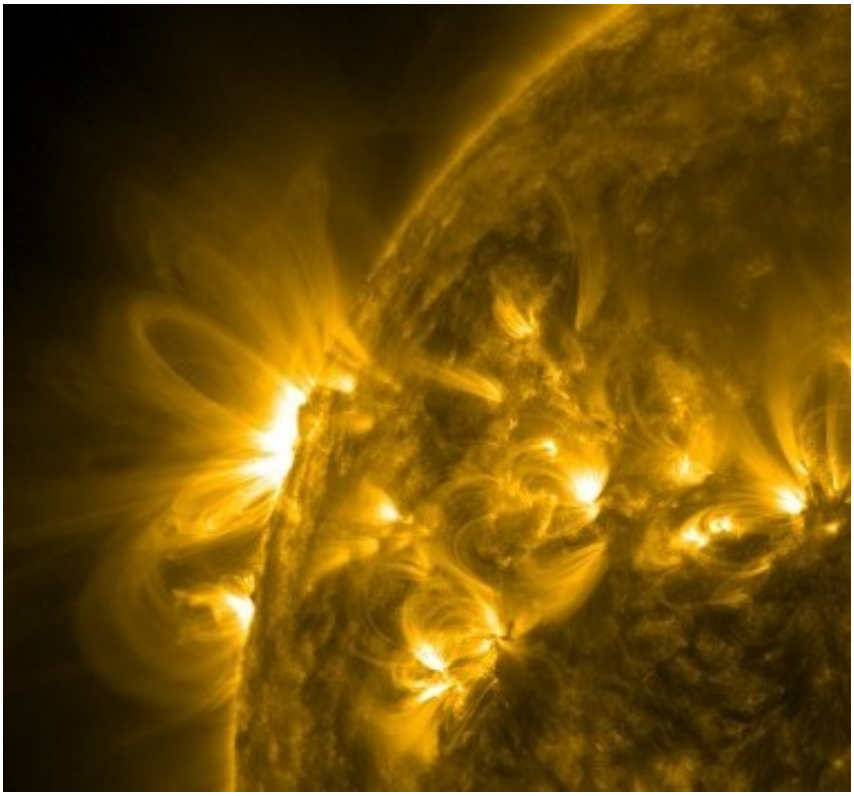

Figure 1.1: View from the corona in a spectral line of iron ($171A°$) at about 1 MK as observed by the Solar Dynamics Observatory (SDO) (From http://sdo.gsfc.nasa.gov/data/. Courtesy of NASA/SDO and the AIA, EVE, and HMI science teams.)

Cylindrical models for magnetic flux tubes were first developed in the late seventies (see f.e. Edwin & Roberts (1983) [10]). At the time this was a rather theoretical endeavor, since detailed observations of the solar atmosphere were not yet available. Since the launch of the Transition Region And Coronal Explorer (TRACE) in 1998 and we can observe the structure of the coronal loops in much more detail (Nakariakov et al. (1999) [26], Aschwanden et al. (1999) [3]). Figure (1.1) shows a snapshot of the corona in an active region. As one can see, in such regions the coronal plasma organizes itself into a structure with many thin loops. These observations have led to a resurgence of theoretical interest in these loops. In particular, one tries to improve the simple models of straight cylinders to more realistic, but still mathematically tractable ones.

Because the corona is optically thin, it is in general difficult to measure the local plasma parameters (such as density, pressure or magnetic field) directly. That is why one tries to resort to alternative measurement techniques. In 2007, observations of the Coronal Multichannel Parameter (CoMP) revealed that many waves are present throughout the solar corona (Tomczyk et al. (2007) [37]). The higher spatial resolution of the Atmospheric Imaging Assembly (AIA) on board the Solar Dynamics Observatory (SDO), launched in 2010, pointed to even more wave activity in the corona. Measuring the properties of these waves and comparing them with theoretical models of MHD waves in the corona, could give information about the environment these waves travel through. This technique is called 'coronal seismology', just like seismologists use the waves generated by earthquakes to probe the interior of the Earth.

A second motivation for constructing and fine-tuning analytical models of coronal loops comes from the observed temperature profile in the solar atmosphere.

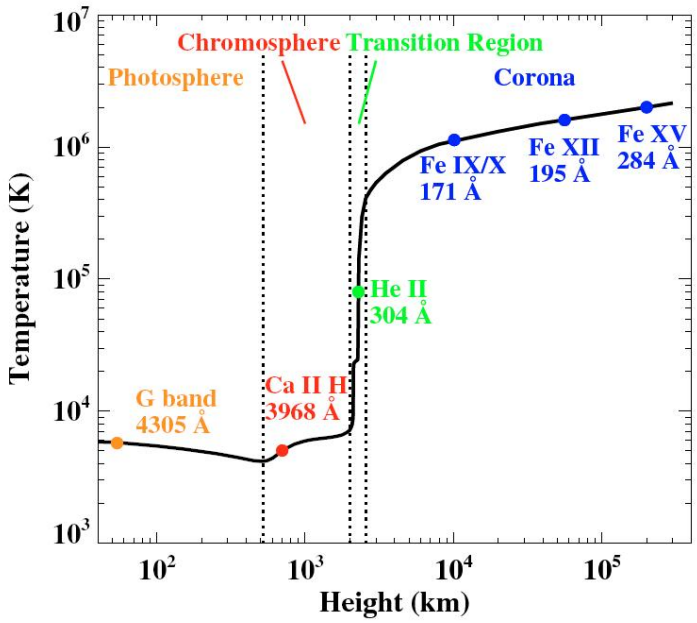


Figure 1.2: Temperature structure from the photosphere to the lower corona. Peak formation temperature of several spectral lines is also indicated with colored dots. From Yang et al., 2009 [42]

Figure (1.2) shows how the temperature in the solar atmosphere evolves with height. At the photosphere, the temperature drops from about 6500K in the lower photosphere to 4300K in the temperature minimum region. However, further outwards, in the chromosphere and transition region, the temperature starts to rise again until reaching a magnitude of about $2-3$ MK in the higher corona. The heating processes involved in generating and sustaining the hot corona have so far defied quantitative understanding. The questions of how and where the necessary energy flux (estimated approximately $200\frac{\mathrm{W}}{\mathrm{m}^2}$) is created, how it is transported and how the energy can dissipate in the corona are collectively known as the coronal heating problem.

Two models hold the most promise in explaining coronal heating. The first is the dissipation of current sheets when a reconnection process takes place in the corona. We will not further deal with this possibility. The second is the conversion of MHD wave energy into heat through resistive and viscous effects. This wave damping occurs mathematically due to coupling of the MHD equations which leads to the physical processes of resonant absorption (Chen & Hasegawa (1974) [8], Hollweg & Yang (1988) [18], Sakurai et al. (1991) [34] and others) and phase mixing (Heyvaerts & Priest (1983) [17]). We will have many occasions to investigate the mathematical framework for resonant absorption in the thesis. Finally, many other mechanisms probably contribute to coronal heating, some of which are better understood than others.

Using the data of the AIA instrument on SDO, McIntosh et al. (2011) [24] claimed that enough energy of transverse waves can be transformed into heat to bring the corona to its high temperature. However, these authors used models of Alfvén waves in homogeneous plasma's, hence overestimating the real energy flux by a factor of 10-50, depending on the equilibrium configuration (Goossens et al., 2013 [16]). In this thesis we will encounter the effects of geometry and density jumps or stratification on the nature of the waves these plasma's admit many times. To conclude, the coronal heating problem remains an open question even today.

Observations have also shown that often not just one loop, but a system of loops oscillates after being triggered by for example a solar flare. (A solar flare is an explosive phenomenon at the solar surface, visible as a sudden brightening at the surface and generally believed to result from the release of huge amounts (about $10^{25}$ J) of magnetic energy.) In view of these observations, generalising the results of cylindrical geometry to systems of two or more coronal loops is a natural approach in trying to improve the existing models of the corona. Building better models of the coronal loop structures improves the measurement of physical parameters by coronal seismology.

Generalisations of the simple models for a single homogeneous cylinder have developed in the two directions outlined above. On the one hand, the theory of resonant absorption can explain the rapid damping of the transverse oscillations. On the other hand, solutions to the eigenvalue problem and initial value problem for a system of coronal loops show how the collective dynamics of the ensemble differ from that of a collection of isolated magnetic flux tubes. I will review these results in Chapters 2 and 3 respectively. Only in the last five years, studies have been performed which aim to incorporate resonant absorption into a model of multi-loop oscillations. Most of these studies make use of computer simulations which solve the resistive MHD equations numerically.

In this master thesis, I will use and extend considerably the known mathematical methods and obtain explicit expressions for the damped oscillations of systems of coronal loops. The major part of the thesis will focus on a system of two parallel loops, in which the results can be analysed and interpreted in a clear way. In Chapter 4, I will use the well-known method of separation of variables to find new expressions to describe the resonantly damped oscillations of a system of two, not necessarily identical, coronal loops. However, an alternative approach is possible, based on a decomposition of the relevant variables into a series of cylindrical functions. This approach is inspired by the results of acoustic physics and studies of the interaction of acoustic waves with sunspots. I will derive and analyse some new equations to describe the oscillations of a system of more than two coronal loops in Chapter 5.

# Chapter 2

# Resonant damping of MHD waves in magnetic flux tubes

In this chapter we will look at the mechanism of resonant damping of incoming waves in magnetic flux tubes with an inhomogeneous layer. Already in the forties it was suggested that the dissipation of waves created at the solar interior could play a role in heating the upper corona (Biermann (1946), Schwarzschild (1948) [35]). Resonant damping is also of interest for laboratory fusion, since one needs to heat the plasma to attain the extremely high temperatures needed for nuclear fusion. Chen & Hasegawa (1974) [8] were the first to develop a model of plasma heating through resonant absorption in the context of laboratory plasmas. In the context of astrophysical plasmas, Hollweg & Yang (1988) [18] were the first to derive equations for resonant absorption in a Cartesian geometry. The extension to cylindrical flux tubes was first made by Sakurai et al. (1991) [34].

An homogeneous medium supports three kinds of waves. Alfvén waves are incompressible waves, driven by magnetic tension which propagate at the Alfvén speed $v_{\rm A} = \frac{B}{\sqrt{\mu\rho}}$. The energy of Alfvén waves propagates in the direction of the magnetic field. Slow and fast magnetosonic waves (often just called 'fast' and 'slow' waves) are compressible waves driven by pressure and magnetic tension forces. Fast waves are fairly isotropic, while slow waves are rather anisotropic with the energy flow confined to a small cone around the magnetic field lines.

The introduction of an inhomogeneous layer produces a continuous Alfvén and slow spectrum. Hence incoming waves with a frequency in this spectrum transfer part of their energy to local Alfvén or slow magnetosonic waves in the magnetic surface, and are damped as a result. The aim of this chapter is to put these arguments on a solid mathematical basis. For this I will mainly follow the papers of Sakurai et al. (1991) [34] and Goossens et al. (1995) [13].

Assume a magnetic flux tube (a magnetised cylinder) of length $L$, radius $R$ and embedded in an exterior plasma. We choose our coordinate system such that the $z$-axis is the axis of symmetry of the cylinder and the $xy$-plane divides the tube in two equal parts. The density $\rho = \rho(r)$ is a function of the radial coordinate only. This represents a one-dimensional model that still contains a lot of the physics present. The magnetic field

$\mathbf{B} = (0, 0, B_z)$ has only an axial component. We call such tubes straight (as opposed to twisted flux tubes which also have an azimuthal component $B_\varphi$). Furthermore, we assume that the plasma is pressureless. The equilibrium configuration is shown in Figure (2.1). I have chosen to present the analysis only for this simplified situation, even though the analysis can be readily generalized to twisted flux tubes including gas pressure (as was done in the aforementioned papers of Sakurai et al. (1991) [34] and Goossens et al. (1995) [13]), since in Chapters 3 and 4 analytical results have only been developed so far for this equilibrium configuration. However, also in this simplified model, a lot of interesting physics is present. In particular the principles of resonant absorption can be shown clearly in this configuration.

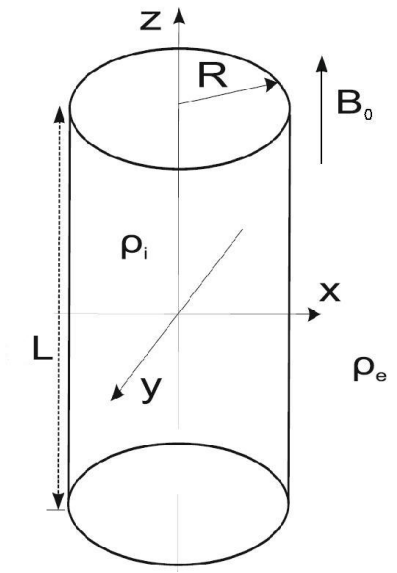


Figure 2.1: Sketch of the equilibrium configuration used in Section 2.1. Adapted from Morton & Erdélyi, 2009 [25].

This configuration trivially satisfies the equation of static equilibrium, since the pressure gradient force, magnetic pressure force and magnetic tension force all vanish. We now impose linear motions on this equilibrium state. The displacement vector will be denoted by $\xi$, hence $\mathbf{v} = \frac{d\xi}{dt}$. Since the background state only depends on $r$, we Fourier-analyze the perturbed quantities with respect to $\varphi$ and $z$ and assume a dependence of the form $\exp(i[m\varphi + kz - \omega t])$. A boundary condition to this problem is that the plasma is frozen into the dense photospheric plasma at heights $z = \pm L/2$. Mathematically, this means

$$\xi_\perp = 0 \qquad \text{at} \qquad z = \pm\frac{L}{2}.$$

Since in a pressureless plasma we automatically have $\xi_z = 0$ (Equation (2.3) ), this boundary condition conveys that the plasma is immobile at the foot points of the coronal loop, the so-called line-tying boundary condition. It quantizes the azimuthal and axial wave numbers $m$ and $k = \frac{n\pi}{L}$ respectively ($m, n \in \mathbb{N}$). In this subsection we stick to the ideal MHD formalism. Then the linearized equations have been derived in many places

and can be considered a part of the MHD heritage. They read

$$\textbf{radial EQM}: D\frac{d}{dr}(r\xi_r) = -C_2 r P' \tag{2.1}$$

$$\textbf{azimuthal EQM}: \rho(\omega^2 - \omega_{\rm A}^2)\xi_\varphi = \frac{im}{r}P' \tag{2.2}$$

$$\textbf{axial EQM}: \xi_z = 0 \tag{2.3}$$

$$\textbf{Pressure}: \frac{dP'}{dr} = \rho(\omega^2 - \omega_{\rm A}^2)\xi_r \tag{2.4}$$

$$\textbf{Compression}: \nabla\cdot\xi = \frac{-P'}{\rho v_{\rm A}^2}. \tag{2.5}$$

The coefficient functions are given by

$$\begin{aligned} D &= \rho v_{\rm A}^2 \omega^2(\omega^2 - \omega_{\rm A}^2) \\ C_2 &= \omega^2(\omega^2 - \omega_{\rm A}^2) - \frac{m^2}{r^2}v_{\rm A}^2. \end{aligned} \tag{2.6}$$

In these equations $\omega_{\rm A} = kv_{\rm A}$ is the Alfvén frequency. We can eliminate $\xi_r$ from equation (2.4) and substitute it into (2.1) to obtain a single equation for $P'$:

$$D\frac{d}{dr}\left(\frac{r}{\rho(\omega^2 - \omega_{\rm A}^2)}\frac{dP'}{dr}\right) - C_2 r P' = 0. \tag{2.7}$$

Substitute the coefficient functions (2.6) into this expression and divide through $v_{\rm A}^2$ to obtain

$$\rho(\omega^2 - \omega_{\rm A}^2)\frac{d}{dr}\left(\frac{r}{\rho(\omega^2 - \omega_{\rm A}^2)}\frac{dP'}{dr}\right) - \left(\frac{m^2}{r^2} - \frac{\omega^2 - \omega_{\rm A}^2}{v_{\rm A}^2}\right) r P' = 0. \tag{2.8}$$

Alternatively, eliminate $P'$ from (2.1) and substitute this into (2.4) to obtain a single equation for $\xi_r$:

$$\frac{d}{dr}\left(\frac{-D}{C_2 r}\frac{d(r\xi_r)}{dr}\right) - \rho(\omega^2 - \omega_{\rm A}^2)\xi_r = 0. \tag{2.9}$$

## 2.1 Solution to the eigenvalue problem in the dissipationless case

Before proceeding to derive the equation of damped oscillations, let us first look at a solution of the eigenvalue problem in the dissipationless case. We consider a flux tube of constant density $\rho_i$ embedded in an exterior plasma of density $\rho_e$. The density of the plasma changes discontinuously at the interface at $r = R$. In this case, it is possible to rewrite (2.8) as

$$\frac{d^2P'}{dr^2} + \frac{1}{r}\frac{dP'}{dr} - \left(\frac{m^2}{r^2} - \frac{\omega^2 - \omega_{\rm A}^2}{v_{\rm A}^2}\right) P' = 0. \tag{2.10}$$

Equation (2.10) represents a set of two differential equations, one for the interior of the flux tube (where we can set $\omega_{\rm A}^2 = \omega_{\rm Ai}^2 = \frac{B_0^2 k^2}{\mu\rho_i}$) and one for the exterior region (where we

take $\omega_{\rm A}^2 = \omega_{\rm Ae}^2 = \frac{B_0^2 k^2}{\mu \rho_e}$). Equation (2.10) is a classical Bessel equation. It has solutions in the form of Bessel functions. Since we are interested in waves which are propagating in the loop interior, but which are evanescent in the outside medium, we select the frequency $\omega^2$ such that $\omega_{\rm Ai}^2 \leq \omega^2 \leq \omega_{\rm Ae}^2$. This means that in the interior, due to the condition $\omega_{\rm Ai}^2 \leq \omega^2$, solutions of equation (2.10) should be linear combinations of the Bessel functions of the first and second kind, $J_m(x)$ and $Y_m(x)$. Since any physically relevant solution must remain finite at the origin, only the Bessel functions of the first kind should be retained. At the exterior region, equation (2.10) together with $\omega^2 \leq \omega_{\rm Ae}^2$ suggest the solutions should be expressed as linear combinations of the modified Bessel functions of the first and second kind, $I_m(x)$ and $K_m(x)$. We select the solutions which remain finite at infinity, hence the terms with $I_m$ must be rejected. This leads after a bit of calculation to the solutions

$$\begin{aligned} P_i' &= C_1 J_m(k_i r), \\ \xi_{r,i} &= \frac{C_1 k_i}{\rho_i(\omega^2 - \omega_{\rm Ai}^2)} J_m'(k_i r), \\ P_e' &= C_2 K_m(k_e r), \\ \xi_{r,e} &= \frac{C_2 k_e}{\rho_e(\omega^2 - \omega_{\rm Ae}^2)} K_m'(k_e r), \end{aligned} \tag{2.11}$$

in which $C_1$ and $C_2$ are constants and $k_i^2 = (\omega^2 - \omega_{\rm Ai}^2)/v_{\rm Ai}^2$, $k_e^2 = -(\omega^2 - \omega_{\rm Ae}^2)/v_{\rm Ae}^2$. The boundary conditions are that the perturbation of total pressure and the radial displacement vector are continuous at the interface. This leads to a dispersion relation for $\omega^2$ as shown in Goossens et al. (2009) [15]. This dispersion relation can be solved numerically as was done by Edwin & Roberts (1983) [10]. The results are shown in Figure (2.2). In this Figure we plotted the phase speeds of the eigenmodes which equation (2.10) supplemented with the boundary conditions allows, as a function of radial position (scaled by $k$).

When we assume that the loops are thin compared to their radius ($kR \ll 1$), it is possible to derive an analytical expression for the eigenfrequency by developing the Bessel functions appearing in (2.11) in a McLaurin series up to first order. As one can infer from Figure (2.2), only the fundamental mode for $m \geq 1$ (only shown here for $m = 1$ and $m = 2$) is defined in the entire tube. In this limit, the frequency of all modes with $m \geq 1$ all converge to the same radius given by the kink frequency

$$\omega_k^2 = \frac{\rho_i \omega_{\rm Ai}^2 + \rho_e \omega_{\rm Ae}^2}{\rho_i + \rho_e}. \tag{2.12}$$

It follows from the selection of solutions that $\omega_{\rm Ai}^2 < \omega_k^2 < \omega_{\rm Ae}^2$, which means that the kink frequency lies in the interval determined by the Alfvén frequencies of the two plasmas. Notice that the frequency is independent of $m$ when $m \geq 1$, as can also be seen in Figure (2.2). The fundamental kink and flute mode indeed converge to the same frequency if $kR \to 0$, while the behavior of the sausage mode ($m = 0$) is different.

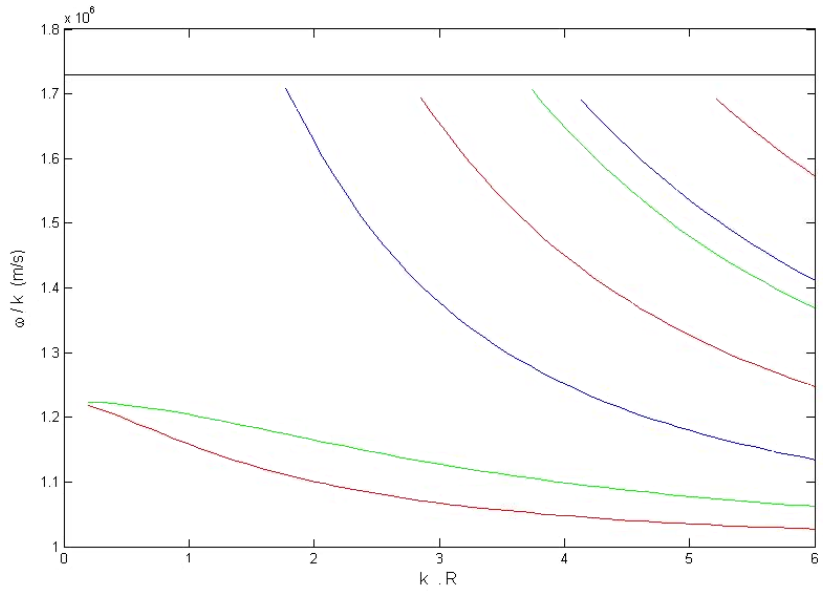


Figure 2.2: The different modes appearing as a solution of the dispersion relation found by Edwin & Roberts (1983). Blue lines correspond to the sausage modes (m=0), Red lines to the kink modes (m=1) and green lines to the flute modes (m=2). The black line corresponds to the Alfvén speed of the exterior plasma. Of the infinite number of modes, only a few are shown here.

## 2.2 Ideal MHD description — Resonant 'absorption'

Now that we know how the solution looks like in the dissipationless case, let us replace the interface at which the density is discontinuous by an inhomogeneous layer at radial position $[R-\frac{l}{2}, R+\frac{l}{2}]$ in which the density is a smooth, strictly monotonically decreasing function from $\rho_i$ to $\rho_e$. Since now the Alfvén frequency is a continuous function of $r$ in this inhomogeneous layer, new physics is introduced. We will first look at what happens when an external driver excites waves with a frequency in the Alfvén spectrum (the driven problem). Such a situation occurs often in coronal loops since waves are easily generated through movements of the photospheric footpoints of the loop. Then we will return to the eigenvalue problem just considered. This method is justified in this case since $\omega_{\rm Ai}^2 < \omega_k^2 < \omega_{\rm Ae}^2$.

In a driven problem, $\omega^2$ is prescribed and we are interested in the reaction of the system in the stationary state. Equations (2.1) and (2.4) are differential equations which become singular at the zeroes of $D$, i.e. when $\omega^2 = \omega_{\rm A}^2(r)$. At this position, there will be a resonance as the impinging wave will interact with local Alfvén waves. It can be seen from equations (2.7) and (2.9) that ideal MHD predicts singularities at the point $r_{\rm A}$ where $\omega^2 = \omega_{\rm A}^2$.

To solve this problem, we will have to move to a resistive MHD description. Two different possibilities can be considered. The first one is to use a numerical code to integrate the resistive MHD equations as was done in Van Doorsselaere et al. (2004) [38] and further studies. The second method goes as follows. In the resistive setting, dissipation is only

important in a narrow layer around the resonant point $r = r_{\rm A}$. In this layer, we can use simplified versions of the resistive MHD equations, which are also valid in an overlap region where the linear Taylor expansion of the local Alfvén frequency is a good approximation of this frequency. In the overlap region, both ideal and simplified resistive MHD are valid and should lead to the same results. If we are only interested in the global form of the solutions of (2.1) — (2.5), then the complicated solutions across the thin dissipative layer only give a jump condition across this layer. In the remainder of this section, we will derive an expression for this jump condition. An overview of the different regions involved is shown in Figure 2.3. It is a priori not clear why the validity of the linear Taylor expansion should hold outside the dissipative layer (as shown in this Figure) or whether its region of validity could exceed the inhomogeneity layer. This will be considered further on in more detail.

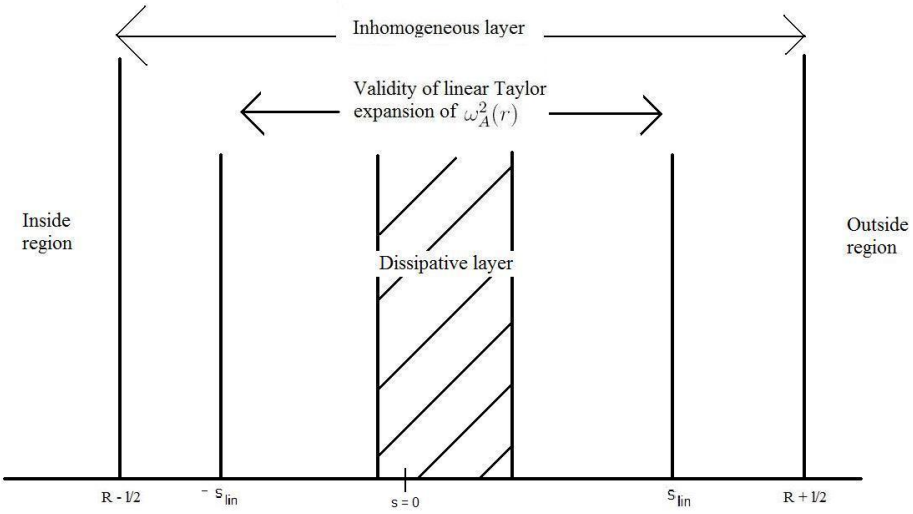


Figure 2.3: Radial cross-section of the magnetic flux tube with overview of the different regions involved in the driven problem.

Early studies (for example the one by Chen and Hasegawa (1974) [8] for laboratory applications) used a mathematical trick to resolve the singularities which are inherent of the ideal MHD equations. They added an imaginary component to the frequency such that $\omega = \omega_0 + i\gamma$ and $\omega^2 \approx \omega_0^2 + 2i\gamma\omega_0$ in first approximation ($\gamma \ll \omega_0$). This way they created an artificial damping term. Because there cannot be any dissipation in ideal MHD, they called this damping mechanism 'resonant absorption' instead of resonant dissipation which occurs in resistive MHD. As we will see later, the damping rate turns out not to depend on the actual coefficient of resistivity (or viscosity) as long as it is small. Hence even ideal MHD can describe most of the physics present.

Introduce a new radial variable $s = r - r_{\rm A}$. Then we can perform a linear Taylor expansion of the Alfvén frequency near the resonant point: $(\omega^2 - \omega_{\rm A}^2) \approx \Delta s$, where $\Delta = -\frac{d}{dr}\omega_{\rm A}^2(r)$. Using this expression for the Alfvén frequency, the coefficient functions $D$ and $C_2$ can also be expanded about $s = 0$. Keeping only the first non-zero contributions leads to

$$D_1 = \rho_{\rm A} v_{\rm A}^2 \omega_{\rm A}^2 \Delta s \qquad\qquad C_{20} = \frac{-\omega_{\rm A}^2 v_{\rm A}^2 m^2}{r_{\rm A}^2}. \tag{2.13}$$

The interval $[-s_{\text{lin}}, s_{\text{lin}}]$ in which this expansion is accurate is determined by the condition $s_{\text{lin}} \ll |2(\omega_A^2)'|/|(\omega_A^2)''|$. Since we are interested in the jumps $[f] = \lim_{s\to 0+}[f(s) - f(-s)]$, it suffices to take the constant terms in the Taylor expansion of the coefficient functions.

Let us substitute the Taylor expansions for $\omega_{\text{A}}^2, D$ and $C_2$ into equations (2.7) and (2.9). Then after a bit of algebra, equation (2.9) is transformed into the following differential equation:

$$\frac{d}{ds}\left(s\frac{d\xi_r}{ds}\right) - \left(\frac{m}{r_{\text{A}}}\right)^2 s\xi_r = 0. \tag{2.14}$$

Similarly, equation (2.7) can be transformed into

$$s\frac{d}{ds}\left(\frac{1}{s}\frac{dP'}{ds}\right) + \left(\frac{m}{r_{\text{A}}}\right)^2 P' = 0. \tag{2.15}$$

Rewriting (2.14) and (2.15) a bit further and substituting also $\alpha = \left(\frac{m}{r_{\text{A}}}\right)^2$ yields

$$s\frac{d^2\xi_r}{ds^2} + \frac{d\xi_r}{ds} - \alpha s\xi_r = 0, \tag{2.16}$$

$$s\frac{d^2P'}{ds^2} - \frac{dP'}{ds} + \alpha sP' = 0. \tag{2.17}$$

Equations (2.16) and (2.17) have regular singularities at $s = 0$. Therefore, we can look for solutions to these differential equations in the complex plane in the form of Frobenius series. For a differential equation of the form $N(z)z'' + Q(z)z' + R(z) = 0$ having a regular singularity at the point $z = z_0$, a solution in the form of a Frobenius series takes the form

$$f(z) = (z - z_0)^r \sum_{n=0}^{\infty} a_n (z - z_0)^n$$

for which $r \in \mathbb{R}$ is a solution of the indical equation

$$r(r-1) + p_0 r + q_0 = 0$$

where

$$p_0 = \lim_{z\to z_0}(z - z_0)\frac{Q(z)}{N(z)}, \qquad q_0 = \lim_{z\to z_0}(z - z_0)^2\frac{R(z)}{N(z)}.$$

Regularity of the singular points exactly means that these limits exist. Fuchs's Theorem tells us that we can find two linearly independent solutions if and only if $r_1 - r_2 \notin \mathbb{Z}$. If the difference is an integer, then a second solution can be found by adding a logarithmic term.

The indical equation of (2.16) is $r(r-1)+r = 0$, with double root $r = 0$. Fuchs's Theorem then implies that every solution is a linear combination of the form

$$\lambda_1\xi_{r1}(s) + \lambda_2[\xi_{r1}(s)\ln(s) + \xi_{r2}(s)], \tag{2.18}$$

where $\xi_{r1}(s)$ and $\xi_{r2}(s)$ are two Frobenius series (in this case they correspond to actual power series) starting with a constant. The indical equation for (2.17) is $r(r-1) - r = 0$

with the two roots $r = 0$ and $r = 2$. Then according to Fuchs's Theorem the solutions to (2.17) look as follows:

$$\mu_1 P_1'(s) + \mu_2 [P_1'(s) \ln(s) + P_2'(s)]. \tag{2.19}$$

Here $P_1'(s)$ is a Frobenius series, which corresponds to a power series starting with a term in $s^2$. The solution $P_2'(s)$ starts with a constant term. It can be shown that the solutions $\xi_{r1}$ and $P_1'$ containing the logarithmic terms are continuous, whereas the solutions $\xi_{r2}$ and $P_2'$ may jump (Goedbloed 1983 [11]). This observation allows us to rewrite the solution for the radial displacement as follows:

$$\xi_r(s) = R\xi_{r1}(s) \ln|s| + \begin{cases} \xi^-(s) & s < 0 \\ \xi^+(s) & s > 0 \end{cases} \tag{2.20}$$

In this equation $R$ is a constant. Consider equation (2.20) in the complex plane. Moving from the positive to the negative real axis implies a jump of the complex argument of $\pi$ and hence of the complex logarithm of $i\pi$. This jump in the radial displacement as we move across the Alfvén resonant point is inherent of the differential equations we obtain, but cannot be put on a solid physical basis using only the ideal MHD description. The resistive equations have to be used. In the formula for the pressure perturbation (2.19) we can neglect the $s^2 \ln(s)$ contribution to the solution for $s \ll 1$. This implies that no logarithmic singularity is present for the pressure perturbation across the Alfvén resonant point.

Another way of obtaining these results, which also yields an expression for $R$ and $\xi_{r1}(s)$ in equation (2.20) is by substituting (2.13) into equations (2.1) and (2.4). Neglecting terms of order $s^2$ then yields the following equations:

$$\Delta s \frac{d\xi_r}{ds} = \frac{m^2}{\rho_{\mathrm{A}} r_{\mathrm{A}}^2} P', \tag{2.21}$$

$$s \frac{dP'}{ds} = 0. \tag{2.22}$$

Equation (2.22) can be solved using distributions. The factor $s$ appearing in (2.22) leads to a Heaviside function contribution, hence its solution can be written as

$$P' = c_1 + c_2 H(s). \tag{2.23}$$

It can be shown that continuity of the solutions containing the logarithmic terms implies that the Heaviside contribution to the solution vanishes. Hence we have derived a conservation law across the resonant point, namely

$$P' = \text{const.} \tag{2.24}$$

Using this conservation property, by a separation of variables one can solve equation (2.21) leading to

$$\xi_r(s) = \frac{m^2}{\rho_{\mathrm{A}} r_{\mathrm{A}}^2 \Delta} P' c_1 \ln|s| + \begin{cases} \xi^-(s) & s < 0 \\ \xi^+(s) & s > 0. \end{cases} \tag{2.25}$$

Now we are able to identify the constant $R$ and the function $\xi_{r1}(s)$ appearing in (2.20). The jump which appears in (2.25) is due to resistive effects. It has been substituted here

because the ideal MHD solution is not valid all the way up to $s = 0$, since for small values of $s$ we move into the dissipative layer. The jump which we are interested in is

$$[\xi_r(s)] = \lim_{s\to 0} [\xi_r(s) - \xi_r(-s)] = \xi^+(s) - \xi^-(s). \tag{2.26}$$

By using the ideal MHD description, we have implicitly assumed that we are away from the resonant point (at least outside the dissipative layer). The jump condition (2.26) has been obtained by an expansion about the resonant point of the solution in the outside layer. What we will do next, following the method of Goossens et al. (1995) [13] and Ruderman et al. (1995) [32], is calculating the solution in the dissipative layer, using a set of simplified resistive equations. Then an asymptotic expansion of this dissipative solution 'far away' from the resonant position, in a precise sense which will be explained later, should coincide with the ideal MHD solution (2.25).

Conservation law (2.24) expresses that the perturbation of gas pressure balances the magnetic pressure perturbation. In the more general case with $B_\varphi \neq 0$, a similar conservation law can be found, although in this case the pressure perturbation does not have to be continuous anymore. (See Goossens et al. (1995) [13]). In the general case, the outwards total pressure gradient and the inwards magnetic tension force at the resonant surface, caused by the original curvature of the field lines plus the additional curvature induced by the displacement of the field lines by the incoming wave, balance one another.

From this the following physical picture arises. An externally driven wave propagates through the magnetic flux tube, inducing plasma motions (in the radial and azimuthal direction, as seen by equations (2.2) and (2.25) ) which deform the magnetic field lines because of conservation of magnetic flux in ideal MHD. The magnetic tension force tries to counteract these motions, setting up oscillations along the magnetic field lines. However, only at the resonant magnetic surface, a stable oscillation can be maintained. Incoming waves can hence be converted very efficiently into Alfvén waves, thus causing a decrease in the radial component of the driving wave. The magnitude of the jump and its physical origin cannot be described anymore using ideal MHD. We have to move towards a resistive MHD description.

## 2.3 Resistive MHD description — Jump conditions

Let us now include the Ohmic resistivity term $\eta\nabla^2\mathbf{B}$ in the linearised induction equation. We will keep the adiabatic energy equation, as numerical studies have shown that the inclusion of resistivity in the energy equation does not significantly alter the results obtained for resonant damping (Poedts et al. 1990 [29]). Since we can neglect resistivity everywhere but in a small dissipative layer, this leads to the following mathematical simplifications:

- We can neglect the derivatives of $\eta$ with respect to the derivatives of $\xi$.
- In the dissipative layer there are only large gradients in the radial direction.

Then it can be shown (reducing the equations of Goossens et al. 1995 [13]) that equations (2.1) and (2.4) can be rewritten to

$$D_\eta \frac{d}{dr}\left(r\xi_r\right) = -C_2 r P' \tag{2.27}$$

$$\frac{dP'}{dr} = \rho(\omega_\eta^2 - \omega_{\rm A}^2)\xi_r. \tag{2.28}$$

Here $D_\eta = \rho v_{\rm A}^2 \omega^2(\omega_\eta^2 - \omega_{\rm A}^2)$ where $\omega_\eta^2$ stands for the differential operator

$$\omega_\eta^2 = \omega^2\left(1 - i\frac{\eta}{\omega}\frac{d}{dr^2}\right).$$

The notation $\omega_\eta^2$ is used to bring the equations (2.27) and (2.28) as much as possible in the same form as their ideal counterparts (2.1) and (2.4). The singularity which was present in the ideal MHD description is absent in the resistive MHD equations (2.27) and (2.28). The price we have to pay is that differential equation (2.27) is now of third order and (2.28) of second order, with the coefficient of the highest-order derivative proportional to $\eta$.

As before, we can linearise (2.27) and (2.28) about the resonant point $s = 0$. Then translating the coordinate system to $s = r - r_{\rm A}$ coordinates leads to

$$\left(s\Delta - i\omega\eta\frac{d^2}{ds^2}\right)\frac{d\xi_r}{ds} = \frac{m^2}{\rho r_{\rm A}^2} \tag{2.29}$$

$$\left(s\Delta - i\omega\eta\frac{d^2}{ds^2}\right)\frac{dP'}{ds} = 0. \tag{2.30}$$

All equilibrium quantities are understood to be evaluated in $s = 0$. Dissipation will become important as soon as the terms $s\Delta$ and $i\omega\eta\frac{d^2}{ds^2}$ on the left-hand side of (2.29) and (2.30) are comparable in magnitude. This results in a layer of thickness $\delta_{\rm A}$ of the dissipative layer determined by $|\delta_{\rm A}\Delta| \approx \left|\frac{i\omega\eta}{\delta_{\rm A}^2}\right|$ or

$$\delta_{\rm A} = \left(\frac{\omega\eta}{|\Delta|}\right)^{1/3}. \tag{2.31}$$

This equation also holds for planar geometry and remains valid if we include viscosity (then the factor $\eta$ would only be replaced by $\eta + \nu$, as one can see by comparing the papers of Sakurai et al. (1991) [34] and Goossens et al. (1995) [13]). By definition of the magnetic Reynolds number $R_m$ we have $\delta_A \sim R_m^{-1/3}$ and since $R_m \gg 1$ in the corona, it follows from these considerations that

$$\frac{s_{\rm lin}}{\delta_A} \gg 1. \tag{2.32}$$

This shows that Figure (2.3) is 'correct' in the sense that the linear Taylor expansion around the resonant point is also valid in an overlap region outside the dissipative layer. Introducing the new variable $\tau = s/\delta_A$, we can rewrite (2.29) and (2.30) to

$$\left(\frac{d^2}{d\tau^2} + i\,\mathrm{sgn}(\Delta)\tau\right)\frac{d\xi_r}{d\tau} = \frac{im^2 P'}{\rho r_{\rm A}^2|\Delta|}, \tag{2.33}$$

$$\left(\frac{d^2}{d\tau^2} + i\,\mathrm{sgn}(\Delta)\tau\right)\frac{dP'}{d\tau} = 0.$$

It can be shown that the conservation law (2.24) still holds across the resonant point in resistive MHD (see Goossens et al. 1995 [13]). Then one can use an integral representation for the solution of $\xi_r$ (originating in a solution for $\frac{d\xi_r}{d\tau}$) in the dissipative layer which reads

$$\xi_r = -\frac{m^2 P'}{\rho r_{\rm A}^2 |\Delta|} G(\tau) + C_\xi, \qquad P' = C_{P'}. \tag{2.34}$$

Here $C_\xi$ and $C_{P'}$ are (integration) constants and the function $G(\tau)$ is defined by

$$G(\tau) = \int_0^\infty \frac{e^{-u^3/3}}{u} \{\exp(iu\tau\,\mathrm{sgn}(\Delta)) - 1\}\, du \tag{2.35}$$

The asymptotics for $\tau \to \pm\infty$ for $G$ (which corresponds to $s \to s_{\rm lin}$, hence with the solution outside the dissipative layer) can then be calculated. This was done in Goossens et al. (1995) [13] and yields the following asymptotic expansion of $\xi_r$:

$$\xi_r \approx \frac{m^2 P'}{\rho_{\rm A} r_{\rm A} \Delta} \left( \ln|\tau| + \frac{2\nu}{3} + \frac{1}{3}\ln 3 - \frac{i\pi}{2}\mathrm{sgn}(\Delta\tau) \right) + C. \tag{2.36}$$

where $\nu$ is Euler's constant. As explained in the last section, we will now match the asymptotic expansion (2.36) of the dissipative solution with the ideal solution (2.25) near the resonant point. This is readily done and gives an expression for the jump (2.26). Since we already proved that $P'$ is constant across the dissipative layer, we obtain that

$$[\xi_r] = -\frac{i\pi m^2 P'}{\rho r_{\rm A}^2 |\Delta|}, \qquad [P'] = 0. \tag{2.37}$$

Note that by the matching condition, this jump could also have been calculated by taking the limit

$$\lim_{\tau\to\infty} [\xi_r(\tau) - \xi_r(-\tau)] \tag{2.38}$$

in equation (2.36). This means that

$$[\xi_r] = \lim_{s\to 0} [\xi_r(s) - \xi_r(-s)] = \lim_{\tau\to\infty} [\xi_r(\tau) - \xi_r(-\tau)] \tag{2.39}$$

if we accept a slight abuse of notation: the expression in the middle refers to the ideal MHD solution, and the expression on the right to the dissipative solution.

The magnitude of the jumps depends on the equilibrium quantities but also on the azimuthal wave number $m$. As one can see, the jump $[\xi_r]$ has a negative sign, which means that the incoming wave indeed leaves behind some of its energy creating Alfvén waves at the resonant surface.

From equation (2.12), we inferred that the kink eigenmode lies in the Alfvénspectrum and that they are susceptible to resonant damping. As one can see from figure (2.2), when the tube thickness increases more eigenmodes lie in the Alfvén spectrum. However, this does not mean that these waves will therefore be automatically damped. For this phenomenon to occur it is necessary that the differential equations (2.1) — (2.5) are coupled. For a straight magnetic field, it can be seen that when $m = 0$, these differential equations can be solved independently for the radial component and for the components in the perpendicular direction. In this case, no coupling (hence no resonance) can occur between Alfvén waves and the sausage modes (Goossens 2008) [14]. This is confirmed by the expression for the jump condition (2.37).

## 2.4 Damping decrement and discussion

In the previous section, we derived a jump condition across the dissipative layer in a driven problem. Now we return to the eigenvalue problem considered in section 2.1. The jump conditions (2.37) can be used as new boundary conditions to the dispersion relation derived from (2.10). However, since (2.10) was only valid in the inside and outside homogeneous regions, we should actually integrate the ideal MHD solution for a nonuniform equilibrium to the dissipative layer to extend the jump condition (2.37) to a jump condition for the inhomogeneous layer.

A way around this problem is to use the so-called thin-boundary (TB) assumption. Traditionally, this assumption is stated as $l/R \ll 1$. It is quite a strong physical assumption since the thickness of the dissipative layer is given by (2.31). Numerical simulations using fully resistive MHD (Van Doorsselaere et al. [38]) show that the thin boundary assumption is nevertheless accurate for $l/R \lesssim 0.4$ (Goossens (2008) [14]). Hence the TB assumption is accurate far beyond the region in which it should be accurate mathematically. However, for larger values of $l/R$ discrepancies are found between analytical and numerical results.

When we assume a thin boundary, the Frobenius expansion about the ideal singularity is valid throughout the entire inhomogeneous layer. This layer will then nearly be small enough to coincide with the dissipative layer, and the jump condition (2.37) can be used as a jump condition across the inhomogeneous layer itself. Note that this approach hinges on two approximations: near-equality of the inhomogeneous and dissipative layer as well as the fact that the validity region of the Frobenius expansion about the ideal singularity does not extend too far outside this layer. In reality, the convergence of the resistive solutions to the ideal quasi-modes is not guaranteed. (Quasi-modes are 'solutions' of the ideal MHD equations in nonuniform plasma's with a complex value for $\omega$ as in the formulation of resonant absorption by Chen & Hasegawa, 1974 [8], which cannot exist as eigenmodes of the ideal MHD equations proper because of the self-adjointness of the force operator in ideal MHD [12].) When the resistivity is lowered, the local resistive eigenfunctions become strongly oscillatory. The only way in which the local resistive solutions converge to the ideal quasi-solutions is due to the fact that the oscillatory domain scales as the thickness of the dissipative layer $\delta_A$, outside of which the resistive and ideal solutions converge pointwise to one another (Andries, 2003 [1]).

In what follows, I will be forced to impose the equality of the dissipative and inhomogeneous layer in order to derive an expression for the linear damping rate. This approach, which represents a simplification of the original TB assumption (but which is often called just the TB assumption as well), has often been made in studies of damped loop oscillations with good results (but see below).

Using the thin boundary assumption, it can be shown (see Goossens et al. (2009) [15]) that an expression for a small damping decrement $\gamma$ (this means that we put $\omega = \omega_k + i\gamma$ and approximate $\omega^2 \approx \omega_k^2 + 2i\gamma\omega_k$) can be given by

$$\frac{\gamma}{\omega_k} = -\frac{\pi}{2\omega_k^2 R}\frac{\rho_i^2\rho_e^2}{(\rho_i+\rho_e)^3}\frac{(\omega_{Ai}^2-\omega_{Ae}^2)^2}{\rho_A|\Delta_A|}. \tag{2.40}$$

In particular, some prescribed density profiles (linear or sinusoidal) were investigated in

the context of studying the eigenfunctions.

In equation (2.40) we could substitute $|\Delta_A| \sim \rho/l$ to infer that the damping decrement is proportional to $l/R \ll 1$. This means that the damping times are proportional to $R/l \gg 1$. TRACE and SDO observations show, however, that this is not the case in reality; the observed oscillations turn out to be efficiently damped in only a few wave periods. This does however not mean that the model we derived turns out to be useless in the real physical case, for two reasons. The fact that resonant damping can be described mathematically and interpreted physically in cylindrical plasmas is an achievement in itself. More importantly, we can use (2.40) to firmly conclude that the nonuniform layer in a coronal loop will be quite large. Thereafter, comparing the numerical results of Van Doorsselaere et al. (2004) [38] with observations can be used to estimate the density contrast $\rho_i/\rho_e$ of the observed loops in the corona. Hence theoretical models of damped loop oscillations can be used as tools to measure the equilibrium quantities in the corona; this is coronal seismology in action.

As we have seen, in our description of resonant damping the radial wave energy is only converted into energy of Alfvén waves propagating along the magnetic surfaces. Hence this phenomenon could a priori not account for the heating of the corona. However, since we linearized equations (2.28) and (2.27), which were third order with the highest-order derivatives proportional to $\eta$, we neglected a lot of nonlinear phenomena which create short length scales and damping. Furthermore, consider a coronal loop in an active region where an oscillation is triggered by a solar flare. The driving frequency will then be a superposition of a broad frequency spectrum. When this wave packet interacts with the coronal loop, each surface will resonate at its own Alfvén frequency. After a while, the different neighboring flux surfaces get out of phase with one another. This process is known as phase mixing and has first been described in Heyvaerts and Priest (1983) [17]. Phase mixing creates small length scales and a consequent decrease of the magnetic Reynolds number. In this situation, the Ohmic resistive term will dominate locally and wave energy will be converted into heat.

# Chapter 3

# Oscillations of two homogeneous parallel magnetic loops: separation of variables

In the previous chapter, we looked at the oscillations of one magnetic cylindrical flux tube. Now we want to extend the results to a system of coronal loops. The reason is that often, coronal loops in active regions do not appear in isolation but as a part of a system of loops which can be triggered simultaneously. It is also argued that loops as we see them actually consists of several strands, i.e. subloops with an enhanced density, which are not detected with the current resolution of the spacecraft. Observations (Verwichte et al. (2004) [40]), numerical simulations (Luna et al. (2008) [21]) and analytical investigations (Van Doorsselaere et al. (2008) [39]) all show that loops that are part of a system interact with one another and can oscillate in phase or anti-phase. Hence the dynamics of the system is more than just the sum of the dynamics of the individual loops. A natural starting point is to study the damped oscillations of a system of two parallel loops. This model will be a generalization of the single-loop model and hence constitutes a more realistic model, which could lead to better seismology. A more elaborate motivation for an analytical study of these systems will be given in Chapter 4, when we will look at the system of two coronal loops including damping.

The aim of my thesis is to study the damped oscillations of a system of two loops. To gain more insight in the results obtained there, we will first look at a system of two parallel magnetic flux tubes. This chapter will briefly summarize the results of the numerical study of Luna et al. (2008) [21] and the analytical study of Van Doorsselaere et al. (2008) [39], since we need to know the behavior of the homogeneous system before we can move on to more complex systems.

## 3.1 Equilibrium configuration

The equilibrium configuration consists of two straight parallel magnetic cylinders of length $L$ with radii $R_L$ and $R_R$ and densities $\rho_L$ and $\rho_R$ respectively. The plasma density in the

exterior region is $\rho_e$. The loop axes are parallel to the z-axis in a Cartesian geometry. A constant magnetic field $\mathbf{B} = B\mathbf{1_z}$ is applied along the loop axes. The $xy$-plane cuts both loops in two equal parts. A sketch of the equilibrium configuration is shown in Figure (3.1).

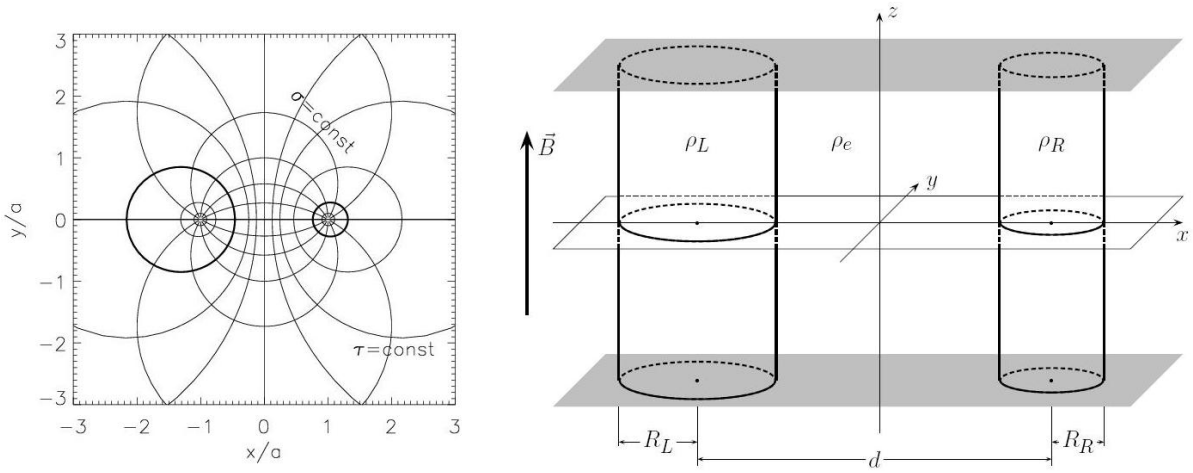


Figure 3.1: Left: Sketch of the bicylindrical $(\sigma, \tau)$ coordinate system. The lines $\sigma = \text{const}$ pass through the points $x = \pm a$, the lines $\tau = \text{const}$ are nested circles around these points, whose radius tends to zero and whose centre tends to $\pm a$ as $|\tau| \to \infty$. Right: Sketch of the equilibrium configuration (from Van Doorsselaere et al. (2008) [39] )

We study the problem in bicylindrical $(\sigma, \tau)$ coordinates. This coordinate system is most suited to study the problem, since the tube radii can be expressed in the simplest way. In this coordinate system, there exist two points $x = \pm a$ such that all coordinate surfaces $\sigma = \text{const}$ pass through these two points. The tube boundaries can be expressed by $\tau = -\tau_L$ and $\tau = \tau_R$. The relation between cartesian and bicylindrical coordinates is given by

$$x = \frac{a \sinh \tau}{\cosh \tau - \cos \sigma}, \qquad y = \frac{a \sin \sigma}{\cosh \tau - \cos \sigma}. \tag{3.1}$$

The tube radii and the distance between the two tube centers can be expressed (after some calculations) as

$$R_L = \frac{a}{\sinh \tau_L}, \qquad R_R = \frac{a}{\sinh \tau_R}, \qquad d = \frac{a}{\coth \tau_L + \coth \tau_R}. \tag{3.2}$$

From equation (3.1) and Figure (3.1) (left) we can investigate two geometrical limits which will be relevant later on. When $|\tau| \to \infty$, the circles $\tau = \text{const}$ which are nested around the points $x = \pm a$ will become smaller. Furthermore, their centers will converge to the points $x = \pm a$ themselves. When $|\tau| \ll 1$, the two circles become large (filling the entire left and right half-plane in the limit $\tau \to 0$). Furthermore, an annulus in the ring $\tau_0 < \tau < \tau_0 + \triangle\tau$ will become very asymmetric for small values of $\tau$.

We adopt for analytical simplicity the cold plasma approximation. Also in the numerical study by Luna et al. (2008) this approximation is made. This removes the energy equation from the analysis. The relevant ideal MHD equations are hence the equation of motion

and the induction equation:

$$\rho\frac{\partial^2\xi}{\partial t^2} = \frac{1}{\mu_0}\left(\nabla\times\mathbf{b}\right)\times\mathbf{B} \tag{3.3}$$

$$\mathbf{b} = \nabla\times(\xi\times\mathbf{B}). \tag{3.4}$$

These equations satisfy the regularity conditions $P'\to 0$ as $\tau^2+\sigma^2\to 0$ and the solutions remain bounded when $\tau\to\infty$. Here $P'$ is the total pressure perturbation, which in the cold approximation reduces to the magnetic pressure perturbation, as in chapter two. Just as at the beginning of chapter two, we are able to impose the boundary conditions that the $\tau$-component of the radial displacement and the total pressure perturbation are continuous at the interface. Note that we can interpret $\tau$ as the 'radial' coordinate here since we only assume an infinitesimal change in this quantity. In chapter four, we shall see that one must take into account that $\tau$ does not fully represent the radial direction since moving a distance $\triangle\tau$ from the boundary will lead to a smaller increase at the region in between the tubes than in the region on the other side (see Figure (4.2) in Chapter four). Using the notation for the jumps $[f]=\lim_{s\to 0+}\left(f(s)-f(-s)\right)$ of chapter two, the boundary conditions read

$$[P'] = 0 \qquad\qquad [\xi_\tau] = 0. \tag{3.5}$$

## 3.2 Eigenmodes and initial value problem

We look at two distinct methods to determine the eigenfunctions and compare them with each other. The set of ideal MHD equations can be solved numerically as was done by Luna et al. (2008) [21]. The authors focus on the kink solution $m=1$. They find four eigenfrequencies of the system corresponding to four different types of motions, as can be seen in Figure (3.2). This figure shows the velocity field of the four kink-like modes and the corresponding pressure perturbations. Just as in the case for one cylinder, these motions displace the tube axis and hence the tube as a whole. From Figure (3.2) it is clear that both tubes interact with each other. The four different eigenmodes can be classified as symmetric or antisymmetric and the displacement can either be in the $x$ or the $y$-direction. The smallest frequencies (longest wavelengths) are found for the $S_x$ and $A_y$-displacements found in Figures (3.2a) and (3.2d), with the $S_x$-displacement having the largest frequency of the two.

The movement of the plasma between the tubes can explain the difference in frequencies. As one can see in figures (3.2a) and (3.2d), the plasma in between the tubes follows the motion of the tubes and in a sense 'helps' to push the tubes in the $S_x$ respectively $A_y$-direction. For the $A_x$-mode, the intermediate plasma is compressed and rarefied as the tubes move towards one another, thus inhibiting their movement. Finally, for the $S_y$-mode the plasma surrounding one flux tube moves in the direction opposing the movement of the other tube.

We can also follow an analytical route. Using equations (3.3) and (3.4), we can rewrite the total pressure perturbation (after some algebra) as

$$P' = -\rho v_A^2\nabla\cdot\xi. \tag{3.6}$$

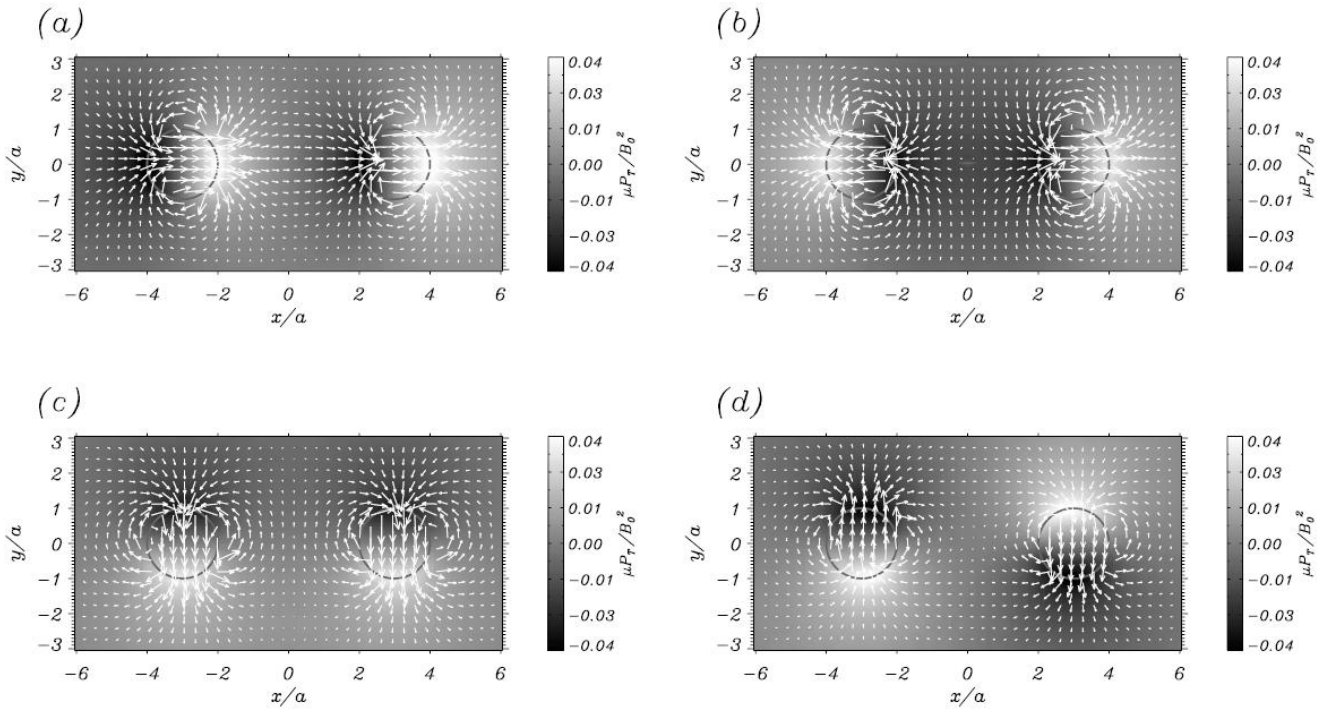


Figure 3.2: Velocity field and pressure perturbations (color index) of the four normal modes of a system of two identical loops. (a) Loops oscillating in phase in the $x$-direction ($S_x$-mode) (b) Loops oscillating in anti-phase in the $x$-direction ($A_x$-mode) (c) Loops oscillating in phase in the $y$-direction ($S_y$-mode) (d) Loops oscillating in anti-phase in the $y$-direction ($A_y$-mode) (from Luna et al. (2008) [21] )

After rewriting and substituting the nabla operator in bicylindrical coordinates, and assuming a dependence of all variables on $z$ and $t$ of the form $\cos(\pi z/L)\exp(i\omega t)$ one finds the following set of equations:

$$(\omega^2 - v_A^2 k^2)P' + v_A^2 \nabla_\perp^2 P' = 0 \tag{3.7}$$

$$(\omega^2 - v_A^2 k^2)\xi_\tau = \frac{\cosh\tau - \cos\sigma}{a\rho}\,\frac{\partial P'}{\partial \tau} \tag{3.8}$$

$$(\omega^2 - v_A^2 k^2)\xi_\sigma = \frac{\cosh\tau - \cos\sigma}{a\rho}\,\frac{\partial P'}{\partial \sigma}. \tag{3.9}$$

In equation (3.7) $P'$ represents only the $\sigma$- and $\tau$-dependence of the total pressure perturbation (a slight abuse of notation) and the operator $\nabla_\perp^2$ is the Laplacian in the direction perpendicular to the magnetic surfaces:

$$\nabla_\perp^2 = \frac{(\cosh\tau - \cos\sigma)^2}{a^2}\left(\frac{\partial^2}{\partial\tau^2} + \frac{\partial^2}{\partial\sigma^2}\right).$$

We will now try to manipulate the governing equations such that a full separation of variables can be performed. This is but one way of solving these equations, depending crucially on the representation in bicylindrical coordinates. There are, however, other ways to proceed which depend less on the coordinate system involved. Note from equation (3.7) that $P'$ satisfies the scalar Helmholtz equation. In Chapter 5, I will adapt results

from acoustic scattering theory to look for an alternative way to derive the solutions to equations (3.7) — (3.9).

Suppose that the loop length $L$ is much larger than the size of the system in the transverse direction $d$. Such an assumption is not unreasonable in view of the observed distances between coronal loops and their length (Aschwanden et al., 2003 [4]). Denote this ratio by $d/L =: \varepsilon \ll 1$. This approximation is known as the long-wavelength approximation (since $k = \frac{n\pi}{L}$). Depending on the separation between the tubes we have either $a \sim d$ or $a \ll d$, but that does not matter for the analysis. Because $\omega \sim k v_A$ we have $\omega a/v_A \sim ka \leq kd = \pi d/L = O(\varepsilon) \ll 1$. Then comparing the first term to the second one in equation (3.7) leads to

$$\left| \frac{\omega^2 - v_A^2 k^2}{v_A^2 (\cosh\tau - \cos\sigma)^2/a^2} \right| \sim \left| \left(\frac{\omega a}{v_A}\right)^2 - k^2 a^2 \right| = O(\varepsilon^2) \ll 1.$$

Hence the first term can be ignored in (3.7), which leads to the equation

$$\frac{\partial^2 P'}{\partial \tau^2} + \frac{\partial^2 P'}{\partial \sigma^2}. \tag{3.10}$$

We can try to solve (3.10) by a separation of variables

$$P' = \Theta(\tau)\cos(\sigma - \sigma_0) - \Theta(0)\cos\sigma_0, . \tag{3.11}$$

Then applying the regularity conditions to equations (3.8) and (3.10) leads to the following solutions:

$$\Theta(\tau) = \begin{cases} C_L\, e^{\tau} & \tau < -\tau_L, \\ C_1\, e^{\tau} + C_2\, e^{-\tau} & -\tau_L < \tau < \tau_R, \\ C_R\, e^{-\tau} & \tau > \tau_R, \end{cases} \tag{3.12}$$

$$\xi_\tau = \hat{\xi}_\tau(\tau)(\cosh\tau - \cos\sigma)\cos(\sigma - \sigma_0), \tag{3.13}$$

$$\hat{\xi}_\tau(\tau) = \begin{cases} \dfrac{C_L e^{\tau}}{a\rho_L(\omega^2 - v_{AL}^2 k^2)} & \tau < -\tau_L, \\ \dfrac{C_1 e^{\tau} - C_2 e^{-\tau}}{a\rho_e(\omega^2 - v_{Ae}^2 k^2)} & -\tau_L < \tau < \tau_R, . \\ \dfrac{-C_R e^{-\tau}}{a\rho_R(\omega^2 - v_{AR}^2 k^2)} & \tau > \tau_R. \end{cases} \tag{3.14}$$

Finally, applying the boundary conditions (3.5) to equations (3.12) and (3.14) leads to the dispersion relation

$$F^2\omega^4(\rho_L - \rho_e)(\rho_R - \rho_e) = [(\rho_L + \rho_e)\omega^2 - 2\rho_e v_A^2 k^2][(\rho_R + \rho_e)\omega^2 - 2\rho_e v_A^2 k^2] \tag{3.15}$$

with solutions

$$\omega_\pm^2 = \frac{\omega_{Ae}^2\{\zeta_L + \zeta_R + 2 \pm \sqrt{(\zeta_L - \zeta_R)^2 + 4(\zeta_L - 1)(\zeta_R - 1)F^2}\}}{(\zeta_L + 1)(\zeta_R + 1) - (\zeta_L - 1)(\zeta_R - 1)F^2}. \tag{3.16}$$

Here we introduced the notation $F = \exp[-(\tau_L + \tau_R)]$, which is a geometrical factor, and the density contrasts $\zeta_L = \rho_L/\rho_e$ and $\zeta_R = \frac{\rho_R}{\rho_e}$. We only recover two eigenfrequencies of the system, as opposed to the four frequencies found in the numerical simulations. Van

Doorsselaere et al. (2008) [39] attribute this difference to the long-wavelength approximation. We can see that if we take the limit $\rho_L \to \rho_e$ in (3.16), then we recover the external Alfvén speed and the kink frequency for the right loop. An important corollary to (3.16) is that in the limit $\tau_L + \tau_R \to \infty$ we have

$$\omega_+ \to \max(\omega_{kL}, \omega_{kR}), \qquad \omega_- \to \min(\omega_{kL}, \omega_{kR}). \tag{3.17}$$

This will be used in the next section when we classify the different systems as standard or anomalous. First we will say a few words about the initial value problem.

Luna et al. (2008) [21] studied the reaction of the loops to an initial pulse applied to the system, with the incidence angle equal to $\beta$ (as measured with respect to the positive $x$-axis). In the stationary state, the system will eventually oscillate in a superposition of the four eigenmodes of the system. For $\beta = 0$, the system will eventually oscillate as a superposition of only the $S_x$ and $A_x$ modes, while for $\beta = \pi/2$, the system reaches a steady state for which only the eigenmodes $S_y$ and $A_y$ are present. When the incidence angle is approximately $0 \leq \alpha \lesssim 50$, a stationary state occurs in which the system behaves as a pair of oscillators which are $\pi/2$ out of phase and which alternatingly receive energy from the other tube in a beating phenomenon.

## 3.3 Standard and anomalous systems

One can show that the polarization of the displacement appearing in the analytical treatment of Van Doorsselaere et al. (2008) [39] in the limit $\tau \to \infty$ (which corresponds to $y \to 0$ and $x \to \pm a$) for $m = 1$ can be given in cartesian coordinates by

$$\xi_L = (-A\cos\sigma_0, A\sin\sigma_0) \tag{3.18}$$
$$\xi_R = (B\cos\sigma_0, B\sin\sigma_0) \tag{3.19}$$

with

$$A = \frac{C_L}{2a\rho_L(\omega^2 - \omega_{AL}^2)}, \qquad B = \frac{C_R}{2a\rho_R(\omega^2 - \omega_{AR}^2)}. \tag{3.20}$$

Hence $\sigma_0$ determines the angle of polarization of the two tubes. For the positive frequency $\omega_+$, it can be shown that $\mathrm{sgn}(C_L) = \mathrm{sgn}(C_R)$, hence $\mathrm{sgn}(A) = \mathrm{sgn}(B)$ and the motion of the tubes is always symmetric with respect to the $y$-axis. For $\sigma_0 = 0$ we recover the $A_x$-mode of Luna et al. (2008) [21], while for $\sigma_0 = \pi/2$ we recover the $S_y$-mode. Hence these two modes are merged in the analytical treatment. In agreement with Luna et al. (2008) [21] these two modes correspond to the highest frequency. For a general angle $\sigma_0$, the tubes move symmetrically with respect to the $y$-axis in the $xy$-plane as shown in Figure (3.3) (left).

For the lower frequency, the polarization of the displacement vector depends on the two inequalities

$$2\zeta_L < \zeta_R + 1 + (\zeta_R - 1)F^2 \tag{3.21}$$
$$2\zeta_R < \zeta_L + 1 + (\zeta_L - 1)F^2. \tag{3.22}$$

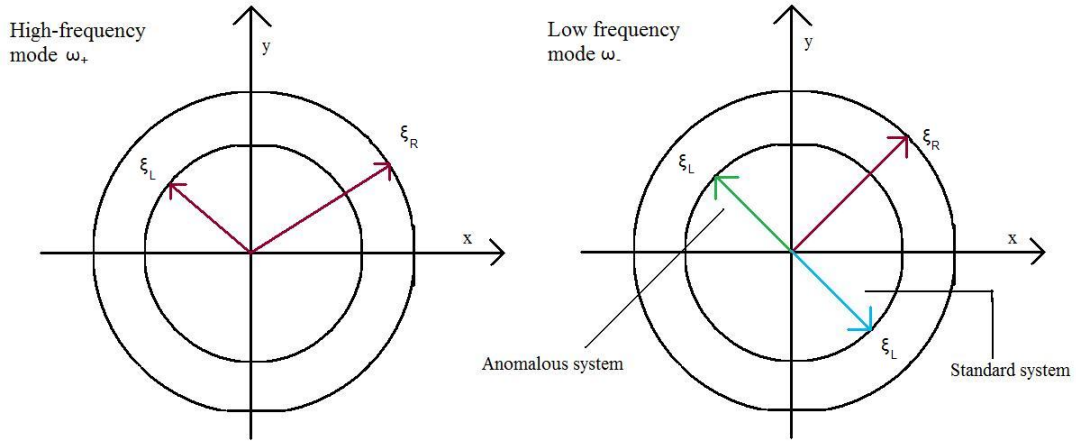


Figure 3.3: Left: Displacement vector in cartesian coordinates corresponding with the higher frequency $\omega_+$ Right: Displacement vector in cartesian coordinates corresponding with the lower frequency $\omega_-$. A subdivision must be made for standard and anomalous systems.

If none of these two inequalities is satisfied, it can be shown that $C_L$ and $C_R$ (hence $A$ and $B$) have opposite signs when $\omega = \omega_-$. Then from equations (3.18) and (3.19) it follows that the displacement vector of the two tubes is symmetric with respect to the $x$-axis. For $\sigma_0 = 0$ we recover the $S_x$-mode, while for $\sigma_0 = \pi/2$ we recover the $A_y$-mode. For a general angle $\sigma_0$, the tubes move symmetrically with respect to the $x$-axis in the $xy$-plane as shown in figure (3.3) (right). If one inequality is satisfied (they cannot be satisfied simultaneously) then we have again $\mathrm{sgn}(A) = \mathrm{sgn}(B)$ and the same analysis as for the positive frequency applies. Hence there are two $A_x$ — $S_y$ - modes.

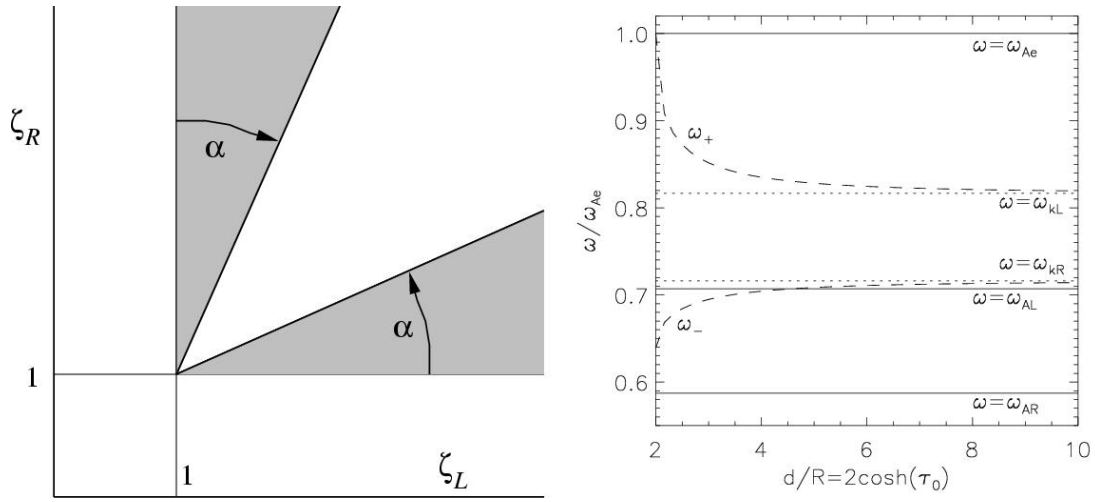


Figure 3.4: Left: Regions corresponding with standard or anomalous systems as a function of $\zeta_L$ and $\zeta_R$ for a fixed value of $F$. The shades zones correspond to the regions with anomalous behavior. The angle $\alpha$ is calculated in the text. Right: Plot of the eigenfrequencies as a function of tube separation. The internal and external Alfvén and kink frequencies are also plotted in full, respectively dotted lines. In this particular example $\zeta_L = 2$ and $\zeta_R = 2.9$ and $\tau_L = \tau_R =: \tau_0$ (from Van Doorsselaere et al. (2008) [39] )

For each value of $F$, one can define three regions in the $\zeta_L\zeta_R$-plane as shown in Figure

(3.4) (left). The shaded areas correspond to anomalous behavior, while the unshaded area corresponds to the standard behavior. Let us suppose in the remainder of this section that $\zeta_L \leq \zeta_R$ and, for simplicity, $\tau_L = \tau_R = \tau_0$. Then inequality (3.22) can never be satisfied. In the upper-left area, inequality (3.21) is satisfied. The angle $\alpha$ in Figure (3.4) (left) determines the limiting case for which the inequality (3.21) becomes an equality. Hence $\alpha$ can be calculated as follows:

$$\tan\alpha = \frac{\zeta_L - 1}{\zeta_R - 1} = \frac{\zeta_R + 1 + (\zeta_R - 1)F^2 - 2}{2(\zeta_R - 1)} = \frac{1 + F^2}{2}. \tag{3.23}$$

By definition of $F$, we have $\frac{1}{2} < \tan\alpha < 1$ or $29,51° < \alpha < 45°$. From this the following conclusions can be drawn. The line $\zeta_L = \zeta_R$ in Figure (3.4) (left) always lies in the region corresponding to standard behavior. This is why Luna et al. (2008) did not find the anomalous behavior, since they only considered two identical tubes. When $\zeta_L \neq \zeta_R$ equation (3.23) shows that we can always find a value of $\tau_0$ small enough making $F^2$ large enough such that the system becomes anomalous when the tubes are close to one another (compared to their radius). Moreover (and this is not mentioned in the paper of Van Doorsselaere et al. (2008) [39]), we can see from the lower bound on $\alpha$ that if the density contrasts $\zeta_L$ and $\zeta_R$ satisfy

$$\frac{\zeta_L - 1}{\zeta_R - 1} \leq \frac{1}{2} \quad \Leftrightarrow \quad 2\zeta_L \leq \zeta_R + 1 \quad \Leftrightarrow \quad \frac{2\zeta_L}{1 + \zeta_R} \leq 1 \tag{3.24}$$

then the system will always exhibit the anomalous behavior, independent of the separation distance between the two tubes. A mathematical way of stating condition (3.24) is that the left (low-density) tube has a density $\rho_L$ which is smaller than the mean density of the outer plasma $\rho_e$ and the plasma in the right (high-density) tube $\rho_R$.

A physical interpretation of the standard and anomalous behavior of the system of two parallel tubes was given by Van Doorsselaere et al. (2008) [39]. The kink and Alfvén frequencies of the two tubes (still assuming $\zeta_L \leq \zeta_R$) satisfy the series of inequalities $\omega_{AR}^2 \leq \omega_{AL}^2 \leq \omega_{kL}^2 \leq \omega_{Ae}^2$ and $\omega_{AR}^2 \leq \omega_{kR}^2 \leq \omega_{kL}^2 \leq \omega_{Ae}^2$, as can be readily calculated. The limits (3.17) imply that $\omega_-$ is a strictly increasing function which tends to $\omega_{kR}$ as $d/R \to \infty$. As one can see from Figure (3.4) (right) in a particular case (but this is true in general), when $\zeta_L \neq \zeta_R$ a value of $d/R$ exists such that the lower frequency drops below the Alfvén frequency. This is the point where the system becomes anomalous since the left tube does not react to the fast global oscillation of the right tube. The global frequency of the system exceeds the cutoff frequency for the magnetosonic oscillations of the left tube, which is the Alfvén frequency $\omega_{AL}$.

The position from which the tubes start to exhibit anomalous behavior is determined by the relative positions of $\omega_{kR}^2$ and $\omega_{AL}^2$. From the definitions of the kink frequency (2.12) and the Alfvén frequency we find that

$$\omega_{kR}^2 = \frac{\rho_R\omega_{AR}^2 + \rho_e\omega_{Ae}^2}{\rho_R + \rho_e} = \frac{2\rho_L\omega_{AL}^2}{\rho_R + \rho_e} = \frac{2\zeta_L}{1 + \zeta_R}\,\omega_{AL}^2. \tag{3.25}$$

When $\frac{2\zeta_L}{1+\zeta_R} \geq 1$, the system can exhibit both the standard and anomalous behavior, depending on the distance between the tubes. When $\frac{2\zeta_L}{1+\zeta_R} \leq 1$, the kink frequency for the right tube lies below the Alfvén frequency for the left tube, which means that the

system is always anomalous. This condition is exactly the condition (3.24) which we found before. In the numerical example of Figure (3.4) (right), we have that $\frac{2\zeta_L}{1+\zeta_R} = 4/3.9$ which is just above one, probably for visibility purposes. The fact that the authors chose these particular values for $\zeta_L$ and $\zeta_R$ suggests that they are also aware of inequality (3.24) even though it is not mentioned in their paper. This discussion gives a physical explanation of the standard and anomalous behavior found in the systems. Now that we know the behavior of the interface system, we can include dissipation in the next chapter.

# Chapter 4

# Resonant damping of MHD waves in a system of two coronal loops

In this chapter we take the next logical step and combine the results and methods of the previous two chapters to study the damped oscillations of a system of two coronal loops. The first numerical studies in this respect were performed by Terradas et al. (2008) [36], who studied the damped oscillations of a multistranded loop (i.e. a structure which looks like one coronal loop, which actually consists of several physically similar smaller loops, called strands, with different densities inside) using a 2D numerical code. Ofman (2009) [27] modelled a system of four parallel coronal loops using a full 3-dimensional numerical code.

In Terradas et al. (2008) [36], the authors looked at an irregular initial configuration of a multistranded plasma with ten subloops. They also dropped the condition that the loop as a whole has a cylindrical geometry. In this more realistic setting, the authors solved the initial value problem. It was found that after an initial phase, the energy becomes concentrated at the regions where the oscillation frequency matches the local Alfvén frequency. This indicates that resonant absorption is a robust mechanism which is not greatly affected by the geometry of the problem.

We saw in the previous chapter how an initial perturbation of an identical two-loop system could give rise to a complex stationary state in which the system oscillates at a superposition of the four eigenmodes of the system. The analytical results of Van Doorsselaere et al. (2008) [39] allowed a more quantitative understanding of these oscillations, even though the lower and higher frequency modes found by Luna et al. (2008) [21] were both merged into one single high-frequency and low-frequency mode. A system of $N$ coronal loops is expected to have many eigenmodes, that have similar frequency and damping rate, as was already the case for the two-loop system of Luna et al. (2008) [21]. The simulations of Terradas et al. (2008) [36] should therefore be interpreted in terms of a superposition of these eigenmodes. However, the eigenmodes of more complex geometries are not yet well developed analytically. Hence developing analytical models for a system of coronal loops, including damping, has two concrete aims. Firstly, it should help interpret the results of observations and complex computer simulations as a superposition

of eigenmodes. Secondly, as mentioned before, a comparison of the predicted frequencies and damping times with observations also furthers coronal seismology.

Resonantly damped oscillations of a system of two coronal loops were first studied by Arregui et al. (2008) [2] using a Cartesian geometry. Later Robertson & Ruderman (2011) [31] refined their analysis, modeling each loop as a magnetic flux tube (since the properties of the kink mode in slabs and tubes are rather different). The analysis of the authors starts in the general setting of two flux tubes with different densities and radii inside and different thicknesses of the inhomogeneous layer. However, the calculation of the damping decrement is only done for the special case of two identical tubes. In this chapter, I first outline the method followed by Robertson & Ruderman (2011) [31] leading to the jump condition across the dissipative layer. Then I will exploit the TB assumption more consequently to derive a hitherto unknown dispersion relation for the damped oscillations of two, not necessarily identical, loops. This dispersion relation generalizes the results of Van Doorsselaere et al. (2008) [39] of Chapter 3, the results for damped oscillations of one magnetic flux tube of Goossens et al. (2009) [15] of Chapter 2 and the damping decrement found by Robertson & Ruderman (2011) [31]. Finally I will derive and discuss an expression for the damping decrement.

## 4.1 Derivation of the jump condition

**Equilibrium configuration and governing equations**
The equilibrium configuration for the system of two loops including an inhomogeneous layer is given by Figure (4.1). The equilibrium parameters are very similar to the ones in the last chapter, so I refer to that discussion for an interpretation of Figure (4.1).

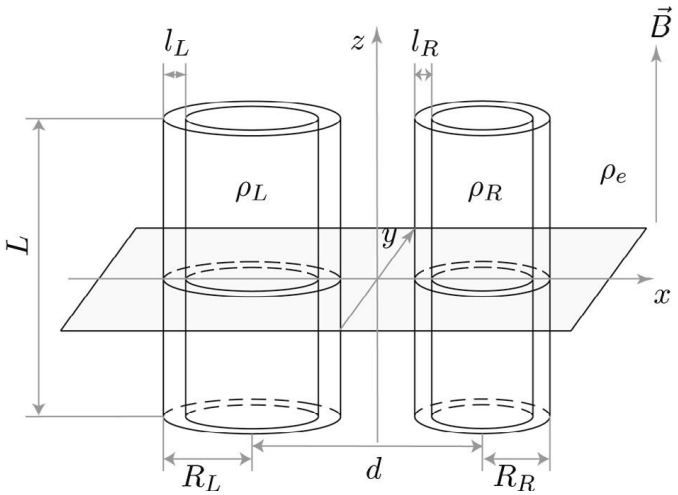


Figure 4.1: Sketch of the equilibrium configuration (from Robertson & Ruderman (2011) [31] )

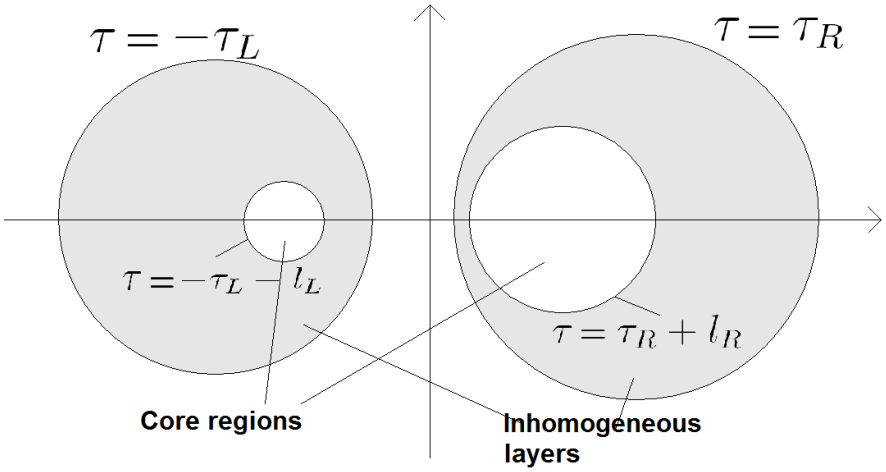


Figure 4.2: Annulus shape for thick inhomogeneous layers

We assume that the density profile is continuous at all boundaries. Hence we can write

$$\rho = \begin{cases} \rho_L & \tau < -\tau_L - l_L \\ \overline{\rho}_L(\tau) & -\tau_L - l_L \leq \tau \leq -\tau_L \\ \rho_e & -\tau_L < \tau < \tau_R \\ \overline{\rho}_R(\tau) & \tau_R \leq \tau \leq \tau_R + l_R \\ \rho_R & \tau > \tau_R + l_R \end{cases} \tag{4.1}$$

in which $\overline{\rho}_L(\tau)$ is a monotonically decreasing function such that $\overline{\rho}_L(-\tau_L - l_L) = \rho_L$ and $\overline{\rho}_L(-\tau_L) = \rho_e$, and $\overline{\rho}_R(\tau)$ is a monotonically increasing function such that $\overline{\rho}_R(\tau_R) = \rho_e$ and $\overline{\rho}_R(\tau_R + l_R) = \rho_R$.

A word of warning considering the configuration sketched in Figure 4.1 should be made: since we are working in bicylindrical coordinates, it could be the case that the thickness of the inhomogeneous annulus varies with angle, as shown in Figure 4.2 (and already alluded to at the beginning of Chapter 3). If we want to exclude these effects, we will have to assume a thin boundary layer $l_L \ll R_L$ and $l_R \ll R_R$ (the TB approximation also used in Section 2.4.).

We again use the cold plasma approximation. We include viscosity and linearize the viscous MHD equations, leading to

$$\rho \frac{\partial^2 \xi}{\partial t^2} = \frac{1}{\mu_0} (\nabla \times \mathbf{b}) \times \mathbf{B} + \frac{\partial}{\partial t} [\nabla(\overline{\nu} \nabla \cdot \xi) - \nabla \times (\overline{\nu} \nabla \times \xi)], \tag{4.2}$$

$$\mathbf{b} = \nabla \times (\xi \times \mathbf{B}). \tag{4.3}$$

Here $\overline{\nu}$ denotes the coefficient of shear viscosity. In chapter 2 we used the resistive MHD equations to study the damping in the dissipative layer. As we saw in section 2.4 in the case of a single loop, the damping decrement (2.40) is independent of the value of viscosity (or resistivity) itself, provided it is small enough. Hence there is no problem in using the viscous MHD equations.

These equations have to be supplemented with a set of regularity and boundary conditions. If we move far away from the tubes, we want that the perturbation of magnetic pressure

goes to zero: $p \to 0$ as $\tau^2 + \sigma^2 \to 0$. As in the previous chapter, the solutions have to be bounded when $\tau \to \infty$. To be able to use the analytical results from Chapter three, we also adopt the long wavelength approximation $\frac{d}{L} =: \varepsilon \ll 1$. Finally, we impose that the magnetic field lines are tied to the photosphere:

$$\xi_\perp(z = \pm L/2) = 0. \tag{4.4}$$

**Solution in the outer and core layers**

As in the previous setting, we will not solve the full set of resistive MHD equations. Since we can neglect viscosity everywhere but in a small dissipative layer, we use exactly the same simplifications as at the beginning of section 2.3. Since the damping decrement is independent of $\overline{\nu}$ we can specify any dependence of $\overline{\nu}$ on $\sigma$ and $\tau$ provided that the scale of variation of $\overline{\nu}$ is large compared to the dissipative layer. In particular we could set

$$\overline{\nu} = \frac{\rho(\tau)\nu}{(\cosh\tau - \cos\sigma)^2}, \tag{4.5}$$

where $\nu$ is assumed small. This mathematical trick greatly simplifies the calculations. Robertson and Ruderman (2011) [31] used this configuration to derive the evolution equations of magnetic pressure and displacement components. Since the derivation is rather similar as in chapter three, we only give the final results, which in the long-wavelength approximation are

$$P' = \Theta(\tau)\cos(\sigma - \sigma_0) - \Theta(0)\cos\sigma_0, \tag{4.6}$$

$$\Theta(\tau) = \begin{cases} C_L\, e^{\tau} & \tau \le -\tau_L - l_L, \\ C_1\, e^{\tau} + C_2\, e^{-\tau} & -\tau_L \le \tau \le \tau_R, \\ C_R\, e^{-\tau} & \tau \ge \tau_R + l_R, \end{cases} \tag{4.7}$$

$$\xi_\tau = \hat{\xi}_\tau(\tau)(\cosh\tau - \cos\sigma)\cos(\sigma - \sigma_0), \tag{4.8}$$

$$\hat{\xi}_\tau(\tau) = \begin{cases} \dfrac{C_L e^{\tau}}{a\rho_L(\omega^2 - v_{AL}^2 k^2)} & \tau \le -\tau_L - l_L, \\ \dfrac{C_1 e^{\tau} - C_2 e^{-\tau}}{a\rho_e(\omega^2 - v_{Ae}^2 k^2)} & -\tau_L \le \tau \le \tau_R, . \\ \dfrac{-C_R e^{-\tau}}{a\rho_R(\omega^2 - v_{AR}^2 k^2)} & \tau \ge \tau_R + l_R, \end{cases} \tag{4.9}$$

Also the $\sigma$-component is coupled to the system; this yields

$$\xi_\sigma = -\hat{\xi}_\sigma(\tau)(\cosh\tau - \cos\sigma)\sin(\sigma - \sigma_0). \tag{4.10}$$

Substituting (4.8) and (4.10) into (3.6) and neglecting terms of other $\varepsilon^2$, we find that

$$\frac{d\hat{\xi}_\tau}{d\tau} - \hat{\xi}_\sigma = 0. \tag{4.11}$$

Equation (4.11) will be useful in obtaining a jump condition across the inhomogeneous layer.

**Solution in the dissipative layer and jump conditions**

We can now combine these equations with the mathematical tools obtained in the second

chapter to find appropriate boundary conditions across the dissipative layer in the form of jump conditions. Using the thin boundary assumption, the main effect of the inhomogeneous layer will be the resonant damping of the eigenmodes, with the real part of the frequency being only slightly modified. Hence the resonant surfaces $\tau = \tau_{AL,R}$ satisfy to a very good approximation the relations

$$\omega_A(\tau_{AL}) = \omega, \qquad \omega_A(\tau_{AR}) = \omega, \tag{4.12}$$

where $\omega$ is equal to either $\omega_+$ or $\omega_-$, that are the eigenfrequencies of the interface system given by (3.16). In Chapter 3 we made the distinction between standard and anomalous systems of magnetic flux tubes. Assume again that $\rho_L \leq \rho_R$. Then we recover the series of inequalities $\omega_{AR}^2 \leq \omega_{AL}^2 \leq \omega_{kL}^2 \leq \omega_{Ae}^2$ and $\omega_{AR}^2 \leq \omega_{kR}^2 \leq \omega_{kL}^2 \leq \omega_{Ae}^2$ as in Chapter three. For the right tube, we have $\omega_A(\tau_R) \in [\omega_{AR}^2, \omega_{Ae}^2]$; this means that there will be a resonant surface for both eigenfrequencies. For the left tube, we find $\omega_A(\tau_L) \in [\omega_{AL}^2, \omega_{Ae}^2]$. Since $\omega_{AL}^2 \leq \omega_{kL}^2 \leq \omega_+^2 \leq \omega_{Ae}^2$, there will always be a resonance for the higher frequency. For the lower frequency we find for standard systems that $\omega_{AL}^2 \leq \omega_-^2 \leq \omega_{kR}^2 \leq \omega_{Ae}^2$, which implies resonance in the left tube. In anomalous systems, however, there holds $\omega_-^2 < \omega_{kR}^2 \leq \omega_{AL}^2$. This means that no resonant surface exists in the tube with the lowest density (hence with the highest Alfvén speed).

All of this is summarized in the following table:

| | Left tube (low density) | Right tube (high density) |
|---|---|---|
| Standard systems | $\omega_+, \omega_-$ | $\omega_+, \omega_-$ |
| Anomalous systems | $\omega_+$ | $\omega_+, \omega_-$ |

Again we introduce a new variable

$$s = \frac{\tau - \tau_A}{\delta}, \qquad \delta = \left(\frac{\omega_0 \nu}{a^2 |\Delta|}\right)^{1/3}$$

for which $\omega_0$ denotes either $\omega_+$ or $\omega_-$ and $|\Delta| = \frac{d\omega_A^2}{d\tau}_{(\tau=\tau_{AL,R})}$. If we denote the region of validity of the linear Taylor expansion of $\omega_A^2$ as $[-\tau_{lin}, \tau_{lin}]$, then letting $\tau \to \pm\tau_{lin}$ corresponds formally to $s \to \pm\infty$. The jump of any quantity $f$ across the dissipative layer is defined as

$$[f] = \lim_{s\to\infty} (f(s) - f(-s)). \tag{4.13}$$

We can now calculate the jump conditions. Now that we understand how this is done, I refer to the paper of Robertson & Ruderman (2011) [31] for the calculations, which in the end yield

$$[\Theta] = 0, \tag{4.14}$$

$$[\hat{\xi}_\tau] = -\frac{i\pi\Theta(\tau_A)}{a\rho_A|\Delta|}. \tag{4.15}$$

These expressions are valid in the case of standard systems, in which there exists a resonant position in both loops. Now consider an anomalous system with $\rho_L \leq \rho_R$. We then know that there does not exist a resonant position in the left (lower-density) tube. In this case,

an identical calculation still holds for the right tube. This means that the jump condition (4.15) should be adapted as follows:

$$[\hat{\xi}_{\tau,L}] = 0, \qquad [\hat{\xi}_{\tau,R}] = -\frac{i\pi\Theta(\tau_{AR})}{a\rho_{AR}|\Delta_R|}. \tag{4.16}$$

Going back to standard systems, by (4.15) the jump in $\hat{\xi}_\tau$ is the same for both loops. This gives rise to a fundamental question. When we use bicylindrical coordinates, letting $\tau$ (or equivalently, $s$) increase, corresponds to moving from the inside of the left tube to the outside region, and finally into the right tube as shown in Figure 4.3.

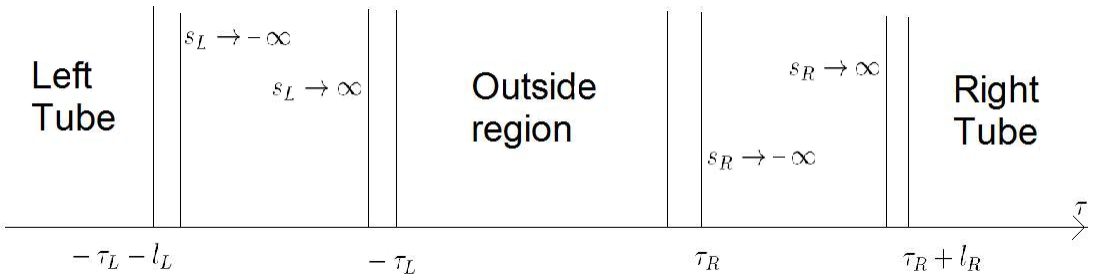


Figure 4.3: Overview of the different regions and the jump conditions

This implies that in the left tube, the limit $s_L \to \infty$ corresponds with moving from the inside of the tube to the outside region, whereas for the right tube, the limit $s_R \to \infty$ corresponds with a movement from the outside region to the inside of the right tube. The nature of the jump condition is thus opposite whether we consider the left, respectively the right tube. If we compare the sign of the jumps (which are still hidden in the sign of $\Theta(\tau_A)$) for both loops, we find, using equations (4.14) and (4.7), that

$$[\hat{\xi}_{\tau,L}] = -\frac{i\pi\Theta(\tau_{AL})}{a\rho_{AL}|\Delta_L|} = -\frac{i\pi\Theta(-\tau_L - l_L)}{a\rho_{AL}|\Delta_L|} = \frac{i\pi C_L e^{-\tau_L - l_L}}{a\rho_{AL}|\Delta_L|}, \tag{4.17}$$

$$[\hat{\xi}_{\tau,R}] = -\frac{i\pi\Theta(\tau_{AR})}{a\rho_{AR}|\Delta_R|} = -\frac{i\pi\Theta(\tau_R + l_R)}{a\rho_{AR}|\Delta_R|} = \frac{i\pi C_R e^{-\tau_R - l_R}}{a\rho_{AR}|\Delta_R|} \tag{4.18}$$

However, in general the two constants $C_L$ and $C_R$ will be complex numbers, hence it is of no use to speak about its sign. We do not have to worry about the opposite 'sign' of these jumps, as this does not indicate (as is the case in cylindrical geometry) that the eigenfunctions correspond to amplifying waves in one of the tubes. This has to do with the nature of the bicylindrical coordinate system. In the next subsections we will derive expressions of the imaginary part of the eigenfrequencies, proving that the dissipative layers are sinks of energy for the waves.

## 4.2 The dispersion relation

### 4.2.1 Thin boundary assumption

From the previous section Robertson & Ruderman (2011) [31] proceed as follows. They integrate the ideal MHD solution in the nonuniform equilibrium to connect these solutions

with the jump conditions (4.14) and (4.15). This was put forward in Section 2.4 as the proper way to proceed in general when we have no further assumptions on the inhomogeneous layer. It finally results in a jump condition across the inhomogeneous layer in the form of a principal value integral for $\hat{\xi}_\tau$:

$$[\hat{\xi}_\tau] = (\hat{\xi}_\tau(-\tau_0) - \hat{\xi}_\tau(-\tau_0 - l)) - \frac{\Theta_A}{a}\,\mathcal{P}\int_{-\tau_0-l}^{-\tau_0} \frac{dt}{\overline{\rho}(t)[\omega_0^2 - \omega_A^2(t)],} \tag{4.19}$$

and a jump condition for $\Theta$ in the form of an integral without singularities:

$$\Theta(-\tau_0) - \Theta(-\tau_0 - l) = a\hat{\xi}_\tau(-\tau_0)\int_{-\tau_0-l}^{-\tau_0} \overline{\rho}(t)[\omega_0^2 - \omega_A^2(t)]dt. \tag{4.20}$$

The authors then use the expressions for $\hat{\xi}_\tau(-\tau_0) - \hat{\xi}_\tau(-\tau_0 - l)$ and $\Theta(-\tau_0) - \Theta(-\tau_0 - l)$ from (4.19) and (4.20) as boundary conditions for equations (4.9) and (4.7). Thereafter, they only keep linear terms in the calculation of the damping. Because they keep the term containing the principal value integral, to keep the calculations tractable they ultimately have to simplify to a system of two identical tubes. However, in the expression for the damping decrement, the principal value integral only appears as a phase shift contributing to the real part of $\omega$ (Robertson & Ruderman, 2011 [31]).

Furthermore, in this case the thin boundary assumption has already been invoked in Section 4.1 (to be able to present $\tau$ as the local radial coordinate, we must by definition (of 'local') assume that $l \ll R$) and Section 4.2 (in the Ansatz to equation (4.12)). As explained in Section 2.4., using the thin boundary assumption we can assume that the inhomogeneous layer and the dissipative layer coincide and forget about the integrals (4.19) and (4.20) altogether. Since the principal value integral did not appear in the end result for the damping decrement anymore in Robertson & Ruderman, we ultimately do not lose any information by doing this. In the remainder of the chapter, we will see how imposing this assumption from the start allows us to obtain more general results for systems of two, not necessarily identical, loops.

### 4.2.2 Derivation of the dispersion relation

We will consider a standard system during the derivations in this subsection. Specific results for anomalous systems will be discussed in the next subsection. Using the thin boundary assumption and jump conditions (4.15) and (4.14), we obtain

$$(\hat{\xi}_\tau(-\tau_0) - \hat{\xi}_\tau(-\tau_0 - l)) = [\hat{\xi}_\tau] = -\frac{i\pi\Theta(\tau_A)}{a\rho_A|\Delta|} \tag{4.21}$$

$$\Theta(-\tau_0 - l) - \Theta(-\tau_0) = 0. \tag{4.22}$$

These two equations are the appropriate boundary conditions to be used in equations (4.7) and (4.9). Since $\Theta$ is a constant along the annuli, we can take $\Theta_{AL} = \Theta(-\tau_L - l_L) = C_1 e^{-\tau_L} + C_2 e^{\tau_L}$ in the left annulus and $\Theta_{AR} = \Theta(\tau_R + l_R) = C_1 e^{\tau_R} + C_2 e^{-\tau_R}$ in the right

annulus. This yields the following system of equations:

$$C_L e^{-\tau_L - l_L} = C_1 e^{-\tau_L} + C_2 e^{\tau_L} \tag{4.23}$$

$$C_R e^{-\tau_R - l_R} = C_1 e^{\tau_R} + C_2 e^{-\tau_R} \tag{4.24}$$

$$\frac{C_1 e^{-\tau_L} - C_2 e^{\tau_L}}{\rho_e(\omega^2 - \omega_{Ae}^2)} - \frac{C_L e^{-\tau_L - l_L}}{\rho_L(\omega^2 - \omega_{AL}^2)} = \frac{-i\pi(C_1 e^{-\tau_L} + C_2 e^{\tau_L})}{\rho_{AL}|\Delta_L|} \tag{4.25}$$

$$\frac{-C_R e^{-\tau_R - l_R}}{\rho_R(\omega^2 - \omega_{AR}^2)} - \frac{C_1 e^{\tau_R} - C_2 e^{-\tau_R}}{\rho_e(\omega^2 - \omega_{Ae}^2)} = \frac{-i\pi(C_1 e^{\tau_R} + C_2 e^{-\tau_R})}{\rho_{AR}|\Delta_R|}. \tag{4.26}$$

This system has a nontrivial solution if and only if its coefficient matrix has determinant equal to zero. We now introduce the notation

$$L = \rho_L(\omega^2 - \omega_{AL}^2) \qquad F = e^{-(\tau_L + \tau_R)}$$

$$E = \rho_e(\omega^2 - \omega_{Ae}^2) \qquad I_L = \frac{i\pi}{\rho_A|\Delta_L|}$$

$$R = \rho_R(\omega^2 - \omega_{AR}^2) \qquad I_R = \frac{i\pi}{\rho_A|\Delta_R|}.$$

The density $\rho_A$ at the Alfvén resonant point only depends on the eigenfrequency $\omega_\pm$, hence it is the same for both loops:

$$\rho(\tau = \tau_{AL}) = \frac{B^2k^2}{\mu\omega_A^2(\tau_{AL})} = \frac{\rho_e\omega_{\mathrm{Ae}}^2}{\omega_0^2} = \frac{B^2k^2}{\mu\omega_A^2(\tau_{AR})} = \rho(\tau = \tau_{AR}). \tag{4.27}$$

We can write the system of equations (4.28) — (4.31) in matrix form as $MC = 0$ with the order of variables $C = (C_L\, C_1\, C_2\, C_R)^T$. Using the notation from above, the condition that $\det(\mathrm{M}) = 0$ can be written as

$$0 = \det \begin{pmatrix} -1 & 1 & e^{2\tau_L} & 0 \\ 0 & e^{2\tau_R} & 1 & -1 \\ \frac{1}{L} & \frac{1}{E} + I_L & e^{2\tau_L}\left(\frac{-1}{E} + I_L\right) & 0 \\ 0 & e^{2\tau_R}\left(\frac{1}{E} - I_R\right) & \frac{-1}{E} - I_R & \frac{1}{R} \end{pmatrix}.$$

In this step we also divided the coefficients appearing with $C_L$ (in the first column) by $e^{-\tau_L - l_L}$ and the coefficients of $C_R$ by $e^{-\tau_R - l_R}$. If we now develop this determinant to its first column (for example) and rearrange the terms, we get the following dispersion relation for $\omega^2$:

$$F^2[L - E(1 - LI_L)][R - E(1 - RI_R)] = [L + E(1 - LI_L)][R + E(1 - RI_R)]. \tag{4.28}$$

This dispersion relation for resonantly damped modes of a system of two cylinders is hitherto unknown in the literature to the best of my knowledge. Since $L, E$ and $R$ are both functions of $\omega^2$ equation (4.28) is an equation for $\omega^2$ of degree four. To calculate its roots using the quartic formula would give us an intractable equation concealing the physics of the problem. Furthermore, we can only expect accuracy up to first order in the damping decrement; which requires a linearisation with respect to the imaginary part of $\omega$. In the next subsection, we will solve equation (4.28) in the limit of small damping. However, let us first look at some limiting cases.

**The case without dissipation**
In this case we take $I_L = 0$, $I_R = 0$ such that (4.28) reduces to $F^2[L-E][R-E] = [L+E][R+E]$. Substituting the expressions for $L, R$ and $E$ then yields

$$F^2\omega^4(\rho_L - \rho_e)(\rho_R - \rho_e) = [(\rho_L + \rho_e)\omega^2 - 2\rho_e v_A^2 k^2][(\rho_R + \rho_e)\omega^2 - 2\rho_e v_A^2 k^2]. \tag{4.29}$$

This is exactly (3.15).

**The case for which the loops are displaced far away from each other**
This situation corresponds to $\tau_L + \tau_R \to \infty$: even though the loop centers will remain at a finite distance at the points for which $x = \pm a$, compared with their radius (which is the typical length scale of the loops), the loops will diverge infinitely far apart from each other. Mathematically, this implies $F \to 0$, such that equation (4.28) splits into two factors:

$$[L + E(1 - LI_L)][R + E(1 - RI_R)] = 0. \tag{4.30}$$

Let us look at the first factor in the limiting case of linear damping. Write therefore $\omega^2 = \omega_0^2 + 2i\omega_0\gamma$. Here $\omega_0$ is the zero-order solution for this equation, i.e. the kink frequency for the left loop. Then we also decompose:

$$L = \rho_L(\omega^2 - \omega_{\mathrm{AL}}^2) = \rho_L(\omega_{\mathrm{kL}}^2 - \omega_{\mathrm{AL}}^2) + 2\rho_L i\omega_{\mathrm{kL}}\gamma =: L_0 + L_\gamma \tag{4.31}$$

and the same for $E$ and $R$. First linearizing the first factor (4.30) and then substituting these expressions we find

$$\underbrace{L_0 + E_0}_{\text{zero-order solution}} + L_\gamma + E_\gamma - E_0 L_0 I_L = 0$$

$$\Leftrightarrow 2i\gamma\omega_{\mathrm{kL}}(\rho_L + \rho_e) = \frac{\rho_L(\omega_{\mathrm{kL}}^2 - \omega_{\mathrm{AL}}^2)\rho_e(\omega_{\mathrm{kL}}^2 - \omega_{\mathrm{Ae}}^2)i\pi}{\rho(\tau_{\mathrm{AL}})|\Delta_L(\tau_{\mathrm{AL}})|}.$$

Because of the identities $\omega_{\mathrm{kL}}^2 - \omega_{\mathrm{Ae}}^2 = \frac{\rho_L(\omega_{\mathrm{AL}}^2 - \omega_{\mathrm{Ae}}^2)}{\rho_L + \rho_e}$ and $\omega_{\mathrm{kL}}^2 - \omega_{\mathrm{AL}}^2 = \frac{-\rho_e(\omega_{\mathrm{AL}}^2 - \omega_{\mathrm{Ae}}^2)}{\rho_L + \rho_e}$ we recover that

$$\frac{\gamma}{\omega_{\mathrm{kL}}} = \frac{-\pi}{2\omega_{\mathrm{kL}}^2} \frac{\rho_L^2\rho_e^2(\omega_{\mathrm{AL}}^2 - \omega_{\mathrm{Ae}}^2)^2}{(\rho_L + \rho_e)^3\rho(\tau_{\mathrm{AL}})|\Delta_L(\tau_{\mathrm{AL}})|}. \tag{4.32}$$

This is almost equation (2.40), with the differences that we evaluate $|\Delta_L(\tau_{AL})|$ in bicylindrical coordinates, and that a factor of $1/R$ is missing which does appear in (2.40). This is logical since we work in bicylindrical coordinates. The analysis for the right tube is exactly the same, leading to the same equation but with the subscript 'L' replaced by 'R'. This shows that in both loops, the imaginary part of the solution corresponds to a damping mechanism, as was derived in Section 4.1. using energy considerations.

In the general case, it is not easy to switch coordinate systems and write $|\Delta_L|$ in terms of $r$. In fact, it turns out to be impossible to prevent the tube thickness to go to zero when $\tau_L + \tau_R \to \infty$ in a bicylindrical coordinate system when using the long-wavelength approximation. This I will show now.

Because of the equations of the bicylindrical coordinate system (3.2) we have

$$\frac{R_L}{L_L} = \frac{ak}{n\pi\sinh(\tau_L)} \tag{4.33}$$

in which, for purposes of clarity, we focus on the expressions for the left tube. Since $\sinh(\tau_L) \to \infty$ as $\tau_L \to \infty$ (like $e^{\tau_L}$), we should additionally make sure that $k \to \infty$ in this limit to prevent the tubes from collapsing to a zero thickness. However, the long-wavelength approximation together with (3.2) imply that

$$\frac{d}{L} = \frac{a(\coth\tau_L + \coth\tau_R)}{L} \quad \overset{\tau\to\infty}{\longrightarrow} \quad \frac{2a}{L} = \frac{2ak}{\pi} \ll 1 \tag{4.34}$$

It is now clear that equation (4.34) can never be satisfied if $R_L/L_L$ must remain finite. This means that we cannot prevent the tubes from becoming infinitely thin in the limit $\tau_L + \tau_R \to \infty$ making a direct comparison with the earlier results in cylindrical geometry difficult.

Nevertheless, it is still possible to compare (4.32) with equation (2.40). Let us first assume that the density profile is linear throughout the inhomogeneous layer $\tau \in \{-\tau_L - l_L, -\tau_L\}$:

$$\overline{\rho}_L(\tau) = \rho_e \left(1 + (1-\zeta_L)\frac{\tau + \tau_L}{l_L}\right). \tag{4.35}$$

With this density profile we have

$$|\Delta_L(\tau_{\mathrm{AL}})| = \frac{\omega_{\mathrm{kL}}^4(\zeta_L - 1)}{l_L \omega_{\mathrm{Ae}}^2}. \tag{4.36}$$

Furthermore, the density at the resonant point can be calculated via equation (4.27). Substituting equations (4.27) and (4.36) into (4.32) leads to a massive simplification, yielding in the end

$$\frac{\gamma}{\omega_{\mathrm{kL}}} = \frac{-\pi}{8}\frac{l_L(\zeta_L - 1)}{\zeta_R + 1}. \tag{4.37}$$

Remember that in general, the thickness of the nonuniform layer $l_L$ is a function of $\sigma$. Let us introduce the mean density of the inhomogeneous layer

$$l_{\mathrm{avg,L}} = \frac{1}{2\pi R_L}\int_0^{2\pi} l_L(\sigma) ds(\sigma). \tag{4.38}$$

Of course, a similar definition can be used for the right tube. Then it can be shown (see Robertson & Ruderman (2011) [31]) that in this case, $l_{\mathrm{avg,\,L}}$ is equal to

$$l_{\mathrm{avg,L}} = l_L R_L \coth\tau_L \quad \overset{\tau\to\infty}{\longrightarrow} \quad l_L R_L. \tag{4.39}$$

Substituting this equation into (4.37) then yields in the end

$$\frac{\gamma}{\omega_{\mathrm{kL}}} = \frac{-\pi}{8}\frac{l_{\mathrm{avg,L}}(\zeta_L - 1)}{R_L(\zeta_R + 1)}. \tag{4.40}$$

In conclusion, using the mean thickness of the inhomogeneous layer, it is possible to compare equations (4.32) and (2.40). In the case of a linear density profile, it can be shown that (2.40) also reduces to (4.40). This means that the dispersion relation (4.28) also generalises the results found for cylindrical geometry.

## 4.3 Derivation of damping decrement

We will now look at the limiting case of small damping for the dispersion relation we found. Therefore we again use the decomposition (4.31) for $L, E$ and $R$. Now $\omega_0$ stands for one of the two-loop interface eigenfrequencies (3.16). Linearizing the dispersion equation (4.28) yields

$$\begin{aligned} F^2[&\underbrace{(L_0-E_0)(R_0-E_0)}+(L_0-E_0)(R_\gamma-E_\gamma+E_0R_0I_R)+(R_0-E_0)(L_\gamma-E_\gamma+L_0E_0I_L)] \\ &= \underbrace{(L_0+E_0)(R_0+E_0)}_{\text{zero-order solution}}+(L_0+E_0)(R_\gamma+E_\gamma-E_0R_0I_R)+(R_0+E_0)(L_\gamma+E_\gamma-L_0E_0I_L). \end{aligned} \tag{4.41}$$

Since $L_\gamma \pm E_\gamma = 2i\gamma\omega_0(\rho_L \pm \rho_e)$ and $R_\gamma \pm E_\gamma = 2i\gamma\omega_0(\rho_R \pm \rho_e)$, we can collect the terms with $\gamma$ and rewrite (4.41) as

$$\begin{aligned} 2i\gamma\omega_0[&F^2\{(L_0-E_0)(\rho_R-\rho_e)+(R_0-E_0)(\rho_L-\rho_e)\}-\{(L_0+E_0)(\rho_R+\rho_e)+(R_0+E_0)(\rho_L+\rho_e)\}] \\ &= -E_0R_0I_R\{(L_0+E_0)+F^2(L_0-E_0)\}-L_0E_0I_L\{(R_0+E_0)+F^2(R_0-E_0)\}. \end{aligned} \tag{4.42}$$

We now try to simplify (4.42) as much as possible. Using the notations

$$X=(\zeta_L-\zeta_R)^2+4(\zeta_L-1)(\zeta_R-1)F^2, \qquad Q=(\zeta_L+1)(\zeta_R+1)-(\zeta_L-1)(\zeta_R-1)F^2$$

we can use the following auxiliary results:

$$\begin{aligned} L_0 &= \frac{\rho_e\omega_{Ae}^2}{Q}\{\zeta_L^2+\zeta_L-\zeta_R-1+(\zeta_L-1)(\zeta_R-1)F^2\pm\zeta_L\sqrt{X}\} \\ R_0 &= \frac{\rho_e\omega_{Ae}^2}{Q}\{\zeta_R^2+\zeta_R-\zeta_L-1+(\zeta_R-1)(\zeta_L-1)F^2\pm\zeta_R\sqrt{X}\} \\ E_0 &= \frac{\rho_e\omega_{Ae}^2}{Q}\{1-\zeta_L\zeta_R+(\zeta_R-1)(\zeta_L-1)F^2\pm\sqrt{X}\} \\ L_0-E_0 &= \frac{\rho_e\omega_{Ae}^2}{Q}\{(\zeta_L-\zeta_R)(\zeta_L+1)-2(1-\zeta_L\zeta_R)\pm(\zeta_L-1)\sqrt{X}\} \\ L_0+E_0 &= \frac{\rho_e\omega_{Ae}^2}{Q}\{(\zeta_L-\zeta_R)(\zeta_L+1)+2(1-\zeta_L\zeta_R)F^2\pm(\zeta_L+1)\sqrt{X}\} \\ R_0-E_0 &= \frac{\rho_e\omega_{Ae}^2}{Q}\{(\zeta_R-\zeta_L)(\zeta_R+1)-2(1-\zeta_L\zeta_R)\pm(\zeta_R-1)\sqrt{X}\} \\ R_0+E_0 &= \frac{\rho_e\omega_{Ae}^2}{Q}\{(\zeta_R-\zeta_L)(\zeta_R+1)+2(1-\zeta_L\zeta_R)F^2\pm(\zeta_R+1)\sqrt{X}\} \end{aligned} \tag{4.43}$$

to simplify the left-hand side of (4.42):

$$\begin{aligned} 2i\gamma\omega_0[&F^2\{(L_0-E_0)(\rho_R-\rho_e)+(R_0-E_0)(\rho_L-\rho_e)\}-\{(L_0+E_0)(\rho_R+\rho_e)+(R_0+E_0)(\rho_L+\rho_e)\}] \\ &= \mp 4i\gamma\omega_0\rho_e^2\omega_{Ae}^2\sqrt{X}. \end{aligned} \tag{4.44}$$

For the right-hand side, I was not able to find a simple factorization as is possible for the left-hand side. Substituting for $L_0, R_0$ and $E_0$ but leaving the terms with $\omega^2$, it is possible

to obtain the following formula for the damping decrement:

$$\frac{\gamma_\pm}{\omega_0} = \frac{\pi\rho_e(\omega_0^2-\omega_{Ae}^2)}{\pm 4\omega_0^2\omega_{Ae}^2\rho_A|\Delta_L||\Delta_R|\sqrt{(\zeta_L-\zeta_R)^2+4(\zeta_L-1)(\zeta_R-1)F^2}}$$

$$\times\{(1+F^2)\zeta_L\zeta_R(\omega_0^2-\omega_{AR}^2)(\omega_0^2-\omega_{AL}^2)(|\Delta_L|+|\Delta_R|)$$

$$+(1-F^2)(\omega_0^2-\omega_{Ae}^2)[|\Delta_L|\zeta_R(\omega_0^2-\omega_{AR}^2)+|\Delta_R|\zeta_L(\omega_0^2-\omega_{AL}^2)]\}. \tag{4.45}$$

An alternative way to write this equation is as follows:

$$\frac{\gamma_\pm}{\omega_0} = \frac{-\pi(\omega_0^2-\omega_{\mathrm{Ae}}^2)}{4\omega_0^2\rho_e\omega_{\mathrm{Ae}}^2\rho_A\sqrt{(\zeta_L-\zeta_R)^2+4(\zeta_L-1)(\zeta_R-1)F^2}}$$

$$\times\Big(\frac{\rho_R(\omega_0^2-\omega_{\mathrm{AR}}^2)[(1+F^2)\rho_L(\omega_0^2-\omega_{\mathrm{AL}}^2)+(1-F^2)\rho_e(\omega_0^2-\omega_{\mathrm{Ae}}^2)]}{|\Delta_R|}$$

$$+\frac{\rho_L(\omega_0^2-\omega_{\mathrm{AL}}^2)[(1+F^2)\rho_R(\omega_0^2-\omega_{\mathrm{AR}}^2)+(1-F^2)\rho_e(\omega_0^2-\omega_{\mathrm{Ae}}^2)]}{|\Delta_L|}\Big) \tag{4.46}$$

This expression is suited to check the case of anomalous systems. Formally, the equations for an anomalous system (in which we take, as usual, $\rho_L < \rho_R$) can be obtained from the equations of a standard system by letting $|\Delta_L| \to \infty$. For future reference, we will write down the equation for damping in anomalous systems, which is obtained simply by dropping the final term of the second factor in (4.46):

$$\frac{\gamma_{\pm,\mathrm{anom}}}{\omega_0} = \frac{-\pi(\omega_0^2-\omega_{\mathrm{Ae}}^2)}{4\omega_0^2\rho_e\omega_{\mathrm{Ae}}^2\rho_A\sqrt{(\zeta_L-\zeta_R)^2+4(\zeta_L-1)(\zeta_R-1)F^2}}$$

$$\times\frac{\rho_R(\omega_0^2-\omega_{\mathrm{AR}}^2)[(1+F^2)\rho_L(\omega_0^2-\omega_{\mathrm{AL}}^2)+(1-F^2)\rho_e(\omega_0^2-\omega_{\mathrm{Ae}}^2)]}{|\Delta_R|}. \tag{4.47}$$

**The case of two identical tubes**

As an analytical check we can investigate what happens if we suppose the tubes are identical. Such systems exhibit the standard behavior independent of the separation between the loops. When $R_0 = L_0$, the two terms on the right-hand side of (4.42) are identical. The factor $\sqrt{X}$ in the left-hand side of (4.42) can also be rewritten, which leads to

$$\mp 8i\gamma\omega_0\rho_e^2\omega_{Ae}^2(\zeta-1)F = -2L_0E_0I_L\{(L_0+E_0)+F^2(L_0-E_0)\}. \tag{4.48}$$

Since in this case $\omega_0^2 = \frac{2\omega_{Ae}^2}{\zeta+1\mp(\zeta-1)F}$, equations (4.43) simplify to

$$\begin{aligned} L_0 + E_0 &= \frac{\pm 2(\rho_L - \rho_e)F\omega_{Ae}^2}{\zeta + 1 \mp (\zeta-1)F} \\ L_0 - E_0 &= \frac{\pm 2(\rho_L - \rho_e)\omega_{Ae}^2}{\zeta + 1 \mp (\zeta-1)F} \\ L_0 E_0 &= \frac{\omega_{Ae}^4 \rho_e^2 (\zeta-1)^2(F^2-1)}{(\zeta + 1 \mp (\zeta-1)F)^2}. \end{aligned} \tag{4.49}$$

Substituting (4.49) into (4.48) we obtain for the damping decrement

$$\gamma_\pm = \frac{-\pi\omega_{Ae}^4 \rho_e (\zeta-1)^2(1-F^2)(1\pm F)}{2\omega_0 \rho_A |\Delta| (\zeta + 1 \mp (\zeta-1)F)^3}. \tag{4.50}$$

This equation is identical to equation (82) of Robertson & Ruderman, 2011 [31] (The minus sign is because these authors write $\omega \approx \omega_0 - i\gamma$ instead of $\omega \approx \omega_0 + i\gamma$).

## 4.4 Parametric study of damping decrement

To understand the damping properties of the two-loop system, we will investigate the dependence of equations (4.45) and (4.47) on the different loop densities and the distance between the tubes. Since the parameter space is a priori quite large, we will have to make some simplifications. We will suppose that both loops have the same radius. We have shown in equation (3.16) that in the long-wavelength regime, the undamped frequencies are independent of the tube radius. For analytical simplicity, we will suppose that the density drops linearly in the inhomogeneous layer, so that density profile (4.35) can be used. This means that equation (4.36) can be used to determine the gradient of the Alfvén frequency in the resonant position. The term $\rho_A$ can be rewritten using equation (4.27).

To perform a parametric study, it is customary to normalize the different variables appearing in equations (4.45) and (4.47). In this case, all length scales will be represented as fractions of the loop length $L$, and the density will be normalized with respect to the density of the exterior plasma, i.e. $\zeta = \rho/\rho_e$. As a consequence, all frequencies will be normalized with respect to the Alfvén speed of the exterior medium, $\omega \to \omega/\omega_{\mathrm{Ae}}$.

An important variable is the thickness of the inhomogeneous layer, since this will play an important role in determining the gradient $|\Delta|$ of the Alfvén frequency. We want the thin boundary assumption to be valid throughout the entire parameter space. We know, however, that the tube radius and the shape of the inhomogeneous layer depend strongly on the value of $\tau_L = \tau_R = \tau_0$. The easiest way out of this problem is to fix the average relative thickness of the nonuniform layer (defined in (4.38) to $l_{\mathrm{avg,L}}/R = 0.01$. This also ensures that the expressions for the damping decrement become independent of the radius itself, which eliminates $R$ from the parameter space. However, this averaging over $\tau$, ignoring the geometry of the problem, has some side effects as well; we will deal with them further in this subsection.

First, we will investigate the dependence of the damping on the distance between the two loops. From (3.2) we know that $d/R = 2\cosh\tau_0$. We will investigate two cases.

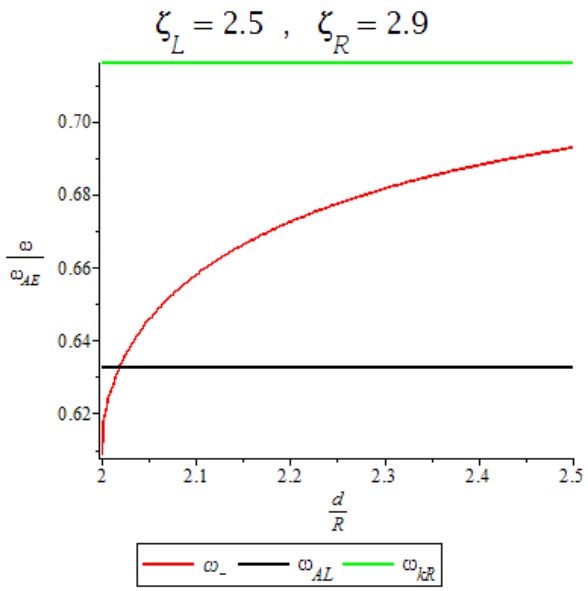


Figure 4.4: Plot of the lower eigenfrequency $\omega_-$ as a function of tube separation $d/R$, together with the Alfvén frequency of the left tube, marking the transition point between standard and anomalous systems, and the kink frequency of the right tube.

In the first case, the loop densities are equal: $\zeta_L = \zeta_R = 3$. This means we can use the 'standard' expression (4.45) for the damping decrement everywhere. In the second case, we set $\zeta_L = 2.5, \zeta_R = 2.9$. As Figure (4.4) shows, only for very small distances ($d/R \lesssim 2.05$) we will have to use the 'anomalous' expression (4.47) to determine $\gamma_-$. A small calculation verifies that in the limit $\omega_- \to \omega_{\mathrm{AL}}$ both the 'standard' and 'anomalous' expression for the damping decrement (4.45) and (4.47) converge to the same value, such that $\gamma_-$ is a continuous function of both density and distance at these positions.

Figure (4.5) shows how the damping depends on the distance between the tubes. The damping of the kink frequencies of the individual flux tubes are plotted as well, and have been taken from equation (32) of Goossens et al. (2009) [15]. They can also be recovered by imposing a linear density profile in our equation (2.40). Quite some information can be read off from this Figure. We can note first of all that the sign of $\gamma$ is negative for both frequencies, confirming again that the resonant layer corresponds to a damping of the two-loop eigenfrequencies. The magnitude of the damping is rather small, indicating large damping times. This is analogous to what happened in Chapter 2, since the expression for the damping decrement is proportional to $l_{\mathrm{avg}}/R \ll 1$. One can again put coronal seismology in action to compare these predicted damping times with the observed damping times to conclude that in coronal conditions, the nonuniform layers ought to be quite large.

Now let us discuss the more interesting aspects of Figure (4.5). In the limit $d/R \to \infty$, the damping decrement tends to the damping decrements of the kink frequencies of the individual loops. This is not surprising. When the loops are placed far from each other, the system of two loops becomes decoupled as shown in equation (4.30). Moreover, in the limit $d/R \to \infty$, we have seen in Chapter 3 (specifically equation (3.17)) that the homogeneous two-loop frequencies tend to the kink eigenfrequencies of the loops. Since $\zeta_L < \zeta_R$, we have $\omega_+ \to \omega_{\mathrm{kL}}$ and $\omega_- \to \omega_{\mathrm{kR}}$. Let us focus on $\omega_+$ and its damping

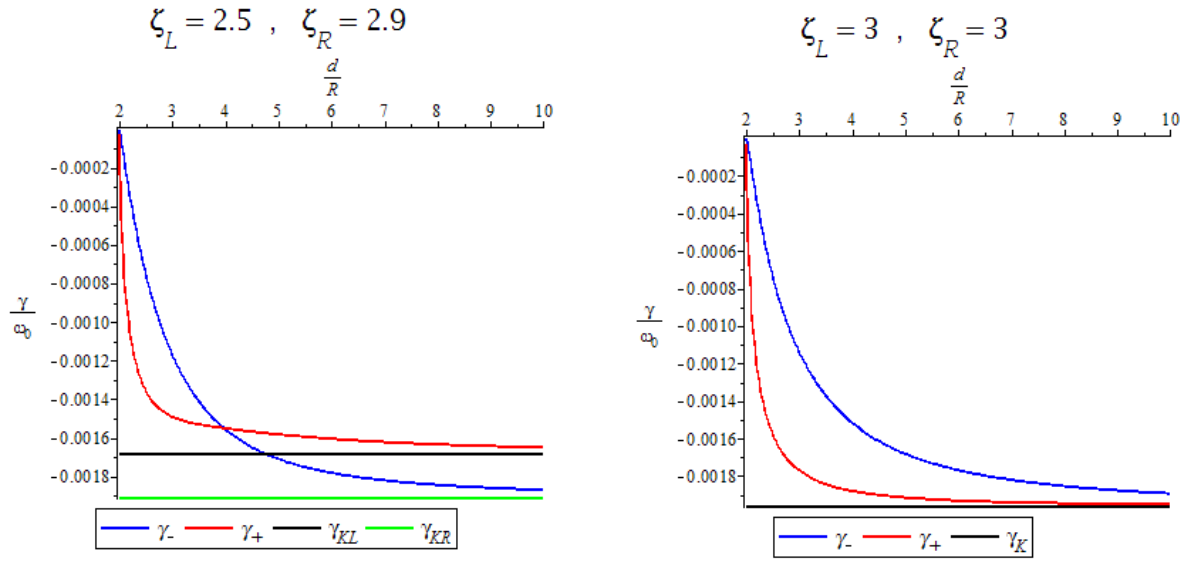


Figure 4.5: Dependence of the damping decrement on the separation between the loops. Left: unequal loop densities $\zeta_L = 2.5, \zeta_R = 2.9$. Right: equal loop densities $\zeta_L = \zeta_R = 3$. Also the damping rates for the kink frequencies of the individual loops are shown.

decrement. It can be shown analytically that the contribution of the damping in the right loop on the global motion vanishes in the limit of large loop separations; just take the limit $\omega_+ \to \omega_{\mathrm{kL}}$ in equation (4.46) and it is easily seen that the factor between square brackets in the term containing $|\Delta_R|$ becomes zero. When the loops are identical, both frequencies will tend to the common kink frequency of the loops.

When the separation between the loops becomes smaller, they interact more strongly as the collective homogeneous eigenfrequencies differ more from the individual kink frequencies, as can be seen for the lower eigenfrequency in Figure (4.4). This coupling of the loops persists until the system becomes anomalous and the lower density loop cannot follow the global oscillations of the two-loop system anymore. Interesting to note from Figure (4.5) is that the interaction between the loops decreases the efficiency of resonant damping. This was already noted in the article of Robertson & Ruderman (2011) [31]. However, research in the absorption of acoustic waves by sunspots suggest that a collection of loops is a more efficient absorber of incident wave energy than an individual sunspot (Keppens et al. (1994) [19]). We look only at the eigenvalue problem here, while they consider the initial value problem. Nevertheless, in the light of these results the reduced efficiency of resonant absorption for interacting loops can be considered rather surprising. It should not be completely ruled out that this tendency is due to the geometry inherent of the bicylindrical coordinate system. The results of Section 5 could shed more light on this.

When $d/R = 2$, the loops touch each other and fill the entire half-plane. Figure (4.5) shows that the oscillations of the two loops will not be damped anymore in this limit. However, this result might be inaccurate. In fact, the limit $\tau_0 \to 0$ is quite a peculiar one. For equal tube densities, this will eventually lead to a state in which almost entire volume of $3d$-space is filled with a plasma of equal density. When the radii are very large, one could approximate the system of two loops with as a single elliptic structure with the

two loops glued to one another, oscillating with the $S_x$ and $S_y$ eigenmodes. The other two eigenmodes will become unphysical, as this would imply that the loops penetrate one another (Van Doorsselaere et al. (2008) [39]). In the case of two loops with unequal densities, the limit $\tau_0 \to 0$ will lead to an anomalous system in which only the denser loop oscillates. In this case, the density of the immobile less dense loop could contribute as a boundary condition of the oscillations of the denser loop.

In these unusual geometrical situations the expressions derived in this Chapter probably lose their validity. However, we can still deduce where the limit $\gamma_\pm \to 0$ for $\tau_0 \to 0$ comes from in the expressions (4.46) and (4.47) for the damping decrement. Let us therefore look at expressions (4.46) and (4.47) in the limit of $\tau_0 \to 0$. In this limit, the system is always anomalous except when the two tubes have equal densities, in which case (4.46) is equivalent to (4.50). For the zero-order solutions, derived in Chapter 3 (equation 3.16), we find that in the limit of $\tau_0 \to 0$, which is equivalent with $F \to 1$, that

$$\omega_\pm^2 \to \frac{\omega_{\rm Ae}^2[\zeta_L+\zeta_R+2 \pm \sqrt{(\zeta_L+\zeta_R)^2+4(\zeta_L-1)(\zeta_R-1)}}{(\zeta_L+1)(\zeta_R+1)-(\zeta_L-1)(\zeta_R-1)} = \omega_{\rm Ae}^2\,\frac{\zeta_L+\zeta_R+2 \pm (\zeta_L+\zeta_R-2)}{2(\zeta_L+\zeta_R)}. \tag{4.51}$$

This leads in particular to

$$\omega_+^2 \to \omega_{\rm Ae}^2, \qquad \omega_-^2 \to \frac{2\omega_{\rm Ae}^2}{\zeta_L+\zeta_R}. \tag{4.52}$$

The limiting frequency for $\omega_-$ is equal to the kink frequency of a tube with density $\rho_L+\rho_R-\rho_e$, but this might be incidental since in this limit both loops fill an entire half-plane so there is no more exterior plasma. The convergence of $\omega_+$ to the Alfvén frequency of the exterior plasma indicates that the factor $\omega_+^2-\omega_{\rm Ae}^2$ appearing in both (4.46) and (4.47) will become zero when $\tau_0 \to 0$. It also means that the geometrical factor $1 \pm F$ appearing in (4.50) should be identified with $(\omega_\pm^2\omega_{\rm Ae}^2)$ in expression (4.46).

When the two loops have equal densities, from equation (4.52) follows that $\omega_-^2 \to \omega_{\rm Ai}^2$ with $\omega_{\rm Ai}^2$ the interior Alfvén speed of both loops. In the case of two identical loops, one can see from the second factor in equation (4.46) that because $(1-F^2)=0$ a factor $(\omega_0^2-\omega_{\rm AL}^2)(\omega_0^2-\omega_{\rm Ae}^2)$ can be factored out, which is then also zero because of (4.52). These factors correspond with the term $(1-F^2)$ appearing in (4.50). In conclusion, this factor appears solely because of the fact that both tubes are identical.

These mathematical points now lead us to what is probably the essence of the matter. When the two tubes have different densities (so that we have to use the 'anomalous' expression (4.47)) we still need an explanation of why $\gamma_- \to 0$ when $\tau_0 \to 0$ (which is equivalent to $d/R \to 2$) in Figure (4.5). This can only be because of the factor $1/|\Delta_R|$ appearing there. Hence a physical explanation for this limit (in all cases) should be concerned with this factor.

Recall from Section 4.1 that $|\Delta| = \frac{d\omega_A^2}{d\tau}_{(\tau=\tau_{AL,R})}$ is actually a quantity linked to the bicylindrical coordinate system, not in particular to the thickness of the inhomogeneous layer itself. Now if we use the linear density profile (which we employed to plot the figures in this section) and keep the average thickness of the inhomogeneous layer constant, then

equations (4.36) and (4.39) yield that

$$\frac{1}{|\Delta_{L,R}|} \sim l = \frac{l_{\text{avg,(L,R)}}}{R} \tanh \tau_{L,R}.$$

This means that indeed $1/|\Delta_{L,R}| \to 0$ as $\tau_{L,R} \to 0$. Normally, the limit $|\Delta_{L,R}| \to \infty$ brings to mind the limit one takes when making the inhomogeneous layer infinitely thin. In this case, the limit $|\Delta_{L,R}| \to \infty$ should be explained by the coordinate system used (because we have fixed $\frac{l_{\text{avg,(L,R)}}}{R} = 0.01$). When $\tau_{L,R} \to 0$, in order to keep the thickness of the inhomogeneous layer finite we must also take the limit $l \to 0$. But then this means that the derivative of the Alfvén frequency with respect to the bicylindrical coordinate $\tau$ — not with respect to any physical direction — must diverge to infinity. It means that we cannot really investigate in this coordinate system what happens when two cylinders are brought close together but do not become infinitely large. The resulting system then looks much like an elliptic structure, such as the one investigated by Ruderman in 2003 [33]. It would be interesting to investigate this limiting case further.

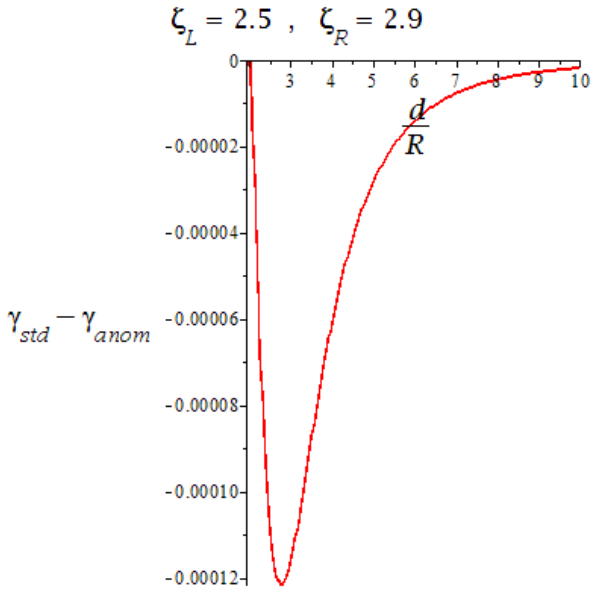


Figure 4.6: Difference between the damping decrement in standard systems with the equivalent expression for anomalous systems, of which one is unphysical, for loop densities $\zeta_L = 2.5, \zeta_R = 2.9$.

One can wonder whether the distinction between standard and anomalous systems significantly influences the damping decrement or not. Figure (4.6) shows the difference $\gamma_{-,\text{std}} - \gamma_{-,\text{anom}}$ for the investigated loop distances. Determining the relative difference between the two damping expressions using Figures (4.5) and (4.6) (look at the scales in both Figures), we conclude that the results are the same whether we use the standard or anomalous values of the damping decrement. The physical reason for this is the following. We have seen in Section 3.3. that in anomalous regimes, the less dense loop cannot support the global oscillations of the system anymore. Hence, the contribution of the damping in this loop becomes negligible in anomalous systems.

Now, we will investigate the influence of the different tube densities on the damping decrement. We set $d/R = 3$ which is a realistic distance between the loops going by

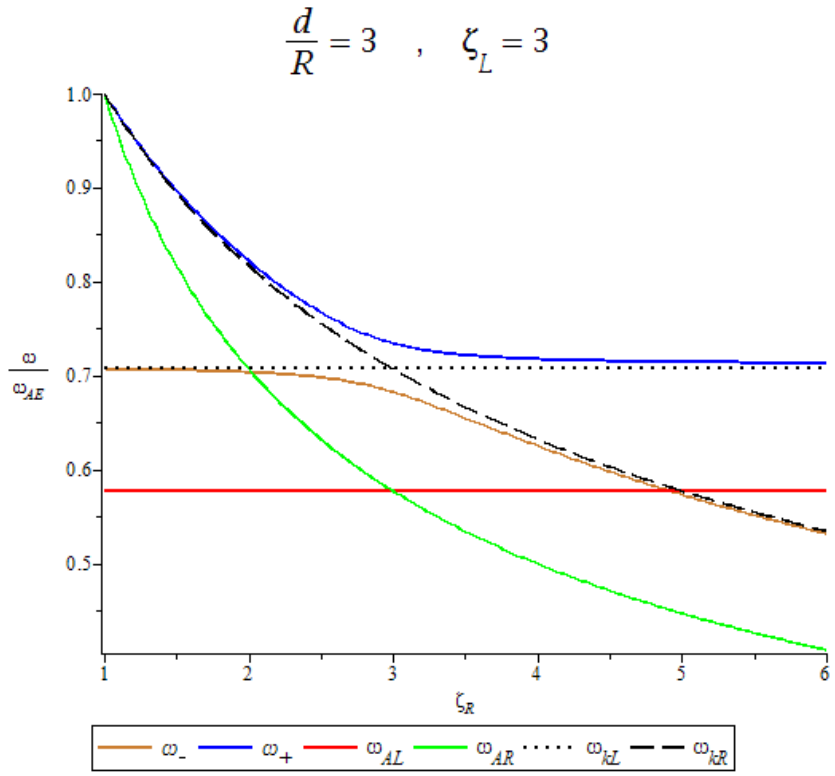


Figure 4.7: Plot of the eigenfrequencies $\omega_-$ and $\omega_+$ as a function of the density in the right tube $\zeta_R$ for fixed $\zeta_L$ and $d/R$, together with the Alfvén frequencies of the left and right tubes, marking two transition points between standard and anomalous systems, and the individual kink frequencies of the two tubes.

observations (Aschwanden et al., 2003 [4]). We fix the density of the left loop $\zeta_L = 3$ and let $\zeta_R$ vary between 1 and 6. This means that both loops can be the less dense one, and that an anomalous system emerges at both ends of the density range $\zeta_R$. This is illustrated in Figure (4.7). For small values of $\zeta_R$, the right loop cannot support the global oscillations while for large values of $\zeta_R$, the left loop will be unable to support them. It can be shown that here as well, the contributions of the anomalous regime is negligible because of the fact that only one loop is oscillating. When the loop densities are equal, the interaction between the tubes is maximal in the sense that the frequencies $\omega_+$ and $\omega_-$ differ most from the individual kink frequencies as Figure (4.7) shows.

Figure (4.8) shows the dependence of the damping decrement on the density contrast between the two loops when the distance between them is kept fixed. The 'standard' and 'anomalous' expressions (4.45) and (4.47) are used where they are appropriate. We note from Figure (4.8) that in the case that the loop densities are equal, the higher eigenfrequency is most strongly damped when compared to unequal loop densities, while the lower eigenfrequency gets least damped in this case. The physical explanation of this should probably be looked for in the nature of the eigenfunctions. The higher frequency $\omega_+$ is the frequency of the $S_y$ and $A_x$ eigenmodes. As explained in Chapter 3 (see Figure (3.2)), for the $A_x$- and $S_y$-mode the motions are such that the plasma surrounding the flux tube moves in the direction opposing the movement of the other tube. It explains why its frequency is higher. This eigenmode will then also be susceptible to a stronger

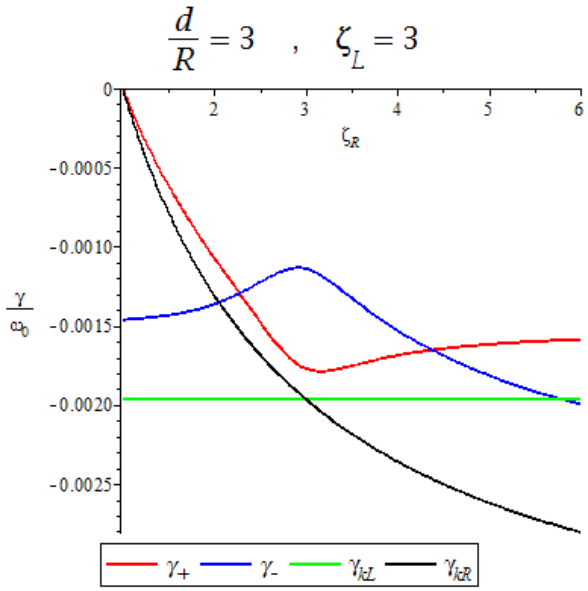


Figure 4.8: Dependence of the damping decrement on the density contrast between the two loops for a fixed loop distance.

damping. The collective oscillations can be more strongly damped than the individual oscillations (manifested when the density contrast is large) which feel less resistance from the intermediate fluid. On the other hand, the $S_x$- and $A_y$- eigenmodes are supported by the intermediate fluid motions, which explains their lower frequencies (longer periods) and can also explain why these modes are less efficiently damped than the individual kink modes.

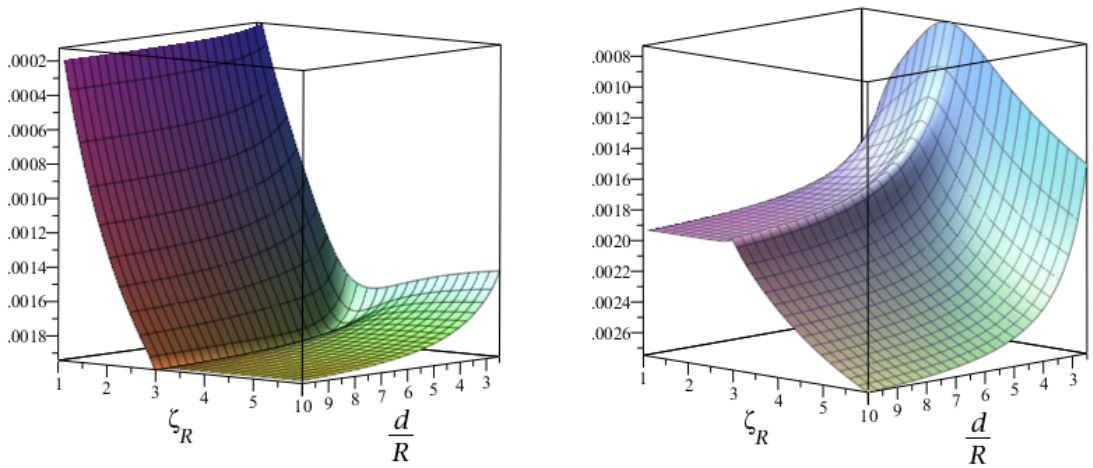


Figure 4.9: Surface plots showing the dependence of the damping decrement on the density contrast and the loop separation. Left: the damping $\gamma_+$ of the higher frequency. Right: the damping $\gamma_-$ of the lower eigenfrequency.

When the density of the right tube decreases to the density of the exterior fluid, the eigenfrequency $\omega_+$ tends to the Alfvén frequency of the exterior fluid (Figure 4.7), since it is the highest frequency present in the system. Since in this limiting case there only remains one loop, it is logical that the damping decrement $\gamma_+$ converges to zero (Figure 4.8). Interestingly, $\gamma_-$ does not converge to the damping of the kink frequency for the left tube when $\zeta_R \to 1$. This is because of the factor $\tanh(\tau_0)$ which we introduce in the equations when keeping $l_{\text{avg}}/R$ constant, because of the formula (4.39) which expresses $l_{\text{avg}}/R$ in terms of the parameters of the study. It can be calculated that in the limit of $\zeta_R \to 1$, we have indeed $\gamma_- \to \gamma_{\text{kL}} \tanh \tau_0 = \gamma_{\text{kL}} \tanh(\text{arccosh}(d/2R))$.

Finally, Figure (4.9) combines and in a way summarizes the results of the previous paragraphs. It plots the dependence of both damping decrements on the tube distance and the density contrast. The range of loop distances has been limited to $d/R \in [2.5, 10]$ to avoid the systems in which the expressions obtained in Section 4.3. do not longer correspond with thin cylinders. Especially for the damping of $\gamma_-$ (right panel) we can see that the interaction between the tubes reduces the efficiency of resonant damping.

# Chapter 5

# Oscillations of systems of parallel magnetic loops: T-matrix method

In Chapters 3 and 4, we looked at oscillations of a system of two magnetic loops using separation of variables in a bicylindrical coordinate system. There is no obvious way to generalise these results to systems of more than two coronal loops. Furthermore, we encountered in Sections 4.3 and 4.4 some of the peculiarities of the bicylindrical coordinate system, especially in the limiting cases $\tau \to 0$ or $\tau \to \infty$.

Therefore, we will investigate another method to solve the MHD equations for a system of more than two coronal loops. Consider an ensemble of $N$ pressureless magnetic loops. The $j^{\text{th}}$ loop is centered (in a cylindrical coordinate system) at $\mathbf{r} = \mathbf{r_j}$, its radius is $a_j$, its density is $\rho_j$ and its Alfvén frequency is $\omega_{\text{Aj}}$. The density and Alfvén frequency of the exterior fluid will be denoted by $\rho_0$ and $\omega_{\text{A0}}$ respectively. Then the total pressure perturbation $P' = \frac{B_0 B_z}{\mu}$ satisfies the wave equation:

$$\frac{\partial^2 P'}{\partial t^2} - v_{\text{A}}^2 \nabla^2 P' = 0. \tag{5.1}$$

If we Fourier-analyse in $z$ and $t$, then we can write $P' = \exp(kz - \omega t)\psi(r, \phi)$. (In Chapter 3, we slightly abused notation and wrote $P'$ for $\psi$ as well. The notation $\psi$ has been chosen here to connect with the results of acoustic and electrodynamic physics.) We have already seen in Section 3.2., equation (3.7) that this leads to the scalar Helmholtz equation for $\psi$:

$$\nabla_\perp^2 \psi + k_\perp^2 \psi = 0. \tag{5.2}$$

where

$$k_\perp = (\omega^2 - \omega_{\text{A}}^2)/v_{\text{A}}^2 \tag{5.3}$$

depends on the density of the cylinders or the exterior fluid.

We can look at the magnetised cylinders as a collection of scatterers. This view is motivated by the rich history of the scattering problem in electrodynamics (the famous Rayleigh scattering of electromagnetic waves) and acoustics. We single these two disciplines out, even though in many other fields of physics, scattering problems are studied. The reason is that in these two disciplines the governing equation describing the wave

motion is the classical wave equation, as it is here. (For example, in quantum mechanics, the governing partial differential equation is the Schrödinger equation.)

The T-matrix method has been developed in acoustic physics by Waterman (1969) [41] to provide a computationally efficient alternative for solving the scalar Helmholtz equation under von Neumann or Dirichlet boundary conditions. In essence, one relates the exciting and scattered fields through a linear operator $T$ on the infinite-dimensional Hilbert space $L^2(\Gamma)$, the space of square-integrable functions on the boundary of the obstacle (which in our case corresponds to the union of the cylinder surfaces). The T-matrix method consists of truncating the infinite system of equations which connects the exciting and scattered fields to obtain a linear system of equations. The convergence of this method has been studied by Ramm [30], who gave mathematical conditions under which the T-matrix method converges.

Unfortunately, we will not deal with the mathematical intricacies of the T-matrix method, described by Ramm [30], because of the following reason. The boundary conditions to equation (5.2) are given by continuity of total pressure and radial displacement, as before. In this case, both the value of $\psi$ and its normal derivative are prescribed on the boundary — however, they are only given in terms of the (unknown) solutions at the inside and outside region. Instead, we will follow another approach which has been introduced in a series of papers by Bogdan and different coauthors (1985, 1989, 1991) [5] [6] [7]. They were the first to apply the results of the acoustic theory to study the interaction of sunspots with acoustic waves. This was studied to resolve the (then) controversy whether sunspots are monolithic or multi-stranded (the so-called 'spaghetti sunspot' model (Parker, 1979 [28])) in nature. Luna et al. (2009, 2010) [22] [23] adapted their methods to investigate oscillations of coronal loops. They present numerical solutions for different numbers of interacting coronal loops. However, they do not investigate whether analytical solutions can be recovered in the long-wavelength limit. Perhaps more importantly, the effects of resonant absorption on the oscillations of a multi-loop system have not been addressed so far to the best of my knowledge.

In Section 5.1., I will give a simple example illustrating the main principles and mathematics behind the T-matrix framework in the formulation of Bogdan, and introduce some terminology. This will be just a more elaborate version of the 'pedagogical example' in the paper of Bogdan & Fox (1991) [7], so those familiar with that can skip to Section 5.2. There I derive the equations for the system of coronal loops (following Luna et al. (2009) [22]) and present some of my findings. Due to time restrictions in the planning of the master thesis, I will only be able to present a few partial results of my investigations here. Further research is still needed, and will also be done during the summer.

## 5.1 T-matrix method and principles of multiple scattering

To introduce the T-matrix method and some mathematical methods in scattering theory, consider the problem of the scattering of an acoustic plane wave by a pair of cylinders. The cylinders are elastic, i.e. there is no transfer of momentum between the waves and

the cylinder. We suppose that the wave vector lies in the plane perpendicular to the cylinder axes, with which we align the coordinate system such that the axes are parallel to the $z$ coordinate axis. When the cylinders have no acoustic properties, the inclusion of a $z$-coordinate of the wave vector would just result in a factor $\exp(ik_z t)$ in all equations. The equilibrium configuration is then shown in Figure (5.1).

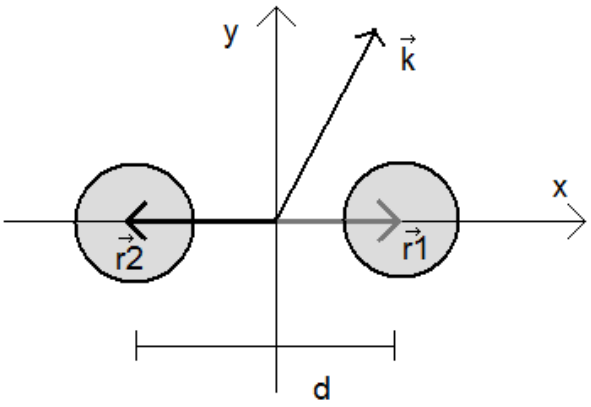


Figure 5.1: Equilibrium configuration for the multiple scattering problem considered in Section 5.1.

Consider an incoming plane wave of the form

$$\phi(\mathbf{r},t) = e^{\frac{i\mathbf{k}\cdot(\mathbf{r_1}-\mathbf{r_2})}{2}} e^{i(\mathbf{k}\cdot\mathbf{r}-\omega t)}. \tag{5.4}$$

In this equation, the phase shift $\exp(\frac{i\mathbf{k}\cdot(\mathbf{r_1}-\mathbf{r_2})}{2}) = \exp(ikd\cos\chi/2)$ (with $d = |\mathbf{r_1}-\mathbf{r_2}|$) is added to obtain symmetry in the expressions, and the meaning of $k = |k|$ should be slightly altered in the case of acoustic physics: $|k| = \omega/v_{S0}$ in which $v_{S0}$ is the sound speed in the external medium. Finally, let us introduce the angle $\chi$ between the wave vector with $(\mathbf{r_1}-\mathbf{r_2})$, the angle $\varphi(\mathbf{r})$ between the position vector $\mathbf{r}$ and $\mathbf{k}$ and the angles $\varphi_j$ between the $x$-axis and the vector $\mathbf{r}-\mathbf{r_j}$ $(j \in \{1,2\})$.

We can use the Anger-Jacobi formula to write the incoming acoustic wave locally as a series of Bessel functions of the first kind:

$$e^{\frac{id\cos\chi}{2}}\, e^{i(k|\mathbf{r}|\cos\varphi-\omega t)} = e^{\frac{id\cos\chi}{2}} \sum_{m=-\infty}^{\infty} i^m J_m(k|\mathbf{r}|)\, e^{im\varphi}\, e^{-i\omega t}. \tag{5.5}$$

Because of the relation $J_{-m}(x) = (-1)^m J_m(x)$, it is also possible to combine the terms $i^{\pm m} J_{\pm m}(k|\mathbf{r}|)\, e^{i(\pm)m\varphi}$ and take the sum over the positive integers only. We also expand the excitation of the first cylinder in a local Fourier-Bessel series:

$$\psi^1_{\text{ex}} = \sum_{m=-\infty}^{\infty} B^1_m J_m(k|\mathbf{r}-\mathbf{r_1}|) e^{im\varphi_1}\, e^{-i\omega t}. \tag{5.6}$$

The scattering of the wave can be expressed by a linear operator $T$ which links the expansion coefficients of the exciting wave with those of the scattered wave. $T$ is called the $T$-matrix (for obvious reasons) and the method of connecting the expansions the

$T$-matrix method. Hence, the scattered wave can be expressed as follows:

$$\psi_{\text{sc}}^1 = \sum_{m=-\infty}^{\infty} \sum_{n=-\infty}^{\infty} -T_{mn}^1 B_n^1 H_m^{(1)}(k|\mathbf{r} - \mathbf{r_1}|) e^{im\varphi_1}\, e^{-i\omega t}. \tag{5.7}$$

We use an expansion in the form of Hankel functions of the first kind since we want a solution in the form of outward propagating waves. It can be shown that for axisymmetric obstacles such as cylinders, the $T$-matrix is diagonal (Bogdan & Zweibel, 1985 [5]). Furthermore, for identical cylinders the $T$-matrix is the same for both scatterers, such that we can rewrite (5.7) as

$$\psi_{\text{sc}}^1 = \sum_{m=-\infty}^{\infty} -T_{mm} B_m^1 H_m^{(1)}(k|\mathbf{r} - \mathbf{r_1}|) e^{im\varphi_1}\, e^{-i\omega t}. \tag{5.8}$$

We will now make the drastic assumption that the cylinders only scatter the axisymmetric component ($m = 0$) of the exciting waves to obtain simple analytical solutions. This assumption will be dropped in Section 5.2. In this case, the acoustic wave and the incoming and scattered waves can be written down as follows (also dividing by $e^{-i\omega t}$ in all equations):

$$\begin{aligned} \psi_{\text{ex}}^1 &= B_0^1 J_0(k|\mathbf{r} - \mathbf{r_1}|) & \psi_{\text{sc}}^1 &= -T_{00} B_0^1 H_0^{(1)}(k|\mathbf{r} - \mathbf{r_1}|) \\ \psi_{\text{ex}}^2 &= B_0^2 J_0(k|\mathbf{r} - \mathbf{r_2}|) & \psi_{\text{sc}}^2 &= -T_{00} B_0^2 H_0^{(1)}(k|\mathbf{r} - \mathbf{r_2}|) \\ \phi &= e^{\frac{id\cos\chi}{2}} J_0(k|\mathbf{r}|). \end{aligned} \tag{5.9}$$

The exciting wave in the second cylinder is the sum of the scattered wave by the first cylinder and the incoming acoustic wave, and analoguously in the first cylinder:

$$\psi_{\text{ex}}^2 = \psi_{\text{sc}}^1 + \phi, \qquad \psi_{\text{ex}}^1 = \psi_{\text{sc}}^2 + \phi. \tag{5.10}$$

To write the scattered waves and acoustic plane wave in the form of a local excitation of the second cylinder, we can use the translation formulae (Bogdan & Cattaneo, 1989 [6]):

$$Z_n(k|\mathbf{r} - \mathbf{r_j}|) e^{in\varphi_j} = \sum_{m=-\infty}^{\infty} \begin{cases} J_{n-m}(kd) e^{in\varphi_{ij}} Z_m(k|\mathbf{r} - \mathbf{r_i}|) e^{im\varphi_i}, & |\mathbf{r} - \mathbf{r_i}| > d \\ Z_{n-m}(kd) e^{in\varphi_{ij}} J_m(k|\mathbf{r} - \mathbf{r_i}|) e^{im\varphi_i}, & |\mathbf{r} - \mathbf{r_i}| < d. \end{cases} \tag{5.11}$$

Here $Z_k$ can represent either $J_k, H_k^{(1)}$ [or $H_k^{(2)}$] and $\varphi_{ij}$ is the angle that the center of the $i^{\text{th}}$ loop makes with the center of the $j$-th loop (measured from the origin). If we only consider axisymmetric scattering, the translation formulae simplify to $Z_0(k|\mathbf{r} - \mathbf{r_j}|) = Z_0(kd) J_0(k|\mathbf{r} - \mathbf{r_i}|)$ where for our purposes $i, j \in \{1, 2\}$. Using the translation formulae together with equations (5.9) and (5.10) gives us a linear system of equations for $B_0^1$ and $B_0^2$:

$$\begin{aligned} B_0^1 + T_{00} B_0^2 H_0^{(1)}(kd) &= \exp(-\frac{ikd\cos\chi}{2}) \\ B_0^2 + T_{00} B_0^1 H_0^{(1)}(kd) &= \exp(\frac{ikd\cos\chi}{2}). \end{aligned} \tag{5.12}$$

The terms on the right give the contribution of the incoming acoustic plane wave. We can use Cramer's rule to quickly obtain solutions for $B_0^1$ and $B_0^2$ in terms of the scattering (in this case one-dimensional) matrix $T_{00}$:

$$B_0^1 = \frac{x \exp\left(-\frac{ikd\cos\chi}{2}\right) - \exp\left(\frac{ikd\cos\chi}{2}\right)}{(x-1)(x+1)}$$

$$B_0^2 = \frac{x \exp\left(\frac{ikd\cos\chi}{2}\right) - \exp\left(-\frac{ikd\cos\chi}{2}\right)}{(x-1)(x+1)}. \tag{5.13}$$

Here the abbreviation $x = T_{00}H_0^{(1)}(kd)$ has been used. The components of $T$ depend only on the scattering properties of the cylinder itself, and can be computed independently of equation (5.10) linking the scattered and exciting waves to one another. In this case, $T_{00}$ is completely determined by the scattering angle $\delta$ of the waves:

$$T_{00} = \frac{1}{2}(1 - e^{-i\delta}). \tag{5.14}$$

Since the scatterers are elastic, the only consequence of their presence is a phase shift between the incoming and outgoing wave, i.e. $\delta$ is real.

The scattering cross section $\sigma_s$ is defined as the scattered acoustic power per unit length divided by the energy flux of the incident plane wave (e.g. Keppens et al. (1994) [19]). In this example, it can be shown that the scattering cross-section can be written in terms of the $B_0^j$ as

$$\sigma_s = \frac{4}{k}|T_{00}|^2(|B_0^1|^2 + |B_0^2|^2 + J_0(kd)[\overline{B_0^1}B_0^2 + B_0^1\overline{B_0^2}] \tag{5.15}$$

(Bogdan & Fox, 1991 [7]). Some algebra reduces (5.15) to

$$\sigma_s = \frac{8}{k}|T_{00}|^2 \left( \frac{(1 + J_0(kd))\cos^2(kd\cos\chi/2)}{(x+1)^2} + \frac{(1 - J_0(kd))\sin^2(kd\cos\chi/2)}{(x-1)^2} \right). \tag{5.16}$$

Expression (5.16) helps to determine three different scattering regimes as explained by Bogdan & Fox (1991) [7]. As we will not use them further in the thesis, I will not elaborate further on this aspect. Nevertheless, the expressions of the scattering cross-section can be useful in later studies of the scattering theory of coronal loops; that is why it is still included here.

We can also calculate the eigenfrequencies of the system. If we remove the incoming acoustic wave from the analysis, the homogeneous counterpart of equation (5.12) yields an eigenvalue problem. Non-trivial solutions to (5.12) only exist if the determinant of the linear homogeneous system is zero. This yields the dispersion relation $(1 + x)(1 - x) = 0$ or

$$T_{00}H_0^{(1)}(kd) = \pm 1. \tag{5.17}$$

When $x = -1$, the system oscillates in phase with the eigenfrequency while antisymmetric oscillations correspond to an eigenfrequency yielding $x = 1$, as can be seen from the homogeneous counterpart to equation (5.12). To satisfy equation (5.17), the eigenfrequency $\omega$ should be complex. This means that acoustic driving cannot insonify the cylinders at one of their eigenfrequencies. However, when one of the eigenvalues $\omega_i$ of the system satisfies $\mathrm{Im}\,\omega_i \ll 1$, driving the system at the resonant frequency (determined through $\omega = \mathrm{Re}\,\omega_i$) will greatly enhance the scattering properties of the system.

## 5.2 Oscillations of a system of coronal loops using the T-matrix method

We will now apply the theory to study oscillations of a system of coronal loops using the T-matrix method. So consider again the configuration conceived at the beginning of the Chapter, and described by equation (5.2). For notational simplicity, the subscript '$\perp$' will be dropped in the remainder of this section, and the wave vectors $k_0$ and $k_j$ represent the perpendicular wave numbers (defined in (5.3)) in the outside plasma and the inside of the $j^{\text{th}}$ loop, respectively. We consider the eigenvalue problem and keep all the terms in the expansions of the incoming and outgoing waves. First we will consider the case without resonant absorption in an inhomogeneous layer at the $j^{\text{th}}$ loop. The equations of the previous section can be recycled without too many major changes. The reason is that equations (5.6) — (5.11) are independent of the scattering properties of the magnetic flux tubes themselves.

Expansions (5.6) and (5.8) are valid for each of the $N$ flux tubes. The consistency requirement (5.10) should be replaced by

$$\psi^j_{\text{ex}}(\mathbf{r}-\mathbf{r_j}) = \sum_{i\neq j}^{N} \psi^i_{\text{sc}}(\mathbf{r}-\mathbf{r_i}). \tag{5.18}$$

Then using equations (5.6), (5.8), (5.18) and the translation formulae (5.11), we obtain a linear system of equations for $B^j_m$ as follows (see also Luna et al., 2009 [22]):

$$B^j_m + \sum_{i\neq j}^{N}\sum_{n=-\infty}^{\infty} B^i_n T^i_{nn} H^{(1)}_{n-m}(k_0|\mathbf{r_i}-\mathbf{r_j}|)e^{i(n-m)\varphi_{ji}} = 0. \tag{5.19}$$

Finally, we will need that the total exterior field can be written as the sum of the incoming wave of the $j^{\text{th}}$ loop and the scattered wave of the $j^{\text{th}}$ loop. In terms of the expansions:

$$\psi_{\text{tot}}(\mathbf{r}-\mathbf{r_j}) = \sum_{m=-\infty}^{\infty} B^j_m[J_m(k_0|\mathbf{r}-\mathbf{r_j}|) + T^j_{mm}H^{(1)}_m(k_0|\mathbf{r}-\mathbf{r_j}|)]e^{im\varphi_j}. \tag{5.20}$$

The coefficients of the $T^j$-matrix are obtained by the boundary condition that the total pressure $\psi$ and the radial displacement $\xi_r$ are continuous across the boundary. If we also expand the internal field in the $j^{\text{th}}$ loop as

$$\psi^j_{\text{in}}(\mathbf{r}-\mathbf{r_j}) = \sum_{m=-\infty}^{\infty} c^j_m J_m(k_j|\mathbf{r}-\mathbf{r_j}|)e^{im\varphi_j}, \tag{5.21}$$

we can use the linearised momentum equation

$$\xi_r = \frac{1}{\rho(\omega^2 - v_{\text{A}}^2 k^2)}\frac{d\psi}{dr} \tag{5.22}$$

and (5.20), (5.21) to write the boundary conditions in terms of $\psi$ as

$$\psi^j_{\text{in}}(\mathbf{r}-\mathbf{r_j})\Big|_{|\mathbf{r}-\mathbf{r_j}|=a_j} = \psi_{\text{tot}}(\mathbf{r}-\mathbf{r_j})\Big|_{|\mathbf{r}-\mathbf{r_j}|=a_j}; \tag{5.23}$$

$$\begin{aligned}
\frac{1}{\rho_0(\omega^2 - v^2_{\text{A}0}k^2)}\,\frac{d\psi_{\text{tot}}}{d(\mathbf{r}-\mathbf{r_j})}\Big|_{|\mathbf{r}-\mathbf{r_j}|=a_j} &= \frac{1}{\rho_j(\omega^2 - v^2_{\text{A}j}k^2)}\,\frac{d\psi^j_{\text{in}}}{d(\mathbf{r}-\mathbf{r_j})}\Big|_{|\mathbf{r}-\mathbf{r_j}|=a_j}, \\
\Leftrightarrow \frac{1}{v^2_{\text{A}0}\rho_0 k_0^2}\,\frac{d\psi_{\text{tot}}}{d(\mathbf{r}-\mathbf{r_j})}\Big|_{|\mathbf{r}-\mathbf{r_j}|=a_j} &= \frac{1}{v^2_{\text{A}j}\rho_j k_j^2}\,\frac{d\psi^j_{\text{in}}}{d(\mathbf{r}-\mathbf{r_j})}\Big|_{|\mathbf{r}-\mathbf{r_j}|=a_j}, \\
\Leftrightarrow \frac{1}{k_0^2}\,\frac{d\psi_{\text{tot}}}{d(\mathbf{r}-\mathbf{r_j})}\Big|_{|\mathbf{r}-\mathbf{r_j}|=a_j} &= \frac{1}{k_j^2}\,\frac{d\psi^j_{\text{in}}}{d(\mathbf{r}-\mathbf{r_j})}\Big|_{|\mathbf{r}-\mathbf{r_j}|=a_j}.
\end{aligned} \tag{5.24}$$

If we use boundary conditions (5.23) and (5.24) for equations (5.20) and (5.21) and eliminate the expansion coefficients $c^j_m$ of the internal loop, we obtain after some calculation that

$$T^j_{mm} = \frac{k_j J_m(k_j a_j) J'_m(k_0 a_j) - k_0 J_m(k_0 a_j) J'_m(k_j a_j)}{k_0 H^{(1)}_m(k_0 a_j) J'_m(k_j a_j) - k_j H^{(1)'}_m(k_0 a_j) J_m(k_j a_j)}. \tag{5.25}$$

### 5.2.1 Solution for a system of $N$ loops

We have now reduced (5.19) to an infinite system of linear equations which only includes the variables $B^j_m$ as unknowns. In order to solve it, we need to truncate the system at a certain value of $m$, say $m_t$. This way, we obtain a sequence of eigenfrequencies $\{\omega^k_{m_t}\}$ which hopefully converges to the eigenspectrum of the two-loop system. In the calculations which follow, the eigenfrequencies which we are interested in eventually become independent of $m_t$.

If we truncate the system at $m_t = 0$, hence only consider axisymmetric components of the incoming and outgoing waves, and furthermore consider a system of just two loops, it can be readily seen that the linear system (5.19) reduces to

$$\begin{aligned}
B^1_0 + T^1_0 B^2_0 H^{(1)}_0(kd) &= 0 \\
B^2_0 + T^2_0 B^1_0 H^{(1)}_0(kd) &= 0
\end{aligned}$$

with the associated dispersion relation

$$1 + T^1_0 T^2_0 [H^{(1)}_0(kd)]^2 = 0 \tag{5.26}$$

which is identical to (5.17), with the exception that the T-matrices are now calculated by equation (5.25).

For higher values of $m_t$, equation (5.19) becomes essentially a homogeneous system of $N(2m_t - 1)$ equations for $N(2m_t - 1)$ unknowns. Non-trivial solutions only exist when the determinant of the matrix $M$ associated to this system is equal to zero. This leads to a dispersion relation which can be solved with a computer. Such a study has been performed by Luna et al. (2009, 2010) [22] [23] to investigate the oscillations of systems of coronal loops. Below, I briefly summarise their results for a system of 2, 3 and 10 loops of equal radius but different densities.

The results which Luna et al. (2009) [22] obtain for a system of two nonidentical loops with radii $a_1 = a_2 = 0.03L$ at a distance $d/R = 3$, employing the T-matrix method, agree qualitatively with the results we obtained in Chapters 3 and 4. Indeed, the long-wavelength assumption is applicable in this situation. Then the simplification of considering only equal loop radii can be justified a posteriori since in the long-wavelength approximation, the eigenfrequencies are independent of the radius. The $A_x, A_y, S_x$ and $S_y$ eigenmodes of Luna et al. (2008) [21] are recovered. The interaction between the tubes is measured with $\zeta_L = 3$ for $\zeta_R \in [1, 5]$ by measuring the deviation between the individual kink frequencies of the loops compared to the collective oscillation frequencies. The interaction between the loops is maximal when their densities are equal. This we found as well when discussing Figure (4.7). Luna et al. (2009) [22] claim that the system becomes decoupled when $\zeta_R \lesssim 2$ or $\zeta_R \gtrsim 4$. In the long-wavelength approximation, use of equation (3.23) shows that the upper threshold between standard and anomalous systems lies a bit higher at $\zeta_R \gtrsim 4.91$, as can also be seen from Figure (4.7) in Chapter 4. In general, the agreement between the T-matrix method and the results from previous Chapters suggests that the T-matrix method converges quickly.

Let us now consider a system of three aligned loops with equal radii $a_j = 0.03L$ and distance of adjacent loops $d/R = 3$ of which the relative densities of the left and middle loop are fixed at $\zeta_1 = 3$ and $\zeta_2 = 2$. In this situation, the first and second loop are decoupled in the long-wavelength approximation as inequality (3.24), with $\zeta_{1,L}$ and $\zeta_{2,R}$ reversed, is satisfied. In this case, Luna et al., 2009 [22] find six kinklike eigenmodes, of which the eigenfrequencies are plotted in the top panel of Figure (5.2). With kinklike modes, it is meant that at least one of the three loop axes is displaced due to transverse kinklike oscillations. Of course, many other fluting eigenmodes (associated with azimuthal wave numbers $m \geq 2$) are found; their number increases with increasing truncation number $m_t$. As can be seen from Figure (5.2), the eigenfrequencies are grouped in pairs of two almost identical frequencies, just like in the system of two coronal loops. When the density of the right loop differs from the densities of the two other loops, the global eigenfrequencies reduce to the individual kink frequencies of the loops.

This translates again in a coupling or decoupling of the different loops, as can be seen from the lower panel of Figure (5.2). In images (a), (d) and (g) we have $\zeta_3 = \zeta_2$. Observe that the middle and right loops oscillate in phase or antiphase, while the left loop oscillates independently. The same can be said for $\zeta_3 = \zeta_1$, shown in images (c), (f) and (i). Finally, when $\zeta_3 = 2.5$, it is found that the three loops oscillate independently. This shows that the presence of a third loop sharpens the requirements for collective loop oscillations, as for example without the presence of the first loop, equation (3.23) predicts the standard behaviour in the system consisting of only the middle and right loop.

When the three loop densities are equal, eight instead of six kinklike frequencies are found. Two of them correspond with a global kink oscillation of the three-loop system, either in the direction of the axis connecting the loop centers or perpendicular to it. Also mixed modes are found, in which the two outer loops oscillate kinklike and the middle loop responds with a flutelike oscillation. See Luna et al. (2009) [22] for more details.

Finally, let us briefly look at the results of the T-matrix method in a system of 10 coronal loops (Luna et al., 2010 [23]). The smaller coronal loops have radius $a_j = 0.006L$ and

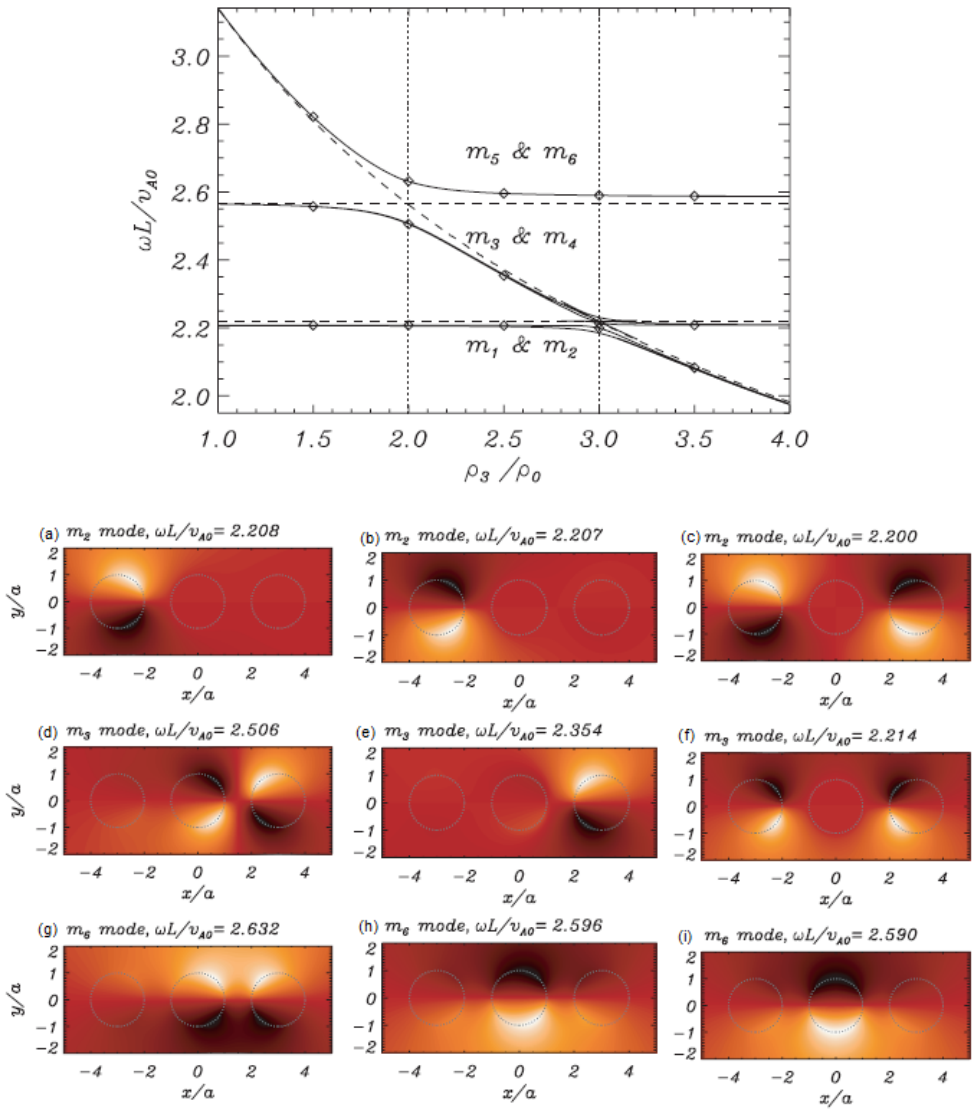


Figure 5.2: Eigenvalues (top panel) and eigenmodes (bottom panel) for three aligned magnetic flux tubes in which $\rho_1 = 3\rho_0$ and $\rho_2 = 2\rho_0$ are fixed as a function of $\rho_3/\rho_0$. In the top panel, the kink frequencies of the left, middle and right tube are given by respectively the lower horizontal, upper horizontal and diagonal dashed lines. The top, central and bottom images of the bottom panel show the $m_2$, $m_3$ and $m_6$ eigenmodes. In the images (a), (d) and (g) $\rho_3 = 2\rho_0$; in images (b), (e) and (h) $\rho_3 = 2.5\rho_0$ while in images (c), (f) and (i) $\rho_3 = 3\rho_0$. Adapted from Luna et al., 2009 [22].

are distributed randomly within a larger cylinder of radius $R = 5a_j$. The equilibrium configuration is shown in Figure (5.3). Our interest in studying this configuration is the following. It is debated whether coronal loops as we see them have an internal fine structure consisting of several mini-loops or 'strands' below the spatial resolution of the current telescopes (e.g. Klimchuk, 2006 [20]). Moreover, it has been demonstrated that the inference of the coronal magnetic field strength heavily depends on the chosen model (De Moortel & Pascoe, 2009 [9]).

In the configuration considered by Luna et al. (2010) [23], the densities of the strands are

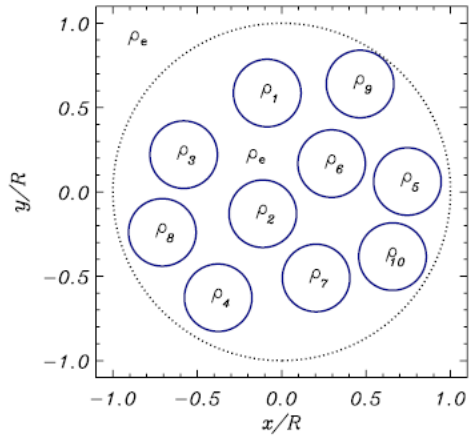


Figure 5.3: Equilibrium configuration in which ten subloops with different densities $\rho_j$ (see text) are distributed randomly within an potentially unresolved loop of radius $R = 0.03L$. The loops fill 40 % of the interior volume. From Luna et al. (2010) [23].

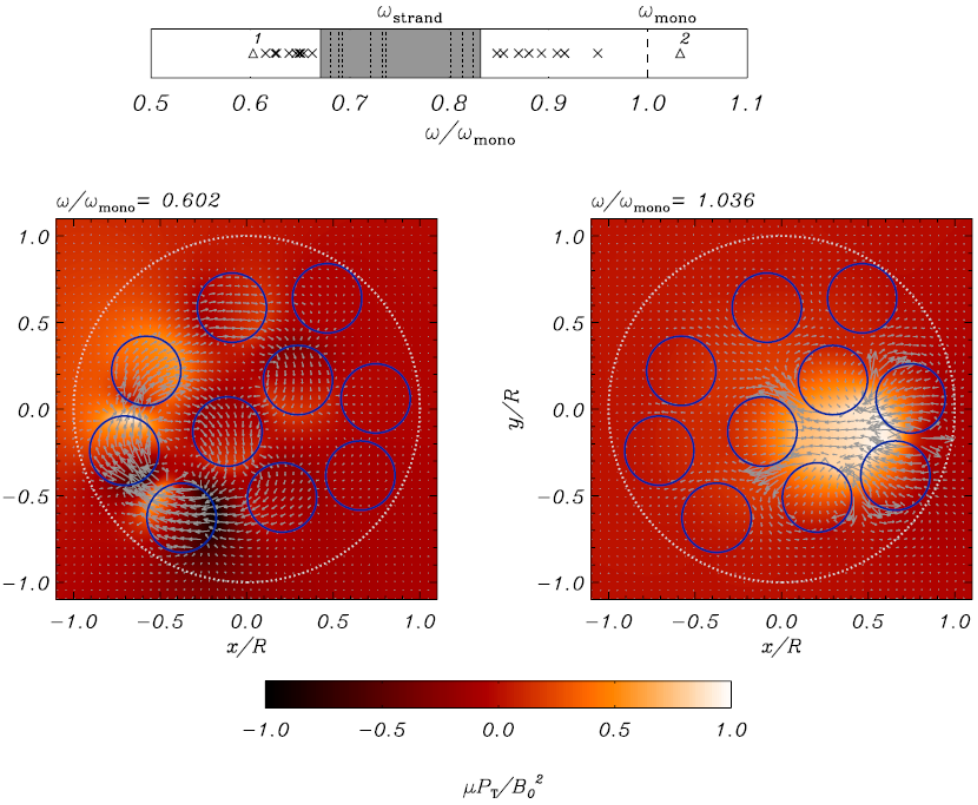


Figure 5.4: Eigenspectrum of the equilibrium configuration of Figure (5.3) (Top panel) and the eigenmodes corresponding to the lowest (left image) and highest (right image) eigenfrequency (Bottom panel). The dotted lines in the top panel represent the individal kink frequencies of the strands. From Luna et al. (2010) [23].

given by $\zeta_j = \{7.89, 7.61, 7.60, 8.97, 5.98, 8.73, 7.52, 8.62, 6.18, 5.80\}$. From Figure (5.3), it can hence be deduced that the three strands on the right have the lowest densities. An equivalent monolithic loop density is calculated by the model assmption that the 10

strands fill 40% of the volume of the loop; it works out to be $\zeta_{\text{eq}} = 3.6$.

Figure (5.4) shows the eigenspectrum obtained by the T-matrix method in the top panel. The eigenfrequencies can be classified as low (when the eigenfrequency drops below the kink frequency of the densest tube), high (when the eigenfrequency rises above the kink frequency of the rarest tube) or average (when it lies within the range of the strand kink frequencies). In the shaded area, corresponding to the last group, many eigenfrequencies are to be found corresponding to complex flutelike eigenmodes (see Luna et al, 2010 [23]). We focus on the lowest and highest eigenfrequency, as collective behaviour can be expected for these eigenfrequencies especially.

In the lower panel of Figure (5.4) the eigenmodes corresponding to the lowest and highest eigenfrequency are shown. Several characteristics of these global loop oscillations are worth pointing out. First of all, the density contrast between the loops (or, equivalently for uniform magnetic fields, the difference in kink frequency) is in general the main parameter which determines which loops will interact with one another. For the lowest eigenfrequency, the denser tubes $1, 2, 3, 4, 6, 7$ and 8 oscillate together in a global circular kinklike pattern. For the highest frequency, the rarer loops 2,5,6,7,10 oscillate collectively. This relation between the eigenfrequencies and the density of the loops with the strongest oscillation amplitudes can also be seen in panels (a), (d), and (g) and (c), (f) and (i) of Figure (5.2). However, in panels (b), (e) and (h) of Figure (5.2), this relation is no longer satisfied, which signals that the distance between the individual strands also influences the global oscillations. Noteworthy, the global kink oscillation of the loop is not identified in the eigenmodes considered in Luna et al., 2010 [23] and it is unclear whether such an eigenmode does exist among the different eigenfrequencies. A consideration of the initial value problem showed that the center of mass of the system will react to an initial perturbation of the multi-loop system polarised with respect to a certain axis with near-elliptic motions with the major axis of the ellipse in the direction of this axis. This could serve as a diagnostic to distinguish between the competing loop models, even though in my view it suggests foremost that the initial pulse contributes more to the global oscillation than the complex global modes of the system. More studies are in any case needed.

### 5.2.2 Long-wavelength approximation

This subsection presents some new expressions for the T-matrix (5.25) and the associated linear system of equations (5.19) which I found using the long-wavelength approximation. Many of these results should be considered as work in progress. In my view, this approach can eventually lead to new insight in the character of oscillations of multi-loop systems and I will indicate which points are not entirely resolved at the writing of this thesis and will be addressed during the summer months.

In the numerical simulations of the previous subsection, we have seen that the long-wavelength approximation should be rather accurate in view of the parameters used in the simulations. Just like we did there, we will assume that the radii of all magnetic flux

tubes are the same and equal to $R$. Because of definition (5.3), we have

$$(k_0R)^2 = (kR)^2\left(\frac{\omega^2-\omega_{\rm Ae}^2}{\omega_{\rm Ae}^2}\right) \qquad (k_jR)^2 = (kR)^2\left(\frac{\omega^2-\omega_{\rm Aj}^2}{\omega_{\rm Aj}^2}\right).$$

such that in general, the long-wavelength approximation $kR \ll 1$ also implies that $k_0R \ll 1$ and $k_jR \ll 1$. The case of many magnetic flux tubes is slightly more subtle in this respect than the well-known case of the uniform single magnetic cylinder, described in Section 2.1. The reason is that it can be easily shown from the formula for the kink frequency that $k_1^2 = (\zeta-1)/(\zeta+1)k^2$ for a single cylinder such that the long-wavelength approximation implies a posteriori that $k_1R \ll 1$. However, if we consider the case of two loops, the long-wavelength assumption should in principle lead to the discovery of the homogeneous two-loop eigenfrequencies (3.16) of Chapter 3. Then from Figure (4.7) in Section 4.4. it follows that $\omega_+ \to \omega_{\rm Ae}$ if $\zeta_R \to 1$. Then the perpendicular wave number in the right loop yields $(k_RR)^2 = (kR)^2(\zeta_R-1)$. Hence apart from the long-wavelength assumption, one should also assume that the density contrast between the loops does not become anomalously large.

For realistic coronal conditions , we can safely assume that we avoid this caveat. In this case, we can perform a Taylor expansion of the Bessel functions of the first kind for positive integers $m$

$$\begin{aligned} J_m(x) &= \frac{x^m}{2^m m!} + O(x^{m+2}) \\ J_m'(x) &= \frac{mx^{m-1}}{2^m m!} + O(x^{m+1}), \qquad J_0'(x) = -\frac{x}{2} + O(x^3) \end{aligned} \tag{5.27}$$

and use asymptotic expansions of the Hankel function of the first kind near the origin

$$\begin{aligned} H_0^{(1)}(x) &= \frac{2i}{\pi}\ln\left(\frac{x}{2}\right) + O(x^0) \\ H_m^{(1)}(x) &= -\frac{i2^m(m-1)!}{\pi x^m} + O(x^{-m+2}) \quad m \neq 0 \end{aligned} \tag{5.28}$$

to obtain the following asymptotic formulae for the T-matrix for small values of the argument:

$$T_0^j = \frac{-i\pi k_0k_jR^3(k_j-k_0)}{16k_j/k_0R + k_0k_jR\ln\left(\frac{k_0R}{2}\right)/4} + O(kR)^4, \tag{5.29}$$

$$\begin{aligned} T_m^j &= \frac{i\pi}{2^{2m}m!(m-1)!}(k_0R)^{2m}\frac{(\zeta_j-1)\omega^2}{(\zeta_j+1)\omega^2-2\omega_{\rm Ae}^2} + O(kR)^{2m+2} \\ &= \frac{i\pi}{2^{2m}m!(m-1)!}(kR)^{2m}\left(\frac{\omega^2-\omega_{\rm Ae}^2}{\omega_{\rm Ae}^2}\right)^m\frac{(\zeta_j-1)\omega^2}{(\zeta_j+1)\omega^2-2\omega_{\rm Ae}^2} + O(kR)^{2m+2}. \end{aligned} \tag{5.30}$$

Not only does the numerator of $T_0^j$ in equation (5.25) vanish in zeroth order because of the factor $m$ in $J_m'(x)$, the first-order terms also become zero because of a cancellation in the two first-order terms of the numerator of $T_0^j$. This is why $T_0^j$ only starts with a term in third order in $(kR)$. The same expressions for $T_m^j$ are valid for negative $m$ because of the formulae $J_{-m}(x) = (-1)^mJ_m(x)$ and $H_{-m}^{(1)}(x) = (-1)^mH_m^{(1)}(x)$. If we would truncate

the system (5.19) at $m_t = 0$, then we should expand $T_0^j$ up to higher order in order to obtain nontrivial solutions to the dispersion relation (5.26). If we however truncate the equations at higher $m_t$, we can work with $T_0^j = 0$ up to second order.

Some properties of the long-wavelength T-matrix (5.30) are worth considering. It shows that Alfvén waves in the exterior medium will be solutions of the dispersion relation since $T_m^j$ vanishes there. Furthermore, the zeroes of the last factor correspond to the kink frequency of the $j^{\text{th}}$ loop. This is as expected, since in the case $N = 1$, all coefficients $B_m$ are zero because of equation (5.19). In order to have a solution in the exterior medium (5.8), the product $B_m T_m$ must be a finite arbitrary number, hence the eigenfrequency of the single loop should be a zero of the denominator of $T_m^j$. This behaviour is in fact already present in the original T-matrix (5.25), as was noted by Luna et al., 2009 [22].

Let us, for the remainder of this subsection, specialise to a system of two coronal loops of relative density $\zeta_L$ and $\zeta_R$ aligned in the familiar way in the coordinate system as in Figure (5.1). Then the term $\exp(n-m)\varphi_{ij}$ in (5.19) is equal to $(-1)^{n-m}$. If we truncate the system at $m = m_t$, then (5.19) is a homogeneous linear system of $N(2m_t - 1)$ equations for as many unknowns. It can be written in the form $Mb = 0$ with

$$\begin{aligned} b &= (B^L_{-m_t}, B^L_{-m_t+1}, \ldots, B^L_{m_t}, B^R_{-m_t}, B^R_{-m_t+1}, \ldots, B^R_{m_t})^T \\ M &= \left[\begin{array}{c|c} I_{2m_t+1} & P \\ \hline Q & I_{2m_t+1} \end{array}\right] \end{aligned} \tag{5.31}$$

in which

$$\begin{aligned} P(i,j) &= T^R_{j-(m_t+1)}\, H^{(1)}_{j-i}(k_0 d)\, (-1)^{j-i} \\ Q(i,j) &= T^L_{j-(m_t+1)}\, H^{(1)}_{j-i}(k_0 d)\, (-1)^{j-i}. \end{aligned} \tag{5.32}$$

Because the block matrices in the bottom row commute, we can use the identity $\det M = \det(I - PQ)$ and thus exploit the block structure of $M$ to reduce the dimension of the problem by a factor 2. Nevertheless, I have not yet found solutions for the equation $\det M = 0$ so far, because of numerical instability of the problem. This is one avenue of research which will undoubtedly be taken further.

However, looking at equation (5.30), the long-wavelength assumption suggests it is reasonable to only retain terms which are of order $\mathrm{O}(kR)^2$. This means setting $m_t = 1$ and retaining $T_0^j = 0$ in the equations. Then using the asymptotics of the Hankel function of the first kind (5.28) together with equations (5.29) and (5.30) we can calculate the three-dimensional matrices $P$ and $Q$-matrix in (5.32) by hand. This yields

$$P(i,j) = -\frac{1}{2}(kR)^2 \left(\frac{\omega^2 - \omega_{\text{Ae}}^2}{\omega_{\text{Ae}}^2}\right) \frac{(\zeta_R - 1)\omega^2}{(\zeta_R + 1)\omega^2 - 2\omega_{\text{Ae}}^2} \begin{pmatrix} \ln\left(\frac{k_0 d}{2}\right) & 0 & \frac{-2}{(k_0 d)^2} \\ \frac{-1}{k_0 d} & 0 & \frac{1}{k_0 d} \\ \frac{-2}{(k_0 d)^2} & 0 & \ln\left(\frac{k_0 d}{2}\right) \end{pmatrix}$$

$$Q(i,j) = -\frac{1}{2}(kR)^2 \left(\frac{\omega^2 - \omega_{\text{Ae}}^2}{\omega_{\text{Ae}}^2}\right) \frac{(\zeta_L - 1)\omega^2}{(\zeta_L + 1)\omega^2 - 2\omega_{\text{Ae}}^2} \begin{pmatrix} \ln\left(\frac{k_0 d}{2}\right) & 0 & \frac{-2}{(k_0 d)^2} \\ \frac{-1}{k_0 d} & 0 & \frac{1}{k_0 d} \\ \frac{-2}{(k_0 d)^2} & 0 & \ln\left(\frac{k_0 d}{2}\right) \end{pmatrix}.$$

Then the condition $\det(I - PQ) = 0$ leads us eventually to the dispersion relation

$$\left(\ln^2\left[\frac{k_0 d}{2}\right] - \frac{4}{(k_0 d)^4}\right)^2 X^2 - 2\left(\ln^2\left[\frac{k_0 d}{2}\right] + \frac{4}{(k_0 d)^4}\right) X + 1 = 0 \tag{5.33}$$

in which the notation

$$X = \frac{1}{4}(kR)^4 \left(\frac{\omega^2 - \omega_{\mathrm{Ae}}^2}{\omega_{\mathrm{Ae}}^2}\right)^2 \frac{(\zeta_L - 1)\omega^2}{(\zeta_L + 1)\omega^2 - 2\omega_{\mathrm{Ae}}^2} \frac{(\zeta_R - 1)\omega^2}{(\zeta_R + 1)\omega^2 - 2\omega_{\mathrm{Ae}}^2}$$

has been used.

Since $X$ is of order $(kR)^4$ and $(k_0 d \sim k_0 R)$, if we only retain terms of order $\mathrm{O}(kR)^2$ in (5.33) this yields the following dispersion relation, accurate up to order $(kR)^2$:

$$\begin{aligned} \frac{16}{(k_0 d)^8} X^2 - \frac{8}{(k_0 d)^4} X + 1 &= 0. \\ \Leftrightarrow \left(\frac{4}{(k_0 d)^4} X - 1\right)^2 &= 0 \\ \Leftrightarrow \frac{1}{(d/R)^4} \frac{(\zeta_L - 1)\omega^2}{(\zeta_L + 1)\omega^2 - 2\omega_{\mathrm{Ae}}^2} \frac{(\zeta_R - 1)\omega^2}{(\zeta_R + 1)\omega^2 - 2\omega_{\mathrm{Ae}}^2} &= 1. \end{aligned} \tag{5.34}$$

Equation (5.34) is identical to the known equation (3.15) for two homogeneous loops in bicylindrical coordinates, if we replace the factor $F^2$ appearing there with $1/(k_0 d)^4$. This term gives the difference between the bicylindrical and cylindrical coordinate systems. Writing this dispersion relation in the form of equation (5.34) shows clearly that when the tubes get placed infinitely far away from one another $(d/R \to \infty)$, the frequency $\omega$ must converge to the kink frequency of the individual loops such that the product on the left-hand side remains finite.

Figure (5.5) shows that for a distance between loops $d/R \gtrsim 3$, the expressions in both coordinate systems are very similar, since both expressions lie close to the kink frequency of the tubes. However, for smaller loop distances, differences start to emerge. In particular, the eigenfrequency $\omega_+$ does not converge to the Alfvén frequency of the exterior fluid anymore when $d/R \to 2$. The different asymptotics are due to the fact that in the cylindrical coordinate system, the loops conserve their volume as they approach one another, which was impossible in the bicylindrical coordinate system. The resulting configuration looks more like an elliptic loop with two different densities at both ends. This undoubtedly has consequences for the damping formulae as well. In Chapter 4 we saw that several limiting cases were hard to tackle within the bicylindrical coordinate system. These results show that the long-wavelength T-matrix approach presents fertile ground to study the oscillations of systems of coronal loops.

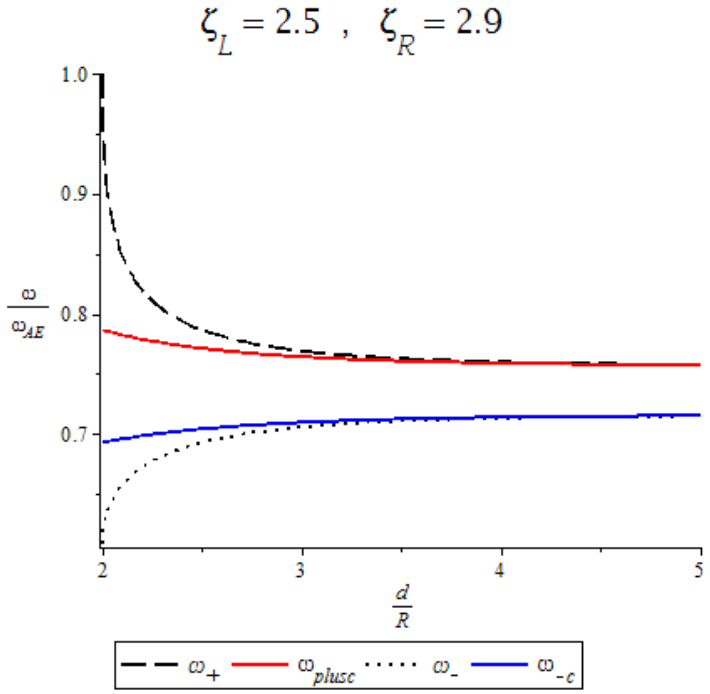


Figure 5.5: Comparison of the homogeneous two-loop frequencies obtained in the cylindrical (blue and red full lines) and bicylindrical (dotted and dashed lines) coordinate system.

### 5.2.3 Damped oscillations of a system of coronal loops

This final section is concerned with the idea of using the jump conditions (2.37) derived in Chapter two as boundary conditions on the loop boundaries to relate the total external field (5.20) and the internal field in the $j^{\text{th}}$ loop (5.21) to one another. Such an extension of the theory has already been performed in the case of sunspot models by Keppens et al. (1994) [19]. As far as I am aware, such a study has not yet been performed in the equilibrium configuration for coronal loops. Due to time constraints, I will only derive the governing equation for the T-matrix here. Future research will involve implementing this method to look for damped eigenmodes.

The use of the jump conditions due to resonant absorption in each of the $N$ loops replaces boundary conditions (5.23) and (5.24) by

$$\psi^j_{\text{in}}(a_j - l_j) = \psi_{\text{tot}}(a_j) \tag{5.35}$$

$$\xi^j_{r,\text{in}}(a_j - l_j) = \xi_{r,\text{tot}}(a_j) - [\xi_r]. \tag{5.36}$$

in which $l_j$ is the thickness of the inhomogeneous layer in the $j^{\text{th}}$ loop. Let us repeat for convenience the jump condition we found in Chapter 2 by following the method of Sakurai et al. (1991) [34], with slightly adapted notation:

$$[\xi^j_r] = -\frac{i\pi m^2 \psi}{\rho_{\text{Aj}} r^2_{\text{Aj}} |\Delta_j|}, \qquad [\psi] = 0. \tag{5.37}$$

Because the total pressure is continuous across the resonant layers, we can approximate $\psi$ appearing in the jump by its value at the outside boundary of the flux tube at $|\mathbf{r} - \mathbf{r_j} = a_j|$.

Then a similar calculation as in the Ansatz to (5.24) transforms the second boundary condition (5.36) into

$$\frac{1}{k_j(\rho v_{\rm A}^2)}{\psi_{\rm in}^j}'(a_j - l_j) = \frac{1}{k_0(\rho v_{\rm A}^2)}\psi'_{\rm tot}(a_j) + \frac{i\pi m^2 \psi_{\rm tot}(a_j)}{\rho_{\rm Aj} r_{\rm Aj}^2 |\Delta_j|}. \tag{5.38}$$

Here a prime denotes the derivative with respect to the argument: $f'(x) = \frac{df}{dx}$. Then using boundary conditions (5.35) and (5.38)) to equations (5.21) and (5.20) yields after some straightforward algebra the following expression for the T-matrix corresponding to resonantly damped oscillations of a system of $N$ loops:

$$\begin{aligned} T_m^j =& k_0 J_m(k_0 a_j) J'_m(k_j(a_j - l_j))\rho_{\rm Aj} r_{\rm Aj}^2 |\Delta_j| - k_j J'_m(k_0 a_j) J_m(k_j(a_j - l_j))\rho_{\rm Aj} r_{\rm Aj}^2 |\Delta_j| \\ & - k_0 k_j i\pi m^2 J_m(k_0 a_j) J_m(k_j(a_j - l_j))\rho_e v_{\rm Ae}^2 \\ & \overline{k_j {H_m^{(1)}}'(k_0 a_j) J'_m(k_j(a_j - l_j))\rho_{\rm Aj} r_{\rm Aj}^2 |\Delta_j| - k_0 {H_m^{(1)}}'(k_0 a_j) J'_m(k_j(a_j - l_j))\rho_{\rm Aj} r_{\rm Aj}^2 |\Delta_j|} \\ & + H_m^{(1)}(k_0 a_j) J_m(k_j(a_j - l_j)) k_0 k_j \rho_e v_{\rm Ae}^2. \end{aligned} \tag{5.39}$$

This equation reduces to (5.25) in the limiting case of $l_j \to 0, |\Delta_j| \to \infty$ removing the inhomogeneous layers. Due to the problems described in the previous subsection, I have not investigated the damped eigenfrequencies resulting from substitution of equation (5.39) into the linear system of equations (5.19) yet. This is a topic of further research which eventually should be able to increase our understanding of damped oscillations of multi-loop systems, and give valuable tools in coronal seismology.

# Summary and conclusions

Observations of coronal loop oscillations have shown the need to extend the models for homogeneous magnetic cylinders. Better models of oscillating coronal loops will improve the measurement of the equilibrium parameters by an inversion of these models, a technique known as coronal seismology. There are many ways to generalise the models of homogeneous cylinders to more realistic equilibria.

We have concentrated our efforts on two generalisations. The first one is to include a continuous density profile in a boundary layer. This leads to a coupling of the MHD equations. The governing differential equations are singular at the resonant point in ideal MHD, but not in resistive MHD. By a matching of the local dissipative solution and the ideal solution, jump conditions were formulated for the driven problem, which showed that incoming transverse waves are damped as part of their energy gets converted into Alfvén wave energy. If we assume a thin boundary, these jump conditions could be used as boundary conditions to derive expressions of damped eigenmodes of the system.

The second generalisation of the theory concerns systems of coronal loops. Two mathematical techniques have been considered to describe the oscillations of such a system: the method of separation of variables and an expansion of the solutions into a series of cylindrical functions.

This master thesis has made some steps towards a unification of both concepts by providing new formulae of coronal loop oscillations, using the two formalisms. These analytical investigations can complement the computer-assisted simulations of oscillations of multi-loop systems and provide deeper insight into them. I have derived a new expression for the damping decrement for a system of two, not necessarily identical, loops. A subdivision must be made to include standard as well as anomalous systems. When fixing the average thickness of the nonuniform layer, it has been shown that the interaction between the loops is maximal when their densities are equal and the loops are placed not too far away from each other. For larger separations, the loops behave independently. In the bicylindrical coordinate system, the interaction of the loops reduces the amount of damping of the eigenfunctions. Furthermore, when the tubes interact strongly with one another, the damping is maximal for the eigenfrequency $\omega_+$ corresponding to the 'forced' $S_y$ and $A_x$ modes and minimal for the 'unforced' $S_x$ and $A_y$ eigenmodes. However, since the radii of the cylinders are so strongly linked to the bicylindrical coordinate system, several limiting cases are not best described in this framework.

The T-matrix method represents probably a better alternative to study the oscillations of two loops, and are necessary if we want to consider extensions of the theory to a system of more cylinders. We have seen that the relative density between the loops is the main parameter which determines the nature of the eigenmodes of a multi-loop system. I have also derived expressions which investigate the case of long wavelengths, and found that for two loops, the results of both mathematical techniques coincide as they should, up to a transformation of the coordinate system. Finally, an extension of the theory for damped oscillations of systems of coronal loops is proposed. Further research can build on this fertile ground to explore in more detail the physical consequences of the expressions derived here.

# Nederlandstalige samenvatting

De corona is de buitenste laag van de zonne-atmosfeer. Door de hoge temperaturen die er heersen, is het gas er sterk geïoniseerd. Een geïoniseerd gas of plasma is elektrisch geleidend en onderhevig aan elektromagnetische krachten. Onder invloed van het magnetische veld organiseert het coronale plasma er zich in lussen.

De macroscopische structuur van een plasma kan worden beschreven met de magnetohydrodynamische (MHD) vergelijkingen. Dit is een stelsel partiële differentiaalvergelijkingen die kunnen worden beschouwd als een combinatie tussen de hydrodynamische vergelijkingen en de wetten van Maxwell, verbonden door de bewegingsvergelijking en de inductievergelijking. Omdat het oplossen van dit stelsel uiterst ingewikkeld is, bestudeert men vaak de reactie van het systeem op kleine verstoringen uit een welbepaalde evenwichtsconfiguratie, die eenvoudiger te begrijpen zijn maar nog steeds fysisch relevant.

Observaties van coronale lussen in hoge resolutie door de Transition Region and Coronal Explorer (TRACE) vanaf 1999 en recenter door het Solar Dynamics Observatory (SDO) (vanaf 2010) laten inderdaad zien dat transversale oscillaties van coronale lussen legio zijn. Door modellen op te stellen voor MHD golven in coronale lussen, kunnen we een beter inzicht krijgen in de evenwichtsconfiguratie van waaruit deze golven ontstaan; een techniek die bekend staat als coronale seïsmologie. Daarnaast laten observaties zien dat zulke transversale oscillaties snel gedempt worden; de energieoverdracht die daarmee gepaard gaat kan de corona verhitten. Ten slotte komen coronale lussen niet afzonderlijk voor, maar verschijnen ze in systemen van min of meer parallelle lussen. In het licht van deze observaties zijn de oorspronkelijke modellen voor een enkele homogene magnetische cylinder uitgebreid; betere modellen leiden namelijk tot betere seïsmologie.

De demping van coronale oscillaties kan beschreven worden door de theorie van resonante absorptie. Deze theorie beschrijft hoe via koppeling tussen de veschillende MHD golven, energie van transversale golven wordt omgezet in energie van golven die langs de magnetische veldlijnen propageren. Daarnaast zijn vele modellen opgesteld die de oscillaties beschrijven van systemen van homogene lussen.

Deze masterthesis poogt de voorgenoemde uitbreidingen van de theorie van oscillaties van magnetische cylinders te verenigen via wiskundige analyse. Eerdere pogingen tot veralgemening maken meestal gebruik van computersimulaties. In de thesis worden twee verschillende wiskundige gezichtspunten aangenomen. Door symmetrieën in het systeem te veronderstellen, kunnen de variablen in de MHD vergelijkingen gescheiden worden. Via deze techniek heb ik uitdrukkingen afgeleid en voor de gedempte oscillaties van een systeem van twee parallelle lussen, en hun afhankelijkheid van de verschillende evenwichtsparameters bestudeerd. De analyse laat zien dat de interactie tussen de lussen de efficiëntie van resonante demping verlaagt. Daarnaast kunnen de oplossingen geschreven worden als een oneindige som van Besselfuncties, functies die de trillingen van cirkelvormige membranen beschrijven. Deze ontwikkeling laat toe om de oscillaties van systemen van lussen te kwantificeren. Ik heb formules afgeleid die deze oscillaties beschrijven in de limiet voor lange golflengten en deze geanalyseerd. Verder onderzoek hierop zal toelaten een vollediger beeld te vormen van de gedempte oscillaties van groepen coronale lussen.

# Bibliography


[1] Andries, J. 'Damping and amplification of MHD quasi-modes in coronal plumes and loops' PhD Thesis, Leuven (2003), 40-47

[2] Arregui, I., Terradas, J., Oliver, R. et al. 'The Resonant Damping of Fast Magnetohydrodynamic Oscillations in a System of Two Coronal Slabs' *ApJ* **674** (2008), 1179-1190

[3] Aschwanden, M. J., Fletcher, L., Schrijver, C. J., & Alexander, D. *ApJ*, **520** (1999), 880

[4] Aschwanden, M. J., Nightingale, W., Andries, J. et al. 'Observational Tests of Damping by Resonant Absorption in Coronal Loop Oscillations' *Apj* **598** (2003) 1375-1386

[5] Bogdan, T. J. & Zweibel, E. G. 'Effect of a fibril magnetic field on solar p-modes', *ApJ* **298** (1985), 867-875

[6] Bogdan, T. J. & Cattaneo, F. 'The normal modes of a resonant cavity containing discrete inhomogeneities - The influence of fibril magnetic fields on the solar acoustic oscillations', *ApJ* **342** (1989), 545-557

[7] Bogdan, T. J. & Fox, D.C. 'Multiple scattering of acoustic waves by a pair of uniformly magnetized flux tubes', *ApJ* **379** (1991), 758-775

[8] Chen, L. & Hasegawa, A. 'Plasma heating by spatial resonance of Alfvén waves' *Phys. Fluids* **17** (1974), 1399-1403

[9] De Moortel, I. & Pascoe, 'Putting Coronal Seismology Estimates of the Magnetic Field Strength to the Test', *ApJ* **699** (2009), L72-L75

[10] Edwin, P.M. & Roberts, B.R. 'Wave propagation in a magnetic cylinder' *Sol. Phys.* **88** (1983), 179-191

[11] Goedbloed, J.P. 'Lecture notes on ideal magnetohydrodynamics', Rijnhuizen Report, (1983), p 113

[12] Goedbloed, J.P. & Poedts, S. *Principles of Magnetohydrodynamics: with applications to laboratory and astrophysical plasmas*
Cambridge, Cambridge University Press, 2004

[13] Goossens, M., Ruderman, M.S. & Hollweg, J.V. 'Dissipative MHD solutions for resonant Alfvén waves in 1-dimensional magnetic flux tubes' *Sol. Phys.* **157** (1995), 75-102

[14] Goossens, M. 'Seismology of kink oscillations in coronal loops: Two decades of resonant damping' *In: Waves & Oscillations in the Solar Atmosphere: Heating and Magneto-Seismology Proceedings IAU Symposium* **247** (2007) R. Erdelyi & C. A. Mendoza-Briceno, eds.

[15] Goossens M., Terradas, J., Andries, J. et al. 'On the nature of kink MHD waves in magnetic flux tubes' *A&A* **503** (2009), 213-223

[16] Goossens, M., Van Doorsselaere, T., Soler, R. & Verth, G. 'Energy Content and Propagation in Transverse Solar Atmospheric Waves' *ApJ* **768** (2013), id. 191

[17] Heyvaerts, J. & Priest, E.R. 'Coronal heating by phase-mixed shear Alfvén waves' *A&A* **117** (1983), 220-234

[18] Hollweg, J.V. & Yang, G. 'Resonance-absorption of compressible MHD waves at thin surfaces' *J. Geophys. Res.* **93** (1988), 5423-5436

[19] Keppens, R., Bogdan, T. J. & Goossens, M. 'Multiple scattering and resonant absorption of p-modes by fibril sunspots', *ApJ* **436** (1994), 372-389

[20] Klimchuk, J.A. 'On Solving the Coronal Heating Problem' *Sol. Phys.* **234** (2006), 41-77

[21] Luna, M., Terradas, J., Oliver, R. et al. 'Transverse oscillations of two coronal loops' *ApJ* **676** (2008), 717-727

[22] Luna, M., Terradas, J., Oliver, R. & Ballester, J. L. 'Transverse Oscillations of Systems of Coronal loops', *ApJ* **692** (2009), 1582-1589

[23] Luna, M., Terradas, J., Oliver, R. & Ballester, J. L. 'Transverse Oscillations of a Multi-stranded Loop', *ApJ* **716** (2010), 1371-1380

[24] McIntosh, S. W., de Pontieu, B., Carlsson, M. et al. 'Alfvénic waves with sufficient energy to power the quiet solar corona and fast solar wind' *Nature* **475** (2011), 477-480

[25] Morton, R. J. & Erdélyi R., 'The effect of elliptic shape on the period ratio P1/P2 of emerging coronal loops' *A&A* **502** (2009)

[26] Nakariakov, V.M., Ofman, L., DeLuca, E.E. et al. 'TRACE observation of damped coronal loop oscillations: implications for coronal heating' *Science* **285** (1999), 862-864

[27] Ofman, L. 'Three-Dimensional Magnetohydrodynamic Models of Twisted Multithreaded Coronal Loop Oscillations' *ApJ* **694** (2009), 502-511

[28] Parker, E.N. 'Sunspots and the physics of magnetic flux tubes. I - The general nature of the sunspot. II - Aerodynamic drag', *ApJ* **230** (1979), 905-923

[29] Poedts, S., Goossens, M., Kerner, W. 'Temporal evolution of resonant absorption in solar coronal loops' *CoPhC* **59** (1990), 95-103

[30] Ramm, A.G. 'Scattering by Obstacles', *Dordrecht, Reidel* (1986), 144-178

[31] Robertson, D. & Ruderman, M.S. 'Resonantly damped oscillations of two coronal loops' *A&A* **525** (2011), A4

[32] Ruderman, M.S., Tirry, W. & Goossens, M. 'Non-stationary resonant Alfvén surface waves in one-dimensional magnetic plasmas' *J. Plas. Ph.* **54** (1995), 129-148

[33] Ruderman, M.S. 'The resonant damping of oscillations of coronal loops with elliptic cross-sections' *A&A* **409** (2003) 287-297

[34] Sakurai, T., Goossens, M. & Hollweg, J.V. 'Resonant behavior of MHD waves on magnetic flux tubes. I. Connection formulae at the resonant surfaces' *Sol. Phys.* **133** (1991), 227-245

[35] Schwarzschild, M. 'On noise arising from the solar granulation' *ApJ* **107** (1948), 1-5

[36] Terradas, J., Arregui, I., Oliver, R. et al. 'Resonant Absorption in Complicated Plasma Configurations: Applications to Multistranded Coronal Loop Oscillations' *ApJ* **679** (2008), 1611-1620

[37] Tomczyk, S., McIntosh, S.W., Keil, S.L. et al. 'Alfvén Waves in the Solar Corona' *Science* **317** (2007), 1192-

[38] Van Doorsselaere, T., Andries, J., Poedts, S. & Goossens, M. 'Damping of Coronal Loop Oscillations: Calculation of Resonantly Damped Kink Oscillations of One-dimensional Nonuniform Loops', *ApJ* **606** (2004), 1223-1232

[39] Van Doorsselaere T., Ruderman, M.S., & Robertson, D. 'Transverse oscillations of two parallel coronal loops' *A&A* **485** (2008), 849-857

[40] Verwichte, E., Nakariakov, V. M., Ofman, L. & Deluca, E. E. 'Characteristics of transverse oscillations in a coronal loop arcade' *Sol. Ph.* **223** (2004), 77-94

[41] Waterman, P.C. 'New formulation of acoustic scattering', *ASAJ* **45** (1969), 1417-1429

[42] Yang et al., 'Response of the solar atmosphere to magnetic field evolution in a coronal hole region', *A&A* **501** (2009), 745-753

**Centrum voor Plasma-Astrofysica**
Celestijnenlaan 200B bus 2400
3001 LEUVEN (HEVERLEE), BELGIË
tel. + 32 16 32 70 15
fax + 32 16 32 79 98
wis.kuleuven.be/CmPA/
www.kuleuven.be